

**VISUALIZING THE ENDOTHELIAL SURFACE: IMAGING AND OTHER
RESEARCH TECHNIQUES FOR STUDYING THE PHYSIOLOGY OF THE
ENDOTHELIAL-BLOOD POOL INTERFACE**

A Thesis

Presented to

The Faculty of the Department of Biomedical Engineering

In Partial Fulfillment

of the Requirements for the Degree of

Master of Science

by

Eran Brown

June 15, 2020

Table of Contents

Section I: Background

Introduction.....	3
Acronyms and Abbreviations.....	5
Chapter 1: Physiology of the Endothelial Surface.....	6

Section II: Techniques for Studying the Endothelial Surface

Chapter 2: Ex-Vivo and In-Vitro Model Vascular Systems.....	39
Chapter 3: Techniques for Live Imaging of Blood Flow.....	53
Chapter 4: Molecular Imaging of the Endothelial-Blood Pool Interface.....	66

Section III: Translational Applications of Endothelial Imaging

Chapter 5: Platelet-Endothelial Interactions in Early Atherosclerosis.....	94
Chapter 6: Remote Endothelial Activation Following Myocardial Ischemia.....	116
Chapter 7: Cardiovascular Toxicity of Tyrosine Kinase Inhibitors.....	136

Acknowledgements and Disclosures.....	159
--	------------

Introduction

While cardiovascular disease has been an area of significant research and clinical progress over the last few decades, it remains the leading cause of death worldwide and a substantial burden for both patients and healthcare providers. Nevertheless, medical advancements have drastically improved survival and quality of life across the range of cardiovascular pathologies, and imaging has played a key role in ushering in this improved standard of care. The diverse range of novel imaging modalities currently available for studying the heart and vasculature provides unique access to anatomy and physiology that would otherwise only be visible with surgical intervention and is at the center of both medical research and clinical practice. While many of the more common techniques visualize the heart and vessels from a macro perspective, there is less widespread use and familiarity with imaging techniques focused specifically on the endothelial surface, despite its massive importance in cardiovascular health and disease. The increasing number of options for imaging the endothelium and endothelial-blood pool interface as well as the need to simultaneously contextualize findings within the state of the entire cardiovascular system necessitates a comprehensive understanding of the various techniques that exist and how they can be used in a holistic fashion to uncover new pathways, evaluate novel therapeutics, and provide diagnostic information.

Rather than presenting and evaluating a hypothesis, this thesis will guide readers through many approaches to examining the endothelium from both a research and clinical perspective and illustrate how these techniques are applied to a diverse range of physiological settings. I will explore several common cardiovascular and endothelial

imaging techniques, as well as some complementary non-imaging techniques, detailing principles, methodology, and clinical and research applications. These techniques span several different imaging modalities including ultrasound, PET-CT, and MRI, and provide information on endothelial physiology, cardiovascular anatomy, blood flow, molecular and cellular processes, and tissue morphology. Applications include basic studies of pathophysiology, identification of drug targets and evaluation of novel therapeutic agents, clinical risk stratification, and diagnostics. This work will include more basic and widespread techniques such as the 2-D echocardiogram as well as more recent and less commonly used innovations such as ultrasound molecular imaging. Specifically, this work will focus heavily on techniques for visualizing and studying the vascular endothelium and the endothelial-blood pool interface. As the vascular endothelium plays many critical regulatory roles, it is both incredibly important and challenging to study non-invasively given that contrary to events such as ventricular ejection or arterial stenosis, endothelial processes occur at a microscopic level. Operating as two distinct parts of one system, the heart and vascular endothelium each play a major role in determining the function and health of the other, and many of the techniques and case studies presented here illustrate this relationship and how it affects cardiovascular disease progression.

In addition to an overview of techniques and how they are used to study atherosclerosis, one of the primary applications in our laboratory, this thesis will also provide three pre-clinical case studies that demonstrate how to create a palette of techniques for answering specific questions in cardiovascular biology and medicine. As the case studies chosen are largely concerned with atherosclerosis, vascular endothelial dysfunction, and platelet-endothelial interactions, these themes will be a major focus throughout. Specific attention will be paid to how the techniques discussed can provide insights on the role of platelet-endothelial interactions and disruption of endothelial function in different disease settings.

Acronyms and Abbreviations

CAD- coronary artery disease

CEU- contrast-enhanced ultrasound

DKO – double knockout

MB- microbubble

MI- myocardial infarction

MR- magnetic resonance

RN- radionuclide

ULVWF- Ultra-large von Willebrand Factor

VWF- von Willebrand Factor

Cardiovascular and Endothelial Physiology

Summary

In order to fully understand the principles behind the techniques described in this manuscript, as well as their applications, it is important to have working knowledge of cardiovascular and, more specifically, endothelial physiology. This chapter serves as an introduction to basic cardiac function, clinical measurements commonly used to characterize the cardiovascular system, endothelial physiology, and the pathophysiology of atherosclerotic vascular disease. Many of the concepts detailed in this chapter are in fact based on observations made using the imaging and other research techniques explored in later chapters.

Basic Cardiovascular Physiology

While this work focuses on the study of the endothelial surface, this requires an understanding the context that the endothelium functions in. In many applications, studying the endothelium is not the main goal but is simply a part of a more broadly focused query. Appreciating the relationship between the endothelium and the rest of the cardiovascular system of course requires being comfortable with basic cardiovascular physiology. The purpose of this chapter is only to present a basic overview of the cardiovascular system tailored to the techniques and applications described in later chapters. For a more complete description of the cardiovascular system, Braunwald's Heart Disease is recommended.

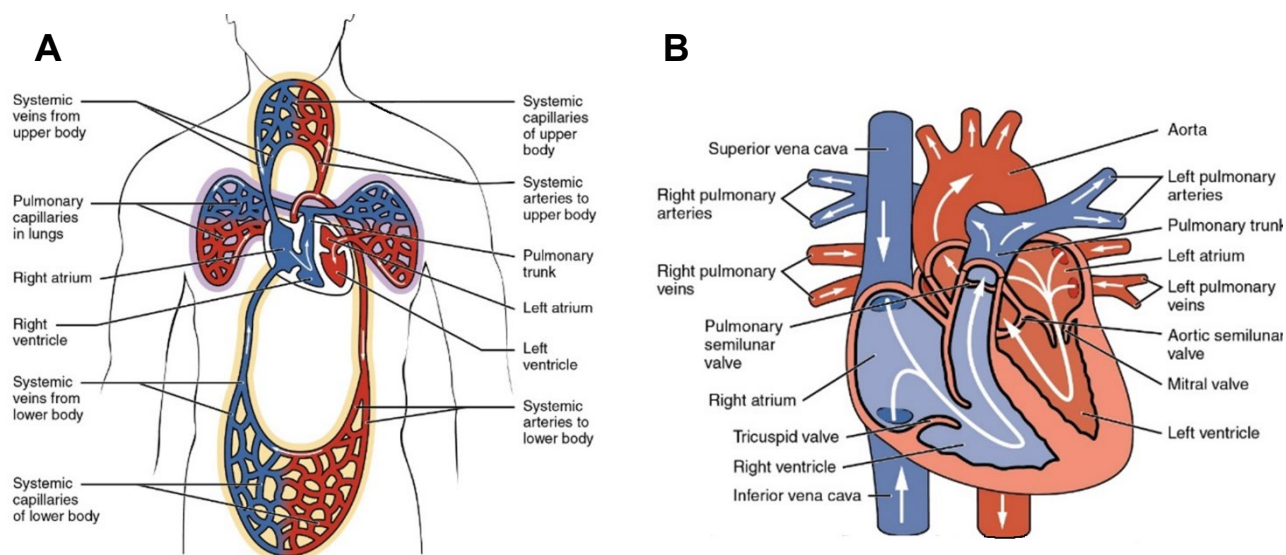


Figure 1: Schematics of (a) cardiovascular anatomy showing pulmonary and venous circulation and (b) cardiac anatomy showing chambers, valves, and great vessels. Vessels and chambers containing deoxygenated or oxygenated blood are shown in blue or red, respectively [1].

The most basic function of the cardiovascular system is to deliver oxygen and nutrients to tissue while removing carbon dioxide and other waste. These functions are dependent on adequate blood flow to, or perfusion of, a given tissue based on metabolic needs [1]. The cardiovascular system has many other functions such as providing a transportation system for immune responses to damaged or infected tissue, endocrine signaling, and thermoregulation, but these roles are less essential to understanding overall design and function of the heart and vasculature. **Figure 1** details the anatomy of the cardiovascular system and the direction of blood flow. There is a diverse array of measurements that can be used to characterize cardiovascular function in a given patient, ranging from simple measurements requiring only a stethoscope to those requiring complex imaging techniques. Some common measurements of cardiovascular function as well as their units and methods for obtaining are listed in **Table 1**.

Each cycle of the heart follows the same set of events represented in **Figure 2**. The right and left sides of the heart operate in tandem, with the right side receiving blood from the venous system and pumping it to the lungs for gas exchange, and the right side receiving oxygenated blood from the lungs and pumping it to the body. The

Measure	Unit	Common Methods	Mathematical Formula
Heartrate (HR)	bpm	Stethoscope, electrocardiogram	
Blood Pressure	mmHg	sphygmomanometer	
End Diastolic Volume (EDV)	L	Ultrasound, CT, MRI	$SV=EDV-ESV$
End Systolic Volume (ESV)	L	Ultrasound, CT, MRI	$CO=HR*SV$
Stroke Volume (SV)	mL	Ultrasound, CT, MRI	$SV=EDV-ESV$
Cardiac Output (CO)	L/min	Ultrasound, thermodilution, Fick's method	$CO=HR*SV$
Ejection Fraction (EF)	%	Ultrasound, CT, MRI	$EF=(SV/EDV)*100$
End Diastolic Pressure (EDP)	mmHg	Cardiac catheterization	
End Systolic Pressure	mmHg	Cardiac catheterization	

Table 1: Basic cardiovascular measurements.

right and left atria receive and transmit blood to the ventricles, which pump blood to either the lungs or body. Timing is controlled by the nervous system of the heart. Once the sinoatrial (SA) node, or the endogenous cardiac pacemaker, sends out a signal, depolarization spreads from the atria to the ventricles, which pump it, triggering muscle contraction along the way. During the filling of the heart with blood, the mitral and tricuspid valves are open to allow the ventricles to fill through the atria while the aortic and pulmonic valve are closed to prevent backflow. Atrial contraction occurs when the ventricles are almost full, pumping remaining blood in the atria into the ventricles. Once ventricular pressure surpasses atrial pressure, the mitral and tricuspid valves close to prevent backflow into the atria. The ventricular pressure at this time, known as end diastole, is termed preload, and represents the force exerted on the ventricle walls prior to contraction.

During the isovolumic contraction phase, ventricular contraction leads to increased pressure while volume remains constant. Eventually, the building ventricular pressure surpasses the pressure in the aorta or pulmonary artery, at which point the aortic and pulmonic valves open to allow for ejection. The pressure in the periphery that the heart must work against is referred to as afterload, which is determined by systemic vascular resistance, blood volume, and vascular elasticity. The ventricular walls thicken

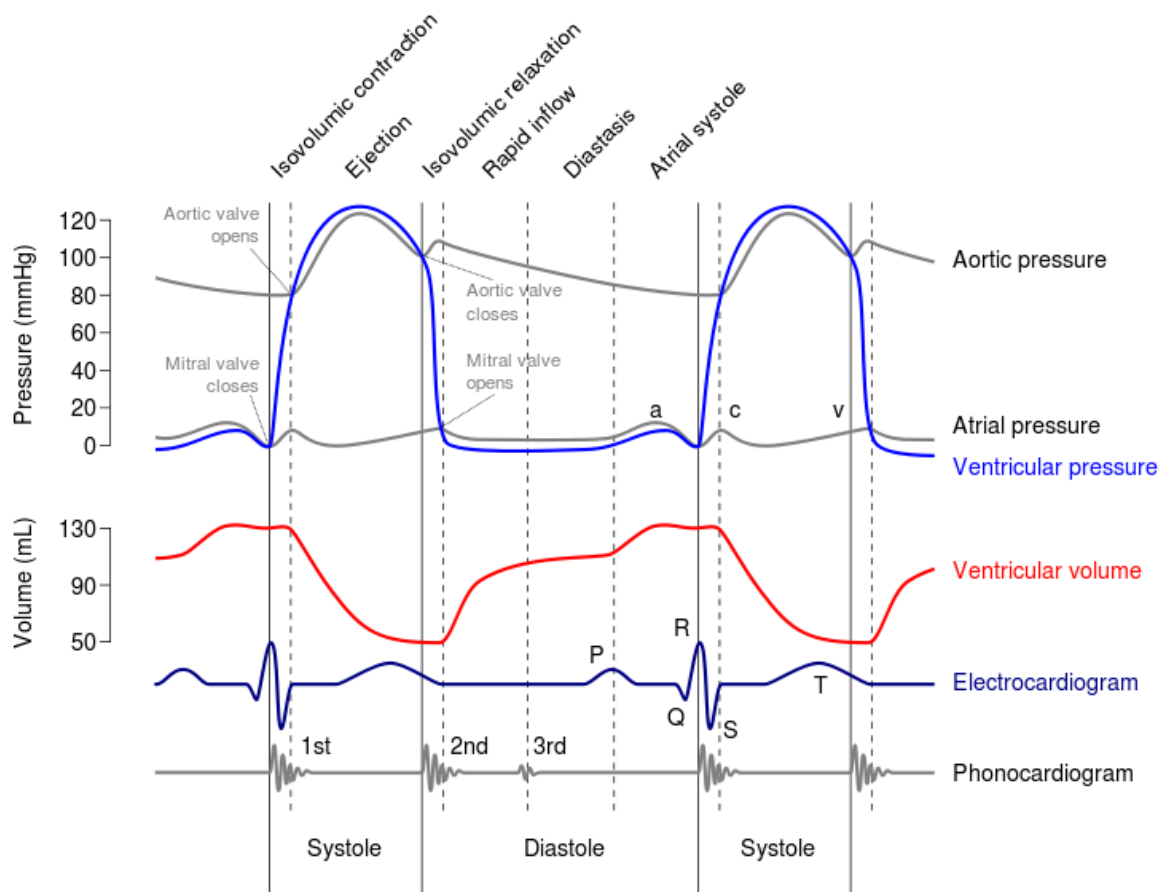


Figure 2: Pressure, volume, electrocardiographic, and auscultory (phonocardiogram) events for each phase of the cardiac cycle. Two full cardiac cycles are shown in terms and each phase of the cardiac cycle and corresponding events are labelled [2].

inwards during contraction and blood is ejected into the aorta or pulmonary artery. As the ventricles begin to relax, the ventricular pressure falls below aortic or pulmonary artery pressure and the aortic and pulmonary valves close again, marking end systole. The relaxation of the ventricles, aided by fibers in the wall that act as a spring, creates a suction that actively pulls in blood from the atria once the mitral and tricuspid valves open again for refilling [3, 4].

The relationship between stroke volume and end diastolic volume, which partially determines preload, is described by the Frank-Starling law, shown by the red curves in **Figure 3**, which states that stroke volume increases proportionally with end diastolic volume up until a point where stroke volume plateaus. The physiological basis for this is higher myocyte contractility in response to greater initial stretching of the muscle fibers,

which creates an optimal sarcomere length and increases binding efficiency of troponin for Ca^{2+} . The plateau limb is created by a drop-off in the force-sarcomere length relationship as myofilaments pass the optimal alignment and the number of possible actin-myosin cross-bridges that drive contraction declines along with overlap between thick and thin filaments. This property of myocytes to increase contractility with increasing preload allows the heart to adapt to increased venous return. When preload is held constant, positive or negative inotropic effects can shift the cardiac function curve up or down, respectively [5].

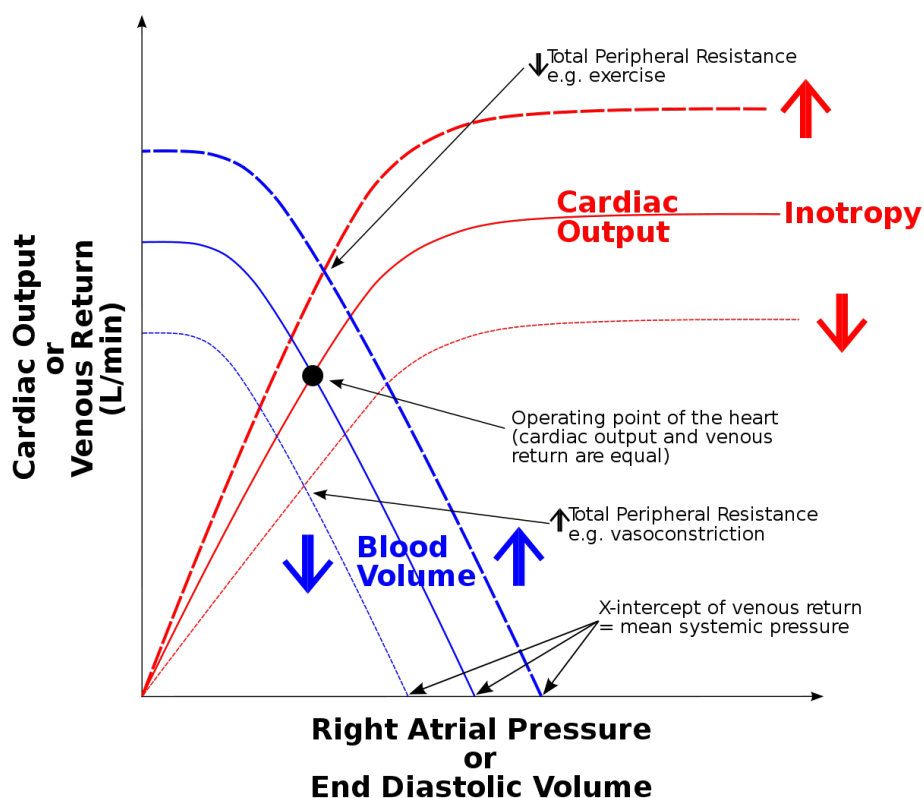


Figure 3: Frank-Starling cardiac function curve (Red) illustrating the effect of preload (or end diastolic volume) on cardiac output (or stroke volume) under different inotropic states; and relationship between atrial pressure and venous return under different intravascular volume states (blue). The intersection between the two curves represents the balanced equilibrium point where output and return are identical.

The Frank-Starling curve is often presented superimposed with the venous return curve, shown in blue in **Figure 3**, which relates venous return to right atrial pressure. As

venous return is dependent on a pressure gradient, increased right atrial pressure leads to decreased venous return given the reduction in gradient. When right atrial pressure is constant, increased venous resistance will also lead to reduced venous return.

Assuming no major bleeding or peripheral blood accumulation, venous return must be equal to cardiac output under steady state conditions. Thus, the point at which the venous return curve intersects the Frank-Starling cardiac function curve is referred to as the operating point of the heart. If, for example, total peripheral resistance were to increase, and the venous return curve shifted to the left, the operating point of the heart would move along the cardiac function curve to a new position with reduced cardiac output [6].

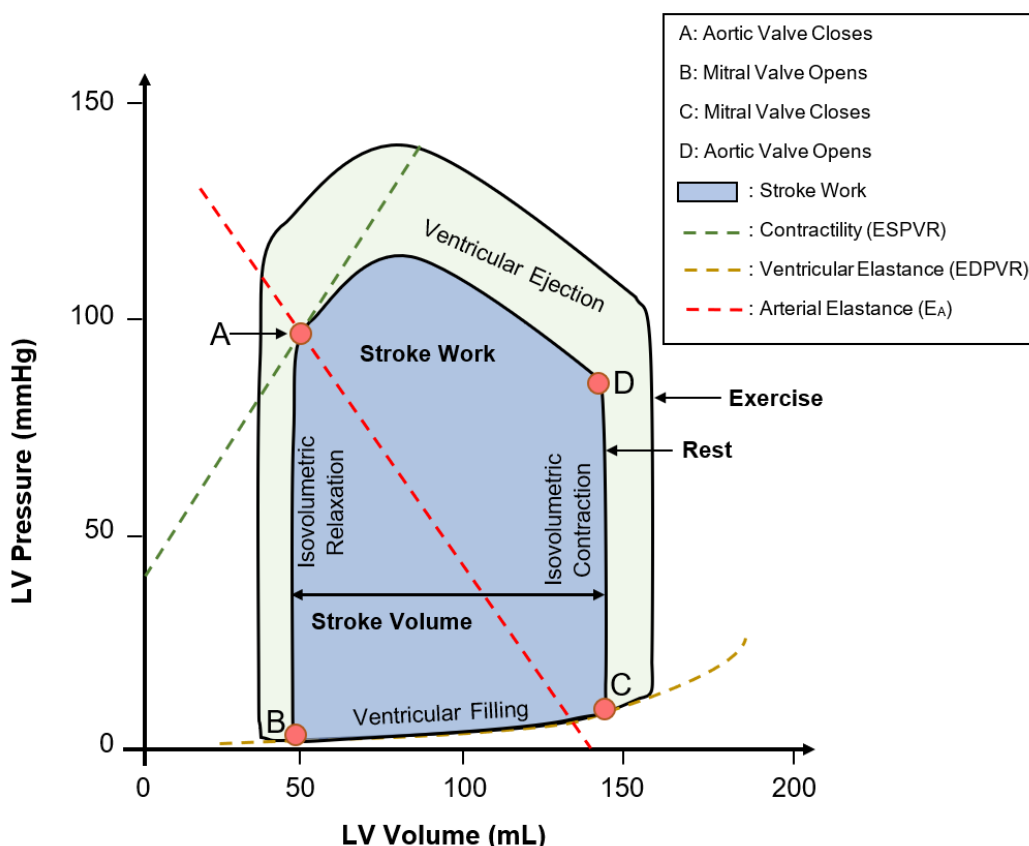


Figure 4: Typical pressure-volume loops at rest (blue) and stress (green). The cardiac cycle is represented moving counterclockwise along each loop. Stroke volume is represented by the horizontal length of each loop and stroke work is the enclosed area. The events that separate the four stages of the cardiac cycle are marked with red circles. When contractility is held constant, aortic valve closure will move along the contractility (ESPVR) curve as other variables change, while the same is true for mitral valve closure and ventricular elastance (EDPVR). Note that the EDPVR curve begins to sharply rise at the point when the ventricle cannot accommodate additional volume without significant increases in pressure.

In addition to the Frank-Starling and venous return curves, pressure-volume loops, as seen in **Figure 4**, are another useful method of describing cardiac function and illustrating how changes to a given variable affect function. A pressure-volume curve, when read counter-clockwise, shows the various stages of the cardiac cycle and the pressure-volume relationship at each point, from which several measures can be generated. The ESPVR curve represents the pressure generated by the ventricle at a given ESV, also known as the end systolic elastance (E_{es}), and can be measured experimentally via occlusion of the inferior vena cava, which shifts the point of aortic valve closure down and to the left as preload is reduced without changing contractility [7]. Arterial elastance (E_A) is the basis for afterload and describes the pressure increase needed for the aorta and downstream arteries to accept ejected blood. This is shown by the line connecting the point of aortic valve closure with the point of EDV on the x-axis.

When interpreting the meaning of a given measure of cardiac function, it is important to consider the physiological basis for that measurement and how it would affect different features of the cardiac cycle. For example, cardiac output rises during exercise, and this change depends not only on faster HR but on several factors that increase stroke volume. Sympathetic pathways increase contractility, shown by the end systolic pressure volume relationship (ESPVR) and results in lower ESV, while higher venous return leads to increased preload and EDV, moving the point of mitral valve closure higher along the ventricular elastance or end diastolic pressure-volume relationship (EDPVR) curve [8]. Conversely, stroke volume is reduced in hypertensive patients as afterload and ESV are higher, and in hypertrophic patients with reduced ventricular compliance as preload and EDV are lower [9].

Ventricular function can be measured several different ways, some of which are presented in **Table 2**, and can describe either systolic or diastolic function. Ventricular ejection fraction (EF) is among the most commonly used measures of cardiac function, but is not a direct measure of ventricular contractility or systolic function. EF can be influenced as much by preload, afterload, and diastolic function as it is by the contractility of the myocardium, so when EDP, EDV, and systemic vascular resistance are not known, there is not proper context for making reliable assessments of systolic function based on EF alone [10]. As patients with larger ventricles will have a larger

stroke volume when EF is held constant, stroke volume index (SVI) is often used to normalize ventricular output to body surface area (BSA), along with end systolic volume index (ESVI) and end diastolic volume index (EDVI) [11].

Common measures of ventricular systolic function include positive systolic wave (s' velocity), a measure of longitudinal contraction rate, torsion or twist, which measures the twisting between the base and apex that forms a healthy contraction, and strain, a dimensionless measure of axial or longitudinal shortening relative to initial length. Strain depends on the degree of myocyte shortening, is often normalized to systolic BP as a means of relating ventricular shortening to afterload, and can be measured regionally or as global longitudinal strain (GLS) [12]. Diastole is an active process that occurs in stages: isovolumetric relaxation, early rapid ventricular filling, diastasis, and finally atrial contraction. Dysfunctional ventricular filling changes the velocity profile of mitral inflow during early filling (E wave), driven by ventricular relaxation, and late filling (A wave), driven by atrial systole [13]. While direct measurement of ventricular filling pressures

Measure	Unit	Common Methods	Mathematical Formula
Left Ventricular Ejection Fraction (LVEF)	%	Ultrasound, CT, MRI	$LVEF = ([LVEDV - LVESV] \div LVEDV) \times 100$
Stroke Volume Index (SVI)	mL/m ²	Ultrasound, CT, MRI	$SVI = SV \div BSA$
End Diastolic Volume Index (EDVI)	mL/m ²	Ultrasound, CT, MRI	$EDVI = LVEDV \div BSA$
End Systolic Volume Index (ESVI)	mL/m ²	Ultrasound, CT, MRI	$ESVI = LVESV \div BSA$
LV Contractility (dp/dt)	mmHg/s	Ultrasound, Catheterization	Maximum dp/dt in LV during isovolumetric contraction
Strain	Ratio	Ultrasound	$Strain = \Delta L / L_0$ $L_0 = \text{initial length}$
Systolic Myocardial Velocity (s')	cm/s	Ultrasound	
End Systolic Elastance (E_{es})	mmHg/mL	Ultrasound	$P_{es} = E_{es} \times (V - V_0)$ P-V relation slope at end systole
Isovolumic Relaxation Time (IVRT)	ms	Ultrasound, CT, MRI	$IVRT = t(\text{AV closure}) - t(\text{MV opening})$
LV Filling (E/e')	Ratio	Ultrasound	E: early mitral inflow velocity e': mitral annular diastolic velocity

Table 2: Common measurements of left ventricular systolic (LVEF, SVI, ESVI, LV Contractility, s' , E_{es}) and diastolic (EDVI, IVRT, E/e') function.

require invasive catheterization, commonly used non-invasive measures of diastolic filling include are the E/A ratio, which decreases with impaired relaxation, the E/e' ratio, which is given by the ratio of mitral peak inflow velocity during early filling to early diastolic mitral annular velocity (rate of long-axis stretching), and isovolumic relaxation time (IVRT) which is measured from closure of the aortic valve to opening of the mitral valve. Many other measurements exist to describe systolic and diastolic function, with the appropriate indicator determined by the pathology in question.

In response to ageing and disease, the heart will experience difficulties that affect different areas and different parts of the cardiac cycle, creating a need for a diverse range of measurement tools that are capable of detecting these changes. Decreased EF or SVI can occur with systolic heart failure, as decreased systolic function can increase ESV while EDV remains mostly unchanged [14]. This occurs partially due to decreased contractility, in which case GLS can be a useful measure when normalized to systolic BP [15] Meanwhile, in acute myocardial infarction (MI), restriction of blood often affects a certain segment of ventricular wall perfused by the blocked vessel, in which case regional strain and the appearance of regional wall motion abnormalities provide a more detailed view of which parts of the wall are compromised, and may provide information about the source of the dysfunction. Not all cardiovascular dysfunction results in decreased contractility or EF. In diastolic heart failure EF is often preserved, as the primary dysfunction occurs during filling and leads to reduced EDV. While the various pathologies that lead to heart failure with reduced ejection fraction (HFREF) have been described extensively, the etiologies of heart failure with preserved ejection fraction (HFPEF) are not as well understood and are the focus of intense research interest [16, 17]. Cardiovascular dysfunction is often preceded or accompanied by anatomical changes to the overall mass and size of the heart and its chambers, as is the case with ventricular hypertrophy and dilated cardiomyopathy [18, 19]. These changes can be detected with more basic measurements of chamber cavity size and wall thickness.

Many of the most common cardiac pathologies stem from inadequate blood flow, whether from endothelial and vascular dysfunction, obstructive plaques, thrombotic events, or other causes. Cardiac dysfunction in turn leads to reduced blood flow,

creating a positive feedback loop that often ends in heart failure [20]. Endothelial and cardiac function are closely linked due to the expansive role of the endothelium in regulating local blood flow, nutrient delivery, inflammation, and hemostasis and thrombosis [21]. This relationship is especially significant in the coronary vasculature, where autoregulation, or the ability of a vascular bed to regulate changes in local blood flow, is necessary for the heart to adapt to changes in demand and myocardial oxygen consumption [22]. Endothelial dysfunction, which occurs in response to a variety of causes such as atherosclerosis and insulin resistance, limits the ability of the coronary arteries to vasodilate and increase flow at higher cardiac outputs [23, 24]. The endothelium can also be a source of cardiac dysfunction through atherothrombotic events, which are most often the cause of MI. In the case of MI, the aftermath of ischemia and reperfusion feeds back on the endothelium leading to endothelial inflammation and acceleration of atherosclerosis [25]. The relationship between endothelial and cardiac function is a recurring theme throughout this thesis, which presents a framework for characterizing the cardiovascular system in a holistic manner that relates distinct but connected physiologic processes. Just as cardiac dysfunction is not monolithic, endothelial dysfunction can present differently depending on etiology. As such, the manner in which endothelial and cardiac disease pathways overlap and influence each other can vary greatly, and a holistic approach allows researchers and clinicians to break down cardiovascular pathologies into distinct processes and describe the relationship between them.

Endothelial and Vascular Anatomy and Physiology

Outside of the heart, the endothelium is perhaps the most critical component in the overall health and maintenance of the cardiovascular system. Forming the inner lining of blood vessels, the vascular endothelium provides a physical barrier between the blood pool and all other tissue, and has a number of essential roles in cardiovascular function and homeostasis, including facilitation of nutrient delivery, regulation of local blood flow based on changing metabolic needs, mediation of local and global inflammatory processes, and promotion of hemostasis [26]. As the endothelium is a primary determinant of vascular health, it is at the center of many vascular pathologies, including atherosclerosis, hypertension, and thrombosis.

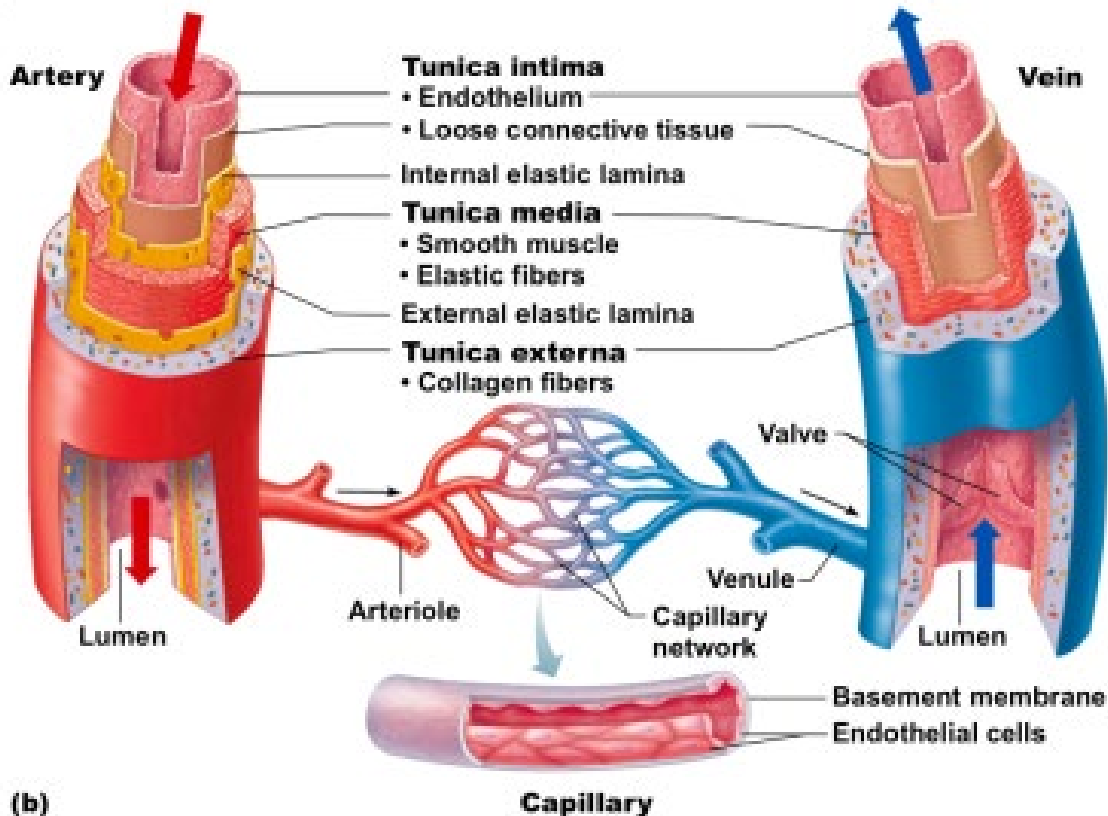


Figure 5: Illustration of arterial, venous and capillary anatomy. Elastic arteries contain additional connective tissue and smooth muscle cells compared to veins, while many veins contain valves to prevent backflow. Capillaries are composed simply of endothelial cells surrounded by a basement membrane. [30]

Additionally, endothelial physiology factors into many non-vascular pathologies such as cancer, bacterial and viral infections, and diabetes mellitus [27].

The endothelium is composed of a single layer of endothelial cell joined together through a network of adherens junctions, tight junctions, and PECAM-1, the latter of which is involved in maintenance and repair of endothelial cell junctions. Variation in junction distribution allows for a modular barrier that depends on local needs, such as in the brain where tighter cell-cell junctions create the blood brain barrier as an added layer of protection against infection and infiltration of toxic compounds [28]. The luminal surface of the endothelium is characterized by a glycolipid and glycoprotein coating, approximately 50-100 nm thick, called the glycocalyx. The glycocalyx contains a number of enzymes and receptors involved in vascular homeostasis, and prevents coagulation and leukocyte adhesion under normal circumstances, in part through nitric

oxide signaling [29]. Together with the endothelium, the arterial elastic lamina in the subendothelial space, rich in collagen, laminin, and fibronectin, forms the tunica intima, as shown in **Figure 5**, which illustrates arterial, venous, and capillary structure. Moving outwards towards the tunica media, smooth muscle cells (SMC) and elastic fibers form the tunica media, which allows for vasodilation through its elasticity and for vasoconstriction through SMC constriction. The tunica adventitia is the outmost layer of arteries and veins and is primarily composed of connective tissue such as collagen, but in large veins and elastic arteries also includes the vaso vasorum, a small-vessel network that provides blood flow to the vascular walls. As capillaries are intended for gas and nutrient exchange, their walls are relatively thin and are composed only of the endothelial layer and a basement membrane [26].

Regulation of Blood Flow

Endothelial cells play a role in regulating blood flow to different tissue beds through nitric oxide signaling that constricts and relaxes the smooth muscle layer of a given arterial segment to change resistance, and by extension, blood flow, to match oxygen demand. Surface proteins on endothelial cells that act as mechanotransducers detect shear forces to determine blood flow, driving downstream processes for optimization of local blood flow [23].

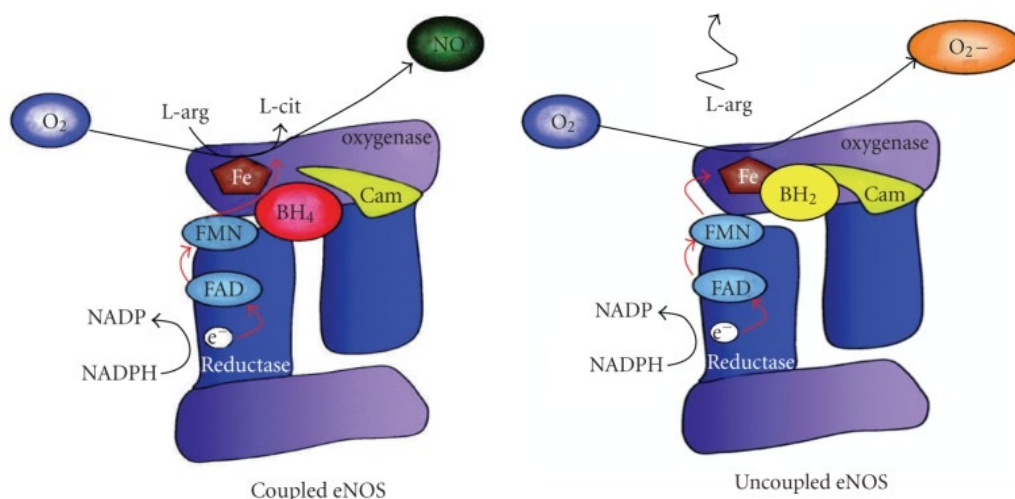


Figure 6: Molecular pathways of coupled and uncoupled eNos. When BH₄ is present, eNOS is coupled and produces NO, while uncoupled eNOS produces superoxide. Production of NO also relies on the presence of L-arginine, which is converted to L-citrulline in the process [32].

Endothelial-driven vasodilation in response to shear stress or cholinergic signaling, among other triggers, occurs through calcium-dependent phosphorylation and activation of endothelial derived nitric oxide synthase (eNOS), which produces nitric oxide (NO), an endothelial derived hyperpolarizing signal responsible for driving smooth muscle cell contraction through production of cyclic guanosine monophosphate (cGMP) [23]. This process, shown in **Figure 6**, requires coupling of eNOS, stabilized by the cofactor tetrahydrobiopterin (BH₄), which then converts oxygen and L-arginine to NO and L-citrulline [31]. Under pathologic conditions, this pathway can be disturbed, leading to attenuated NO formation and a reduction in maximal flow. This phenomenon can be driven by dysfunction at several different nodes in the blood flow regulatory pathway. For example, oxidation of tetrahydrobiopterin (BH₄) in the presence of reactive oxygen species (ROS) results in uncoupling of eNOS and a shift from NO production to production of superoxide, which has additional harmful effects besides reduced blood flow.

Endothelial-driven vasoconstriction, meanwhile, occurs primarily through angiotensin II and TNF α , which promote endothelin-1 dependent SMC contraction, suppress eNOS activity directly, and suppress the PI3 kinase-Akt pathway which serves as an upstream promoter of eNOS [33]. There is much interaction between the various vasomotor pathways, which allows for incorporation of feedback mechanisms and precise control. For example, endothelin-1 as well as other members of the endothelin family bind to the endothelin-A and endothelin-B receptors, which both have vasoconstrictive effects, but have differing affinities for different endothelin subtypes. Endothelin-B can also promote NO formation, allowing for tight control of vascular tone through modulation of endothelin signaling [34].

Vasomotor dysfunction, especially at the microvascular level, is prevalent in vascular diseases such as atherosclerosis as well as in smokers and patients with systemic diseases such as obesity, diabetes mellitus, and metabolic syndromes [27, 35, 36]. In atherosclerosis, inflammatory signaling suppresses NO production while oxidative stress promotes eNOS uncoupling. Endothelial insulin receptors interact with both the vasodilation-favoring PI3-kinase pathway and the vasoconstriction-favoring MAP-kinase and endothelin-1 pathway [37]. Insulin resistance and diabetes mellitus

adversely impacts the vasodilation pathways relative to vasoconstrictive pathways, while also promoting endothelial dysfunction through glucotoxicity and inflammation.

Clinically, endothelial dysfunction can be assessed by measuring changes in blood flow in response to stimuli such as acetylcholine, but degree of dysfunction can vary depending on the vascular bed [38]. Flow-dependent vasodilation is also used to assess vasomotor function and involves ultrasound doppler imaging of changes to arterial diameter during reactive hyperemia, or a rapid and short-lived increase in flow following vascular occlusion [39]. Measurement of blood biomarkers for inflammation, oxidative stress, and pro-coagulant factors can provide context regarding the etiology of endothelial dysfunction. In pre-clinical research, arterial ring assays allow for measurement of vasomotor function in excised arterial segments in order to identify the source and extent of endothelial dysfunction and are discussed in Chapter 2 [40].

Coronary Vascular Physiology

The ability of arteries to auto-regulate is especially important for coronary blood flow, as the heart has remarkably high basal oxygen demand and the highest degree of oxygen extraction, as measured by arteriovenous oxygen difference [41]. The heart is also unique in that perfusion primarily occurs during diastole due to compression during systole under high ventricular pressures, a factor that makes the myocardium, highly sensitive to ischemia, specifically in the subendocardium where pressures during systole are highest [22]. Coronary perfusion is also sensitive to heartrate as rising heartrates decreases the ratio of time spent in diastole versus systole [42]. Mechanisms for regulation of coronary perfusion vary at different parts of the vascular tree. In large coronary arteries, which provide only 5% of total coronary vascular resistance at rest, endothelial mechanisms described above predominate [22, 24]. The coronary arterioles, which are responsible for approximately 60% of resistance at rest, serve as resistance vessels that maintain perfusion pressure, or the flow-driving pressure gradient between aortic diastolic pressure and LVEDP. Arteriolar autoregulation depends on both endothelial and myogenic control mechanisms, with the former found in smaller arterioles (80-100 μ m) and the larger predominating in larger arterioles (200-400 μ m) [43]. Myogenic control of vascular tone occurs through stretch receptor stimulation of

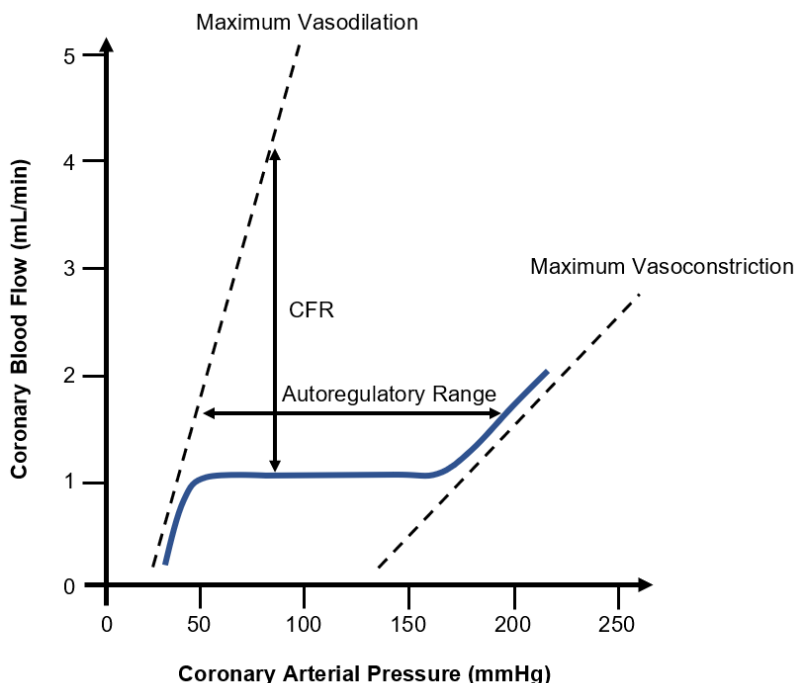


Figure 7: Coronary perfusion and autoregulation. Coronary flow reserve (CFR) is indicated by the difference between actual and maximal blood flow. The autoregulatory range encompasses all perfusion pressures at which coronary blood flow is constant and vascular tone falls between maximum vasodilation and maximum vasoconstriction.

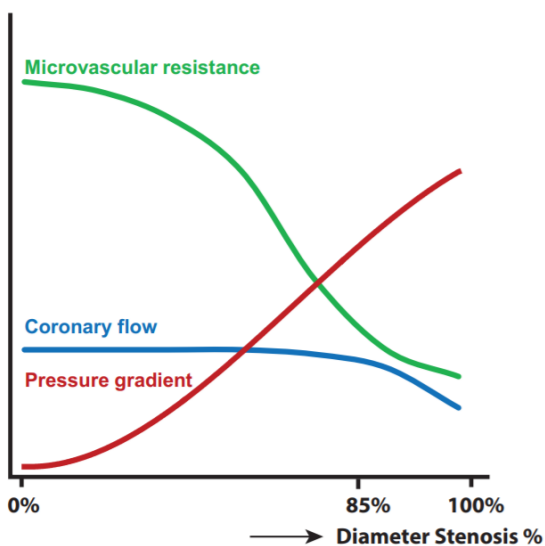
smooth muscle cells in response to changes in blood pressure. Metabolic control of vasomotor function dominates in the precapillary arterioles ($40\mu\text{m}$), where SMCs react to changes in O_2 , CO_2 , ATP, and adenosine.

The coronary capillaries, which hold 90% of the myocardial blood volume, contribute approximately 25% of coronary vascular resistance, with the remaining 10% coming from the venous system. The relative contributions to resistance along the vascular tree changes during exercise, when resistance vessels dilate and shift more resistance to the capillaries and veins [44]. Autoregulation, which is represented graphically in **Figure 7**, allows for pressure-independent regulation of flow coupled to myocardial oxygen demand within the autoregulatory range. Outside of the autoregulatory range, coronary blood flow is mostly pressure dependent.

Understanding of coronary autoregulation is essential for assessment of the narrowing of arteries seen in coronary stenosis. Coronary stenosis in atherosclerotic patients is difficult to detect at rest because downstream arterioles will vasodilate to

compensate for the increased resistance and pressure drop at the site of stenosis. This limits the impact of stenosis on resting blood flow in all but the most severe cases (>85-90% stenosis) [44]. However, during exercise, resistance vessels are already dilated to accommodate the increased myocardial oxygen demand, and their ability to compensate for upstream stenoses is diminished with increasing degree of stenosis, as seen in **Figure 8** [45]. Thus, it is possible to detect less severe stenosis after exercise or infusion of a pharmacologic stress agent.

Resting conditions



Hyperemic conditions

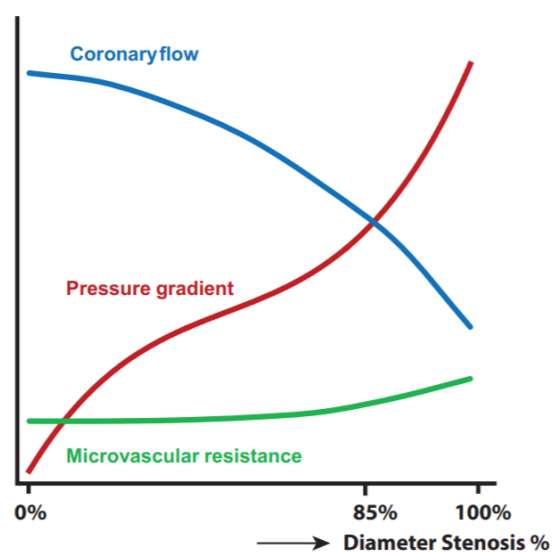


Figure 8: Relationship between degree (%) stenosis and microvascular resistance, coronary blood flow, and pressure gradient at rest and stress (hyperemia). Note that at rest, coronary blood flow is maintained when degree of stenosis is less than ~85% as the microvasculature undergoes vasodilation to compensate. In hyperemic conditions, microvascular resistance is already minimized for increased flow, and reduction in coronary blood flow is roughly proportional to degree of stenosis [44].

Hemostasis and Thrombosis

The intact endothelial barrier prevents coagulation of blood in the absence of a wound through production of anti-thrombotic signals. When this barrier is disrupted, such as in the case of trauma, nearby blood undergoes coagulation to create a stable clot and prevent further blood loss in a process known as hemostasis. Coagulation involves a series of self-amplifying reactions that activate soluble factors in the blood and eventually lead to deposition of fibrin, an activated form of the protein fibrinogen, which forms a crosslinked net over the wound [46, 47]. This process can proceed

through one of two pathways, known collectively as the coagulation cascade, which is shown in **Figure 9**. The intrinsic (contact activation) pathway, proceeds through exposure of subendothelial collagen, while the extrinsic (tissue factor) pathway is triggered by release of tissue factor from smooth muscle cells, fibroblasts, and other subendothelial tissue. The net result of the coagulation cascade is activation of thrombin, and extremely potent driver of fibrin activation and cross-linking.

The endothelium itself regulates coagulation through several mechanisms, most of which overlap with vasomotor control and inflammatory pathways, which are tightly linked processes. Pro-inflammatory factors can promote coagulation and vasoconstriction, pro-coagulant factors have pro-inflammatory and vasoconstrictive effects, and vasoconstrictive factors can augment inflammation and coagulation [48].

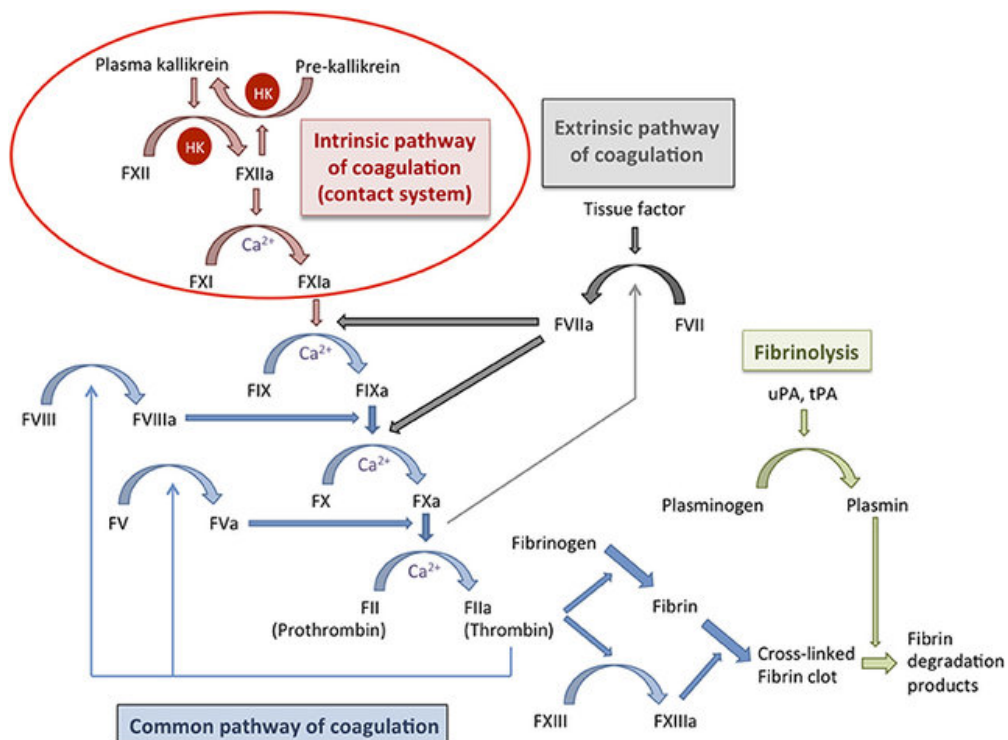


Figure 9: Schematic of coagulation cascade featuring the intrinsic and extrinsic pathways. Extrinsic pathway activation occurs through release of tissue factor while the initiating event for the intrinsic pathway is the exposure of subendothelial collagen. Both pathways converge downstream and result in formation of cross-linked fibrin nets [49].

The reverse is also true. Under healthy conditions, release of NO has anti-thrombotic and anti-inflammatory effects, partially through blockage of Weibel-Palade body release, and also acts against platelet activation and aggregation [50]. Prostaglandins are a family of lipids that, along with other eicosanoid compounds, are derived from arachidonic acid, and play a major role in coagulation, inflammation, and hemostasis. Prostacyclin, or PGI₂, a member of the prostaglandin family released by endothelial cells, is among the most potent endogenous anti-platelet agents as well as a powerful vasodilatory agent [51]. Conversely, thromboxane-A₂ (TXA₂), another member of the prostaglandin family, is primarily secreted by activated platelets but can be released from endothelial cells as well, and exerts pro-coagulant and vasoconstrictive effects [52]. As hemostatic pathways are self-amplifying, it is important to have a mechanism that can turn the process off. Endothelial thrombomodulin attenuates active coagulation through cooperation with activated protein C to convert thrombin in an anti-coagulant factor that inhibits upstream reactions [53].-

Before a stable clot can be formed, an initial platelet plug must be created to prevent further loss of blood and create a scaffold for fibrin deposition. This occurs via binding of platelets to active von Willebrand Factor (VWF) multimers that bind to collagen in the subendothelial space [54]. VWF is a multimeric protein secreted by endothelial cells in an inactive form, that under healthy conditions is cleaved by the metalloproteinase ADAMTS13 at the VWF A2 domain as it is released, leaving short strands of VWF on the endothelial surface and circulating VWF multimers [55]. Upon either binding to collagen or exposure to high shear forces, VWF activates and unfolds to expose its A1 domain, which binds passing platelets via the GPIIb α receptor. In the case of traumatic injury to the vessel wall, VWF forms long strands over the disrupted area so platelets can plug the wound and drive coagulation and construction of a fibrin net. Platelet activation can be triggered by binding to VWF or to collagen through the GPVI receptor, as well as by agonists such as ADP, thromboxane-A₂, and thrombin [56]. Upon activation, platelets release pro-coagulant and pro-inflammatory factors and undergo morphological changes from a disc shape to an irregular spiky shape that is more conducive to binding VWF and forming platelet plugs. Platelet-endothelial

interactions through VWF are of great interest in vascular pathologies and discussed extensively in later chapters.

While hemostasis is a necessary component of vascular health, pathologic coagulation occurring in intact vessels is a major cause of morbidity and mortality through ischemic and embolization events. Thrombosis occurs through similar mechanisms as hemostasis, but rather than forming a wound-healing clot, a clot is formed inside the vessel lumen following a trigger such as rupture of atherosclerotic plaques containing pro-thrombotic factors or through disruption of anti-coagulation pathways that depend on healthy endothelial function and proper blood flow [21, 46]. Such is the case in low-flow areas or areas of recirculation, which are often seen in the atria and atrial appendages, both common sites of thrombosis [57]. As the blood pool contains both anti-coagulant and pro-coagulant factors, the balance can be shifted in favor of the latter in cases of vascular pathologies or cardiovascular dysfunction. These events can cause blockage of a vessel at the site of thrombosis, leading to ischemia, or can result in embolization of a thrombus, which may cause severe problems downstream. Venous thrombi may find their way to the lungs and cause pulmonary embolism, while thrombi formed in the left side of the heart can make their way to the cerebral circulation and cause stroke [58]. Medications such as aspirin, anti-platelet agents, and clotting factor antagonists are useful in preventing thrombosis, but by shifting the balance towards anti-coagulant factors, increase the risk of bleeding [59].

Inflammation and the Endothelium

The inflammatory system relies on the endothelial layer to signal a nearby problem and recruit inflammatory cells to the site of active infection or tissue damage. When a pathogen is detected, pro-inflammatory endothelial activation occurs in the adjacent vasculature, whereby endothelial cells release pro-inflammatory cytokines and endothelial cell adhesion molecules (ECAMs) such as P- and E-selectin, VCAM-1 and ICAM-1 to attract, capture, and activate passing leukocytes which then migrate into the tissue and fight the infection [60, 61]. P-Selectin is stored in Weibel-Palade bodies along with VWF and is released immediately in response to endothelial activation. After

vesicular release of stored pro-inflammatory factors, the endothelium depends on transcriptional upregulation of additional factors, which occurs on the order of hours.

Endothelial activation is mediated through transcriptional factors NF- κ B and activating protease-1 (AP-1) and is often triggered by pro-inflammatory cytokines such as TNF- α and IL-6, among others through the MAP3K pathway [60]. Activated endothelial cells secrete many different cytokines including IL-8, monocyte chemoattractant protein-1 (MCP-1), CCL5 (also known as RANTES), and CXCL3 (fractalkine), which recruit and activate inflammatory cells, promoting firm adhesion and transmigration [62]. Upregulation of ECAM expression mediates the rolling of passing leukocytes and their adhesion to the surface, followed by transmigration and extravasation, partially facilitated by PECAM-1, where leukocytes can then target pathogens or cellular damage [63].

The inflammatory process produces oxidative stress, tissue factor, and matrix metalloproteinases (MMPs), and leads to disruption of the glycocalyx and its associated protective mechanisms, all of which may contribute to VWF dysregulation and link inflammatory processes with platelet-endothelial interactions [48, 64, 65]. Recruited leukocytes interact with platelets through platelet P-selectin and leukocyte PSGL-1, allowing for further mutual activation and recruitment. Upon interacting with the endothelial surface, both platelets and activated leukocytes secrete a number of cytokines that feedback and drive further endothelial activation. Once an inflammatory process begins to die down, endogenous anti-inflammatory mechanisms prevail and return the endothelium to its normal state. However, risk factors such as dyslipidemia, insulin resistance, smoking, or other triggers for endothelial dysfunction, disrupt anti-inflammatory mechanisms, endothelial activation and inflammation can become chronic and lead to vascular pathologies such as atherosclerosis, a process discussed later in this chapter.

Endothelial Dysfunction and Vascular Pathologies

Although the primary roles of the endothelium, as described in the previous section, can be thought of as distinct processes, dysfunction in one of these areas is

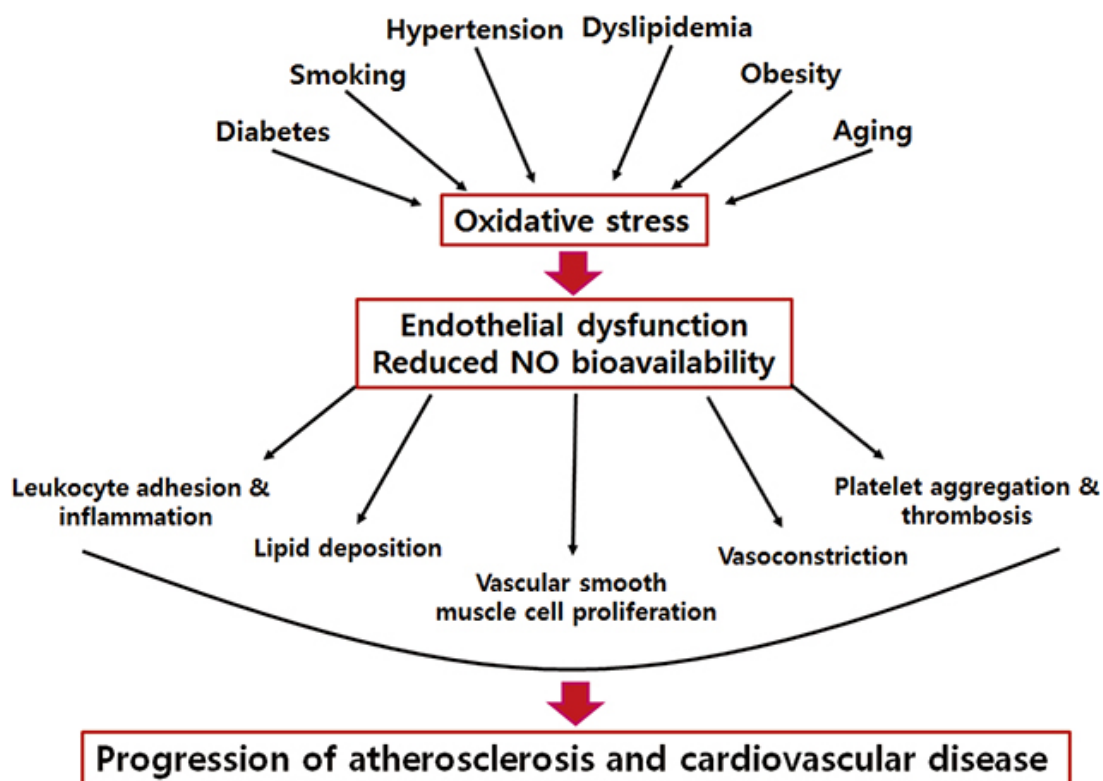


Figure 10: Causes and manifestations of endothelial dysfunction. The risk factors shown here lead to oxidative stress and loss of NO bioavailability in the short-term, which is accompanied by loss of many endothelial protective mechanisms. Sustained endothelial dysfunction is a main driver of atherosclerosis [66].

often accompanied by dysfunction in the others. While in practice, description of endothelial phenotype is far more nuanced, endothelial phenotype can in the simplest terms be thought of as a binary model: healthy or dysfunctional. The healthy endothelium is an anti-oxidant, anti-inflammatory, anti-thrombotic and vasoactive environment, while the dysfunctional endothelium is characterized by oxidative stress, inflammation, increased risk of thrombosis, and loss of vascular reactivity and vasodilatory capacity. Endothelial dysfunction, the basic mechanism of which is shown in **Figure 10**, can be developed in response to many different stressors that impair endothelial protective mechanisms, such as smoking, dyslipidemia, diabetes, obesity, and hypertension [27, 66]. The loss of NO bioavailability from eNOS uncoupling as well as loss of other cardioprotective mechanisms creates the ideal environment for progression of vascular pathologies such as atherosclerosis and thrombotic microangiopathies.

Atherosclerosis and Myocardial Infarction

Cardiovascular disease encompasses many different pathologies including acute events such as MI and chronic conditions such as cardiomyopathies. In the case of MI, which is caused by a blockage of blood flow within the coronary vasculature, damage to heart muscle and associated structures may lead to chronic conditions, as in the case of ischemic heart failure, which is the leading cause of death in the United States. The primary triggers of myocardial ischemia are atherothrombotic events, which is the formation of a blood clot from an atherosclerotic plaque [67]. Atherosclerosis can occur in the coronary vasculature, where it is referred to as coronary artery disease (CAD), as well as the peripheral vasculature (peripheral arterial disease, PAD) and the cerebral vasculature (cerebrovascular disease), and can lead to ischemic events in any of these vascular beds.

Atherosclerosis is a chronic inflammatory disease that can begin in childhood or adolescence and develops over decades in response to a diverse range of genetic and lifestyle risk factors. Common risk factors include dyslipidemia, hypertension, obesity, diabetes mellitus, tobacco use, hyperhomocysteinemia, and many others. The composition of atherosclerotic lesions varies based on both disease stage, depicted in **Figure 11**, and driving risk factors, which can lead to distinct atherosclerotic phenotypes. Atherogenesis is triggered by endothelial injury in the setting of vascular risk factors and excess low-density lipoprotein (LDL), which accumulates in the subendothelial space and undergoes oxidative modification to form ox-LDL. Ox-LDL and other oxidized lipoproteins cause inflammation of vascular wall, marked by endothelial activation and recruitment of leukocytes, specifically monocytes which enter the vessel wall and eventually become lipid-engorged macrophages known as foam cells [69]. The subendothelial collection of foam cells forms a fatty streak, the earliest histologic sign of a nascent atherosclerotic lesion. Foam cell accumulation of ox-LDL through scavenger receptors, pinocytosis of LDL, and binding of ox-LDL on other modified lipoproteins to Toll-like-receptors (TLRs), lead to pro-inflammatory cytokine release, proliferation of macrophages, and additional myeloid cell recruitment, some of many sources of positive feedback in atherogenesis. Among the pro-inflammatory cytokines released is IL-1 β , a potent driver of downstream inflammatory signaling

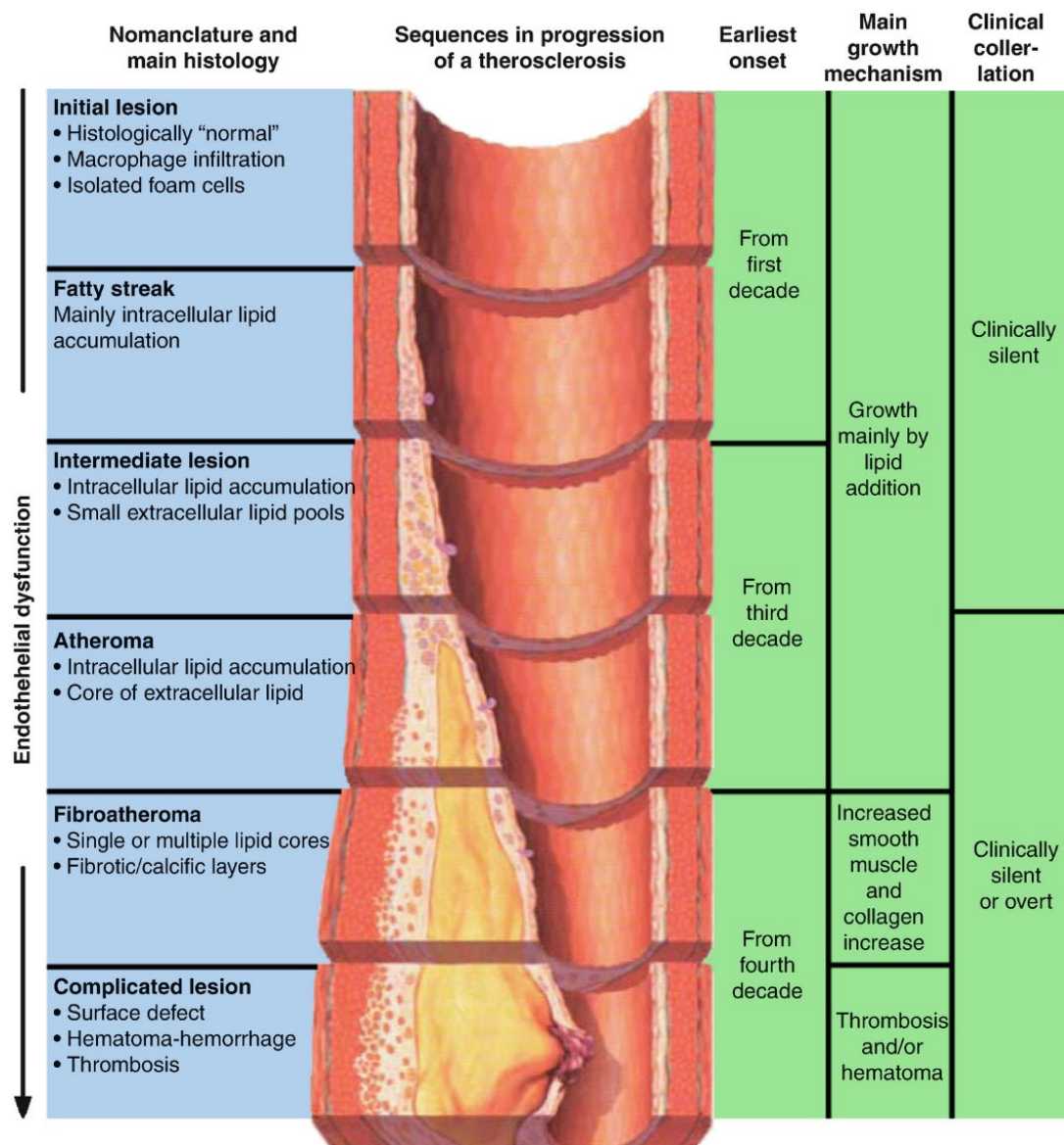


Figure 11: Stages of atherosclerotic plaque development from formation of initial lesions and fatty to streaks to progressively advanced lesions. Degree of endothelial dysfunction increases along with lesion progression. Atherosclerotic plaques are mostly clinically silent until later disease stages [68]

activated in part by formation of cholesterol microcrystals that form within foam cells [70].

Macrophages are a primary driver of atherosclerotic lesion formation, but the adaptive immune response is also involved. T cells, recruited to the endothelial surface in part through chemokine receptor type 5 (CCR5), and have been observed to be involved in secretion of pro-inflammatory cytokines in the setting of

hypercholesterolemia, constituting as much as 20-40% of plaque leukocyte content [72]. B lymphocytes serve to both regulate T cell activity and secrete antibodies, which can have atheroprotective or pro-atherogenic effects. Secretion of IgM proteins by B1a B lymphocytes, for example, can reduce ox-LDL recruitment by macrophage scavenger receptors [73], while IgE released by several classes of B cells promote activation of macrophages and mast cells [74].

Fatty streak formation is followed by proliferation and migration of SMCs to the lesion, which mediate fibrosis and plaque progression along with vascular fibroblasts [75]. After sufficient intracellular accumulation of lipid droplets and microcrystals by foam cells, apoptosis begins to take hold among the resident leukocytes, forming a necrotic core rich in extracellular lipid pools and proinflammatory and prothrombotic factors. Foam cell necrosis significantly aggravates the already disturbed endothelium, by which point endothelial atheroprotective mechanisms have been overwhelmed and reversal of plaque growth is unlikely [76].

The development of atherosclerotic plaques is not a smooth, continuous process, but instead one characterized by phases of rapid growth between periods of relative quiescence [77]. Potential destabilization events that trigger these rapid growth phases include intraplaque hemorrhage and release of pro-thrombotic factors within the microvascular network that supplies the plaque, superficial erosion of the plaque surface, leading to platelet aggregation and micro-thrombus formation, and disruption of the plaque fibrous cap which protects the nearby blood pool from thrombogenic factors in the lipid core [75]. Inflammation drives many plaque-disrupting events, through mechanisms such as induction of endothelial apoptosis or endothelial cell attack by killer T cells. Pro-inflammatory cytokines also trigger secretion of MMPs which can degrade the protective fibrous cap [78].

While the cholesterol and inflammatory pathways of atherogenesis described above are well characterized and the target of most preventative therapies, a parallel pathway for plaque growth involving platelet-endothelial interactions, shown in **Figure 12**, has more recently emerged, in part thanks to the techniques described in later chapters. In a normal vessel, VWF multimers are kept short and inactive, only binding

platelets and forming a plug when the endothelial layer is disrupted. However, in the setting of oxidative stress, VWF can become oxidatively modified at the A2 domain, rendering it resistant to cleavage by ADAMTS13, which can also be oxidatively modified and rendered inactive [79, 80]. When the VWF cleavage process is impaired, ultralong VWF (ULVWF) multimers form and become shear activated, binding platelets in the process. Bound platelets amplify endothelial activation through secretion of pro-inflammatory and pro-thrombotic factors, and are involved in both indirect and direct monocyte recruitment. The role of platelet-endothelial interactions in atherosclerosis is further explored in Chapters 5 and 6.

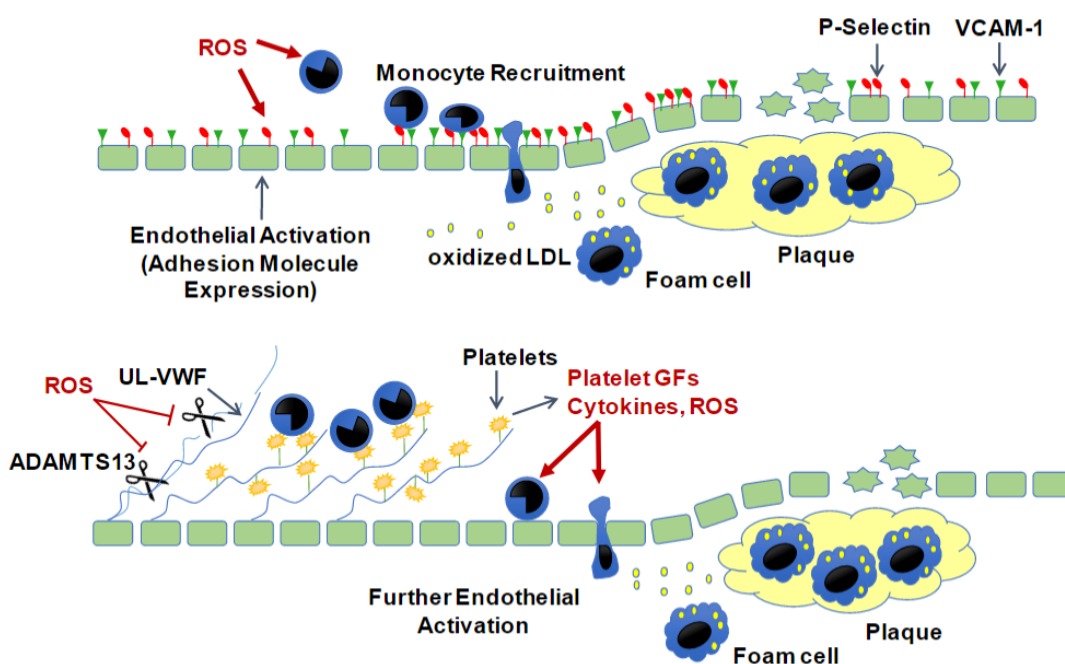


Figure 12: Canonical pathway of lipid accumulation and inflammation as drivers of atherosclerosis (top) and more recently discovered pathway driven by platelet-endothelial interactions secondary to oxidative modification of VWF and ADAMTS13 leading to ULVWF accumulation. These pathways are somewhat distinct but have significant signaling overlap.

Atherosclerotic plaque growth takes decades and can end with one of several phenotypes. While plaques initially expand outward, some plaques progress enough to begin encroaching on the lumen, leading to stenosis and reduced blood flow. Some plaques will have large lipid and necrotic regions and thin fibrous caps, putting them at risk for rupture and thrombosis, while others may be primarily composed of smooth muscle cells and collagen. Plaques are distributed throughout the arterial tree, both in

the coronary and peripheral circulation, and may form in proximal large arteries, often at branch points, leading to stenosis or thrombosis or may occur more diffusely in smaller arterioles, leading to microvascular dysfunction.

The propensity of a plaque to rupture or undergo surface erosion, which causes atherothrombotic ischemic events, is hard to predict and not necessarily based on size, as many so-called culprit lesions are not large enough to be visible by traditional imaging methods [81]. In fact, atherosclerotic plaques are not easily detected on non-invasive imaging until late in the process, often after decades of unchecked growth, and at a point where no therapies exist to reverse the process. While plaques initially form outwards from the lumen, evidenced by early intimal-medial thickening, as plaques progress they begin to encroach on the lumen. Only late-stage plaques can generally cause degree of stenosis sufficient to detect with conventional medical imaging methods such as angiography, although advancements in intravascular ultrasound (IVUS) are leading to improved detection of subclinical atherosclerosis [82]. In the absence of earlier detection methods, clinicians rely on risk stratification so patients at a high risk are assigned early on to therapies that prevent growth.

When an acute thrombotic event occurs within the coronary circulation and prevents blood from reaching the cardiac muscle, it triggers a number of local and global downstream effects. Locally, hypoxia sets in, with the endocardium the most vulnerable to changes in blood flow and the first to see decreases in systolic function [83]. As the time of ischemia continues, dyskinesia spreads from the endocardium to the epicardium, and in the case of a severe ischemic event, known as a transmural infarct, the entire thickness of the heart wall in the affected region is affected [84]. The severity and duration of ischemia, determined mostly by the location of blockage and time to reperfusion, determine the ultimate extent of the damage to the heart muscle [85]. In the best scenarios, damage is reversible and normal systolic function resumes once proper blood flow is restored. In the worst cases, cardiomyocytes undergo necrosis and the physiological response to this, including splenic release of monocytes and a burst of reactive oxygen species, pro-thrombotic and pro-inflammatory factors, and apoptotic bodies can have deleterious effects on the entire vasculature that lead to acceleration of atherosclerosis. This process is reviewed in more detail in Chapter 6. Atherothrombotic

events in the peripheral and cerebral vasculature can also cause ischemia, and their impact on remote vessels can also potentially accelerate atherosclerosis due to similar systemic responses to ischemia and tissue necrosis.

Thrombotic Microangiopathies

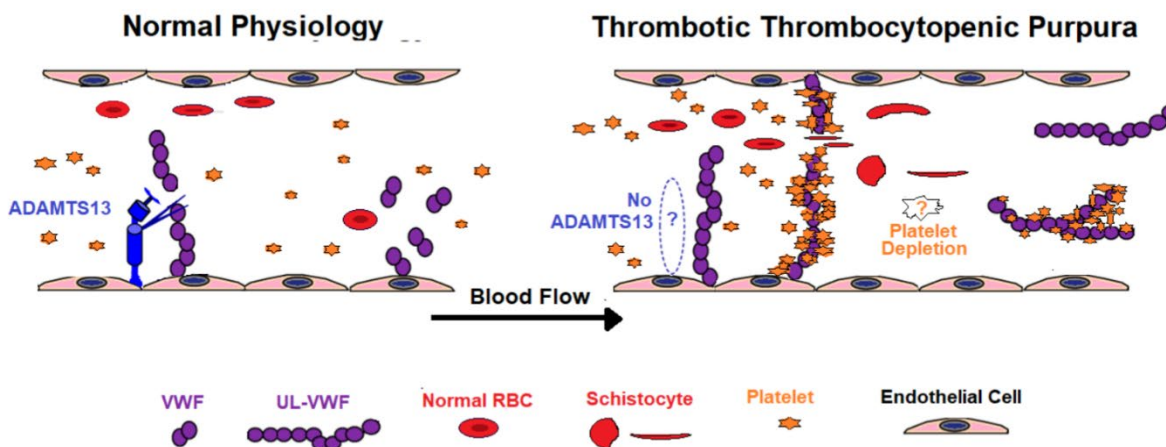


Figure 13: Microvascular physiology in normal vessels and in thrombotic thrombocytopenic purpura (TTP). TTP leads to microthrombus formation, hemolysis and fragmentation of erythrocytes (schistocytes), and platelet depletion through consumption by thrombotic processes.

One of the consequences of endothelial dysfunction is impairment of anti-thrombotic protective mechanisms and buildup of ULVWF multimers. While major ischemic events such as MI and stroke are caused by large occlusive thrombi, thrombotic processes on a smaller and more diffuse scale can also result in cardiac and other organ dysfunction. These thrombotic microangiopathies are characterized by widespread formation of VWF-platelet thrombi in the microvasculature [87, 88]. Thrombi can embolize and lead to diffuse blockages and lead to hemolytic anemia and thrombocytopenia, which is responsible for increased bleeding and the characteristic blood spots or purpura in TTP patients. One such example of this is thrombotic thrombocytopenic purpura (TTP), illustrated in **Figure 13**, caused by inactivation of ADAMTS13, often genetic in origin [89].

While TTP is an acute clinical syndrome, thrombotic microangiopathies and TTP-like processes can contribute to vascular diseases such as atherosclerosis on a less severe, but chronic level [90-94]. Thrombotic processes exist on a spectrum from low-grade systemic platelet-endothelial interactions to acute thrombotic occlusion of major

vessels, but the mechanism of thrombosis is similar across this spectrum. As recombinant ADAMTS13 therapy and treatments that reduce VWF dysregulation show promise in TTP patients [95, 96], these therapies are explored in later chapters for potential in more chronic applications such as atherosclerosis and cardiotoxicity of certain cancer medications.

Conclusion

Healthy cardiovascular function depends on a number of complex and interacting systems. Proper endothelial function is necessary for maintaining blood flow and cardiac function. Many different cardiovascular pathologies share a common pathway of endothelial activation and dysfunction. Characterizing cardiac and endothelial function in clinical and research settings depend on utilizing a many different techniques targeted at measuring specific functions, but also understanding how these functions interact. This thesis will focus on techniques to visualize and characterize the vascular endothelium but doing so also requires an understanding of cardiac function to contextualize events at the endothelial surface. Many of the imaging techniques, such as the 2D echocardiogram, that are ideal for visualizing cardiac function, are not suitable for characterizing the complex molecular interactions that occur at a microscopic scale at the endothelial surface. The physiological processes detailed in this chapter will form the basis for the different techniques imaging and non-imaging techniques discussed and how they are applied in common disease settings.

References

1. Chappell M, Payne S. Cardiovascular System I: The Heart. *Physiology for Engineers*. 2015;BIOSYSROB, volume 13:81-95.
2. Wiggers Diagram. Wikimedia2017. p. https://commons.wikimedia.org/wiki/File:Wiggers_Diagram.svg.
3. Fukuta H, Little WC. The cardiac cycle and the physiologic basis of left ventricular contraction, ejection, relaxation, and filling. *Heart Fail Clin*. 2008;4(1):1-11.
4. Ahmad M. Cardiac Cycle , Phases Of Cardiac Cycle, Cardiac Cycle & ECG. 2019. p. <https://www.medicosite.com/cardiac-cycle/>.
5. Magder S. Volume and its relationship to cardiac output and venous return. *Crit Care*. 2016;20(1):271-.
6. Sequeira V, van der Velden J. Historical perspective on heart function: the Frank-Starling Law. *Biophys Rev*. 2015;7(4):421-47.
7. Guyton AC, Hall JE. *Medical Physiology: 10th Edition*. Elsevier Health Sciences; 2000.

8. Huang C, Chambers D, Matthews G. Cardiac Pressure–Volume Loops. *Basic Physiology for Anaesthetists*. 2 ed. Cambridge: Cambridge University Press; 2019. p. 136-40.
9. Forstermann U, Munzel T. Endothelial nitric oxide synthase in vascular disease: from marvel to menace. *Circulation*. 2006;113(13):1708-14.
10. Monge García MI, Jian Z, Settels JJ, Hunley C, Cecconi M, Hatib F, et al. Determinants of left ventricular ejection fraction and a novel method to improve its assessment of myocardial contractility. *Ann Intensive Care*. 2019;9(1):48-.
11. Kerkhof PLM, Kuznetsova T, Ali R, Handly N. Left ventricular volume analysis as a basic tool to describe cardiac function. *Advances in Physiology Education*. 2018;42(1):130-9.
12. Chengode S. Left ventricular global systolic function assessment by echocardiography. *Ann Card Anaesth*. 2016;19(Supplement):S26-S34.
13. Smiseth OA. Evaluation of left ventricular diastolic function: state of the art after 35 years with Doppler assessment. *J Echocardiogr*. 2018;16(2):55-64.
14. Omar Alaa Mabrouk S, Bansal M, Sengupta Partho P. Advances in Echocardiographic Imaging in Heart Failure With Reduced and Preserved Ejection Fraction. *Circulation Research*. 2016;119(2):357-74.
15. Rhea IB, Rehman S, Jarori U, Choudhry MW, Feigenbaum H, Sawada SG. Prognostic utility of blood pressure-adjusted global and basal systolic longitudinal strain. *Echo Res Pract*. 2016;3(1):17-24.
16. Park J-H, Marwick TH. Use and Limitations of E/e' to Assess Left Ventricular Filling Pressure by Echocardiography. *J Cardiovasc Ultrasound*. 2011;19(4):169-73.
17. Shah AM, Cikes M, Prasad N, Li G, Getchevski S, Claggett B, et al. Echocardiographic Features of Patients With Heart Failure and Preserved Left Ventricular Ejection Fraction. *J Am Coll Cardiol*. 2019;74(23):2858-73.
18. Losi M-A, Nistri S, Galderisi M, Betocchi S, Cecchi F, Olivotto I, et al. Echocardiography in patients with hypertrophic cardiomyopathy: usefulness of old and new techniques in the diagnosis and pathophysiological assessment. *Cardiovascular Ultrasound*. 2010;8(1):7.
19. Mathew T, Williams L, Navaratnam G, Rana B, Wheeler R, Collins K, et al. Diagnosis and assessment of dilated cardiomyopathy: a guideline protocol from the British Society of Echocardiography. *Echo Res Pract*. 2017;4(2):G1-G13.
20. Causes of Heart Failure: American Heart Association; [Available from: <https://www.heart.org/en/health-topics/heart-failure/causes-and-risks-for-heart-failure/causes-of-heart-failure>.
21. Lerman A, Zeiher AM. Endothelial function: cardiac events. *Circulation*. 2005;111(3):363-8.
22. Goodwill AG, Dick GM, Kiel AM, Tune JD. Regulation of Coronary Blood Flow. *Compr Physiol*. 2017;7(2):321-82.
23. Sandoo A, van Zanten JJCSV, Metsios GS, Carroll D, Kitis GD. The endothelium and its role in regulating vascular tone. *Open Cardiovasc Med J*. 2010;4:302-12.
24. Feliciano L, Henning RJ. Coronary artery blood flow: physiologic and pathophysiologic regulation. *Clin Cardiol*. 1999;22(12):775-86.
25. Dutta P, Courties G, Wei Y, Leuschner F, Gorbato R, Robbins CS, et al. Myocardial infarction accelerates atherosclerosis. *Nature*. 2012;487(7407):325-9.
26. Galley HF, Webster NR. Physiology of the endothelium. *Br J Anaesth*. 2004;93(1):105-13.
27. Rajendran P, Rengarajan T, Thangavel J, Nishigaki Y, Sakthisekaran D, Sethi G, et al. The vascular endothelium and human diseases. *Int J Biol Sci*. 2013;9(10):1057-69.
28. Bazzoni G, Dejana E. Endothelial Cell-to-Cell Junctions: Molecular Organization and Role in Vascular Homeostasis. *Physiological Reviews*. 2004;84(3):869-901.

29. Reitsma S, Slaaf DW, Vink H, van Zandvoort MAMJ, oude Egbrink MGA. The endothelial glycocalyx: composition, functions, and visualization. *Pflugers Arch*. 2007;454(3):345-59.
30. Marieb EN, Hoehn K. *Human Anatomy and Physiology*: Pearson Education; 2013.
31. Alp Nicholas J, Channon Keith M. Regulation of Endothelial Nitric Oxide Synthase by Tetrahydrobiopterin in Vascular Disease. *Arteriosclerosis, Thrombosis, and Vascular Biology*. 2004;24(3):413-20.
32. Chen Q, Kim EEJ, Elio K, Zambrano C, Krass S, Teng JC-w, et al. The Role of Tetrahydrobiopterin and Dihydrobiopterin in Ischemia/Reperfusion Injury When Given at Reperfusion. *Advances in Pharmacological Sciences*. 2010;2010:963914.
33. Jonk AM, Houben AJ, de Jongh RT, Serne EH, Schaper NC, Stehouwer CD. Microvascular dysfunction in obesity: a potential mechanism in the pathogenesis of obesity-associated insulin resistance and hypertension. *Physiology (Bethesda)*. 2007;22:252-60.
34. Sandoval YH, Atef ME, Levesque LO, Li Y, Anand-Srivastava MB. Endothelin-1 signaling in vascular physiology and pathophysiology. *Curr Vasc Pharmacol*. 2014;12(2):202-14.
35. Cui M, Cui R, Liu K, Dong J-Y, Imano H, Hayama-Terada M, et al. Associations of Tobacco Smoking with Impaired Endothelial Function: The Circulatory Risk in Communities Study (CIRCS). *J Atheroscler Thromb*. 2018;25(9):836-45.
36. Hadi HAR, Suwaidi JA. Endothelial dysfunction in diabetes mellitus. *Vasc Health Risk Manag*. 2007;3(6):853-76.
37. Gutiérrez A, Contreras C, Sánchez A, Prieto D. Role of Phosphatidylinositol 3-Kinase (PI3K), Mitogen-Activated Protein Kinase (MAPK), and Protein Kinase C (PKC) in Calcium Signaling Pathways Linked to the $\alpha(1)$ -Adrenoceptor in Resistance Arteries. *Front Physiol*. 2019;10:55.
38. Tousoulis D, Antoniades C, Stefanadis C. Evaluating endothelial function in humans: a guide to invasive and non-invasive techniques. *Heart (British Cardiac Society)*. 2005;91(4):553-8.
39. Alley H, Owens CD, Gasper WJ, Grenon SM. Ultrasound assessment of endothelial-dependent flow-mediated vasodilation of the brachial artery in clinical research. *J Vis Exp*. 2014(92):e52070-e.
40. Muniyappa R, Sowers JR. Role of insulin resistance in endothelial dysfunction. *Rev Endocr Metab Disord*. 2013;14(1):5-12.
41. S R, A K, A. R. *Physiology, Coronary Circulation StatPearls2020* [Available from: <https://www.ncbi.nlm.nih.gov/books/NBK482413/>].
42. Ramanathan T, Skinner H. Coronary blood flow. *Continuing Education in Anaesthesia Critical Care & Pain*. 2005;5(2):61-4.
43. Muller-Delp JM. The Coronary Microcirculation in Health and Disease. *ISRN Physiology*. 2013;2013:238979.
44. de Waard GA, Cook CM, van Royen N, Davies JE. Coronary autoregulation and assessment of stenosis severity without pharmacological vasodilation. *Eur Heart J*. 2018;39(46):4062-71.
45. Lindner JR, Skyba DM, Goodman NC, Jayaweera AR, Kaul S. Changes in myocardial blood volume with graded coronary stenosis. *Am J Physiol*. 1997;272:H567-H75.
46. Wu KK, Thiagarajan P. Role of endothelium in thrombosis and hemostasis. *Annual review of medicine*. 1996;47:315-31.
47. Saba HI, Saba SR. Vascular Endothelium, Influence on Hemostasis: Past and Present. *Hemostasis and Thrombosis*. 2014:14-29.
48. Margetic S. Inflammation and haemostasis. *Biochem Med (Zagreb)*. 2012;22(1):49-62.
49. Loof T, Deicke C, Medina E. The role of coagulation/fibrinolysis during *Streptococcus pyogenes* infection. *Frontiers in cellular and infection microbiology*. 2014;4:128.

50. Krejcy K, Schmetterer L, Kastner J, Nieszpaur-Los M, Monitzer B, Schütz W, et al. Role of nitric oxide in hemostatic system activation in vivo in humans. *Arterioscler Thromb Vasc Biol.* 1995;15(11):2063-7.
51. Smith JB. Prostaglandins and platelet aggregation. *Acta Med Scand Suppl.* 1981;651:91-9.
52. Ellinsworth DC, Shukla N, Fleming I, Jeremy JY. Interactions between thromboxane A₂, thromboxane/prostaglandin (TP) receptors, and endothelium-derived hyperpolarization. *Cardiovascular Research.* 2014;102(1):9-16.
53. Okamoto T, Tanigami H, Suzuki K, Shimaoka M. Thrombomodulin: a bifunctional modulator of inflammation and coagulation in sepsis. *Crit Care Res Pract.* 2012;2012:614545-.
54. Peyvandi F, Garagiola I, Baronciani L. Role of von Willebrand factor in the haemostasis. *Blood Transfus.* 2011;9 Suppl 2(Suppl 2):s3-s8.
55. Lancellotti S, Basso M, De Cristofaro R. Proteolytic processing of von Willebrand factor by adamts13 and leukocyte proteases. *Mediterr J Hematol Infect Dis.* 2013;5(1):e2013058.
56. Yun S-H, Sim E-H, Goh R-Y, Park J-I, Han J-Y. Platelet Activation: The Mechanisms and Potential Biomarkers. *Biomed Res Int.* 2016;2016:9060143-.
57. Hathcock James J. Flow Effects on Coagulation and Thrombosis. *Arteriosclerosis, Thrombosis, and Vascular Biology.* 2006;26(8):1729-37.
58. Bruni-Fitzgerald KR. Venous thromboembolism: An overview. *J Vasc Nurs.* 2015;33(3):95-9.
59. Mega JL, Simon T. Pharmacology of antithrombotic drugs: an assessment of oral antiplatelet and anticoagulant treatments. *Lancet.* 2015;386(9990):281-91.
60. Pober JS. Endothelial activation: intracellular signaling pathways. *Arthritis Res.* 2002;4 Suppl 3(Suppl 3):S109-S16.
61. Golias C, Tsoutsis E, Matziridis A, Makridis P, Batistatou A, Charalabopoulos K. Review. Leukocyte and endothelial cell adhesion molecules in inflammation focusing on inflammatory heart disease. *In Vivo.* 2007;21(5):757-69.
62. Speyer CL, Ward PA. Role of endothelial chemokines and their receptors during inflammation. *J Invest Surg.* 2011;24(1):18-27.
63. Woodfin A, Voisin MB, Nourshargh S. PECAM-1: a multi-functional molecule in inflammation and vascular biology. *Arterioscler Thromb Vasc Biol.* 2007;27(12):2514-23.
64. Weyrich AS, Lindemann S, Zimmerman GA. The evolving role of platelets in inflammation. *J Thromb Haemost.* 2003;1(9):1897-905.
65. Chauhan AK, Kisucka J, Brill A, Walsh MT, Scheiflinger F, Wagner DD. ADAMTS13: a new link between thrombosis and inflammation. *J Exp Med.* 2008;205(9):2065-74.
66. Park K-H, Park WJ. Endothelial Dysfunction: Clinical Implications in Cardiovascular Disease and Therapeutic Approaches. *J Korean Med Sci.* 2015;30(9):1213-25.
67. Libby P, Buring JE, Badimon L, Hansson GK, Deanfield J, Bittencourt MS, et al. Atherosclerosis. *Nature Reviews Disease Primers.* 2019;5(1):56.
68. Heslop CL, editor *Emerging environmental, molecular, and genetic risk factors in stable coronary artery disease* 2009.
69. Ley K, Miller YI, Hedrick CC. Monocyte and macrophage dynamics during atherogenesis. *Arterioscler Thromb Vasc Biol.* 2011;31(7):1506-16.
70. Wolf D, Ley K. Immunity and Inflammation in Atherosclerosis. *Circulation Research.* 2019;124(2):315-27.

72. Jonasson L, Holm J, Skalli O, Bondjers G, Hansson GK. Regional accumulations of T cells, macrophages, and smooth muscle cells in the human atherosclerotic plaque. *Arteriosclerosis*. 1986;6(2):131-8.
73. Kyaw T, Tay C, Krishnamurthi S, Kanellakis P, Agrotis A, Tipping P, et al. B1a B lymphocytes are atheroprotective by secreting natural IgM that increases IgM deposits and reduces necrotic cores in atherosclerotic lesions. *Circ Res*. 2011;109(8):830-40.
74. Sage AP, Tsiantoulas D, Binder CJ, Mallat Z. The role of B cells in atherosclerosis. *Nature Reviews Cardiology*. 2019;16(3):180-96.
75. Libby P. Inflammation in atherosclerosis. *Nature*. 2002;420(6917):868-74.
76. Insull W, Jr. The pathology of atherosclerosis: plaque development and plaque responses to medical treatment. *Am J Med*. 2009;122(1 Suppl):S3-s14.
77. Libby P, Schoenbeck U, Mach F, Selwyn AP, Ganz P. Current concepts in cardiovascular pathology: the role of LDL cholesterol in plaque rupture and stabilization. *Am J Med*. 1998;104(2a):14s-8s.
78. Newby AC. Metalloproteinases and vulnerable atherosclerotic plaques. *Trends Cardiovasc Med*. 2007;17(8):253-8.
79. Chen J, Fu X, Wang Y, Ling M, McMullen B, Kulman J, et al. Oxidative modification of von Willebrand factor by neutrophil oxidants inhibits its cleavage by ADAMTS13. *Blood*. 2010;115(3):706-12.
80. Wang Y, Chen J, Ling M, Lopez JA, Chung DW, Fu X. Hypochlorous acid generated by neutrophils inactivates ADAMTS13: an oxidative mechanism for regulating ADAMTS13 proteolytic activity during inflammation. *J Biol Chem*. 2015;290(3):1422-31.
81. Arbab-Zadeh A, Fuster V. The myth of the "vulnerable plaque": transitioning from a focus on individual lesions to atherosclerotic disease burden for coronary artery disease risk assessment. *Journal of the American College of Cardiology*. 2015;65(8):846-55.
82. Schoenhagen P, Nissen S. Understanding coronary artery disease: tomographic imaging with intravascular ultrasound. *Heart (British Cardiac Society)*. 2002;88(1):91-6.
83. Hoffman JI, Buckberg GD. Pathophysiology of subendocardial ischaemia. *Br Med J*. 1975;1(5949):76-9.
84. Reimer KA, Jennings RB. The "wavefront phenomenon" of myocardial ischemic cell death. II. Transmural progression of necrosis within the framework of ischemic bed size (myocardium at risk) and collateral flow. *Lab Invest*. 1979;40(6):633-44.
85. Hasche Edmund T, Fernandes C, Freedman SB, Jeremy Richmond W. Relation Between Ischemia Time, Infarct Size, and Left Ventricular Function in Humans. *Circulation*. 1995;92(4):710-9.
87. Zheng XL, Sadler JE. Pathogenesis of thrombotic microangiopathies. *Annu Rev Pathol*. 2008;3:249-77.
88. Arnold DM, Patriquin CJ, Nazy I. Thrombotic microangiopathies: a general approach to diagnosis and management. *CMAJ*. 2017;189(4):E153-E9.
89. Sadler JE. Pathophysiology of thrombotic thrombocytopenic purpura. *Blood*. 2017;130(10):1181-8.
90. Theilmeyer G, Michiels C, Spaepen E, Vreys I, Collen D, Vermeylen J, et al. Endothelial von Willebrand factor recruits platelets to atherosclerosis-prone sites in response to hypercholesterolemia. *Blood*. 2002;99(12):4486-93.
91. Lindemann S, Kramer B, Seizer P, Gawaz M. Platelets, inflammation and atherosclerosis. *J Thromb Haemost* 2007;5(Suppl. 1):203-11.
92. Liu Y, Davidson BP, Yue Q, Belcik T, Xie A, Inaba Y, et al. Molecular Imaging of Inflammation and Platelet Adhesion in Advanced Atherosclerosis: Effects of Antioxidant Therapy With NADPH Oxidase Inhibition. *Circ Cardiovasc Imaging*. 2013;6:74-82.

93. Liu Y, Davidson BP, Yue Q, Belcik T, Xie A, Inaba Y, et al. Molecular imaging of inflammation and platelet adhesion in advanced atherosclerosis effects of antioxidant therapy with NADPH oxidase inhibition. *Circ Cardiovasc Imaging*. 2013;6(1):74-82.
94. Shim CY, Liu YN, Atkinson T, Xie A, Foster T, Davidson BP, et al. Molecular Imaging of Platelet-Endothelial Interactions and Endothelial von Willebrand Factor in Early and Mid-Stage Atherosclerosis. *Circ Cardiovasc Imaging*. 2015;8(7):e002765.
95. Rottenstreich A, Hochberg-Klein S, Rund D, Kalish Y. The role of N-acetylcysteine in the treatment of thrombotic thrombocytopenic purpura. *J Thromb Thrombolysis*. 2016;41(4):678-83.
96. Scully M, Knöbl P, Kentouche K, Rice L, Windyga J, Schneppenheim R, et al. Recombinant ADAMTS-13: first-in-human pharmacokinetics and safety in congenital thrombotic thrombocytopenic purpura. *Blood*. 2017;130(19):2055-63.

In-Vitro and Ex-Vivo Techniques in Vascular Research

Summary

Studying molecular interactions in the context of vascular and endothelial pathologies does not require a living system, and many in-vitro and ex-vivo model systems and techniques have been described that allow researchers to investigate specific questions in a controlled environment. This chapter details some of these approaches, including flow chamber and chip-based systems, ex-vivo vascular tension assays, and histological analysis. The principles behind each approach are discussed, as well as specific applications within vascular research. As with other approaches, these techniques have a wide range of applications in pre-clinical research such as identification of pathological molecular and cellular pathways, characterization of vessel morphology and function, testing and optimization of novel therapies or targeted microparticles, and even point-of care diagnostics.

In Vitro Approaches

Flow Chambers

Background and Design

The study of vascular physiology is mostly unique in relation to other systems within the body as many of the core biological processes are heavily influenced by the flow of blood within the vessels [1, 2]. Flow chambers are artificial systems that are used to investigate the influence of different flow state on physiologic processes.

Variations in flow conditions affect countless down-stream processes such as vascular tone, hemostasis and thrombosis, inflammation, nutrient delivery, and waste clearance. Blood pressure and shear rate within the heart and vasculature is relayed to endothelial and associated cells through surface mechano-transducers and play a critical role in health and disease. For example, atherosclerotic lesions are often found at sites of disturbed or low flow such as branch points and curvatures [3]. Thrombotic emboli are seen in these states as well, such as deep vein thrombosis in response to prolonged sitting-induced reductions in flow, or in the atrial appendage where eddies and low-velocity recirculation can create perfect conditions for thrombus formation.

Flow chambers vary in design depending on the application, as for any given research question the geometry, biochemistry, and flow conditions must sufficiently approximate the native setting. Flow chambers range in scale from microfluidic devices to aorta-sized tubing, but size is far from the only design criteria [4-7]. These systems must also be compatible with the measurement device providing a readout. Most often the output is optical microscopy, and the molecules or cells of interest may be fluorescently labelled for identification. Imaging can be performed either under flow or after the fact depending on the study. Many other readouts are also used for flow chamber experiments, especially if the flow chamber design is incompatible with optical imaging. One example of this is the use of a gamma scintillation counter in a biocompatible surface design to measure time-dependent adhesion of radiolabeled particles, cells, or platelets to a bio-engineered surface [8].

For simple applications such as quantifying the influence of shear rate on on/off rates of various ligand-receptor binding interactions or hemostatic pathways, a flow chamber might consist of as little as a pair of parallel plates coated with the ligand or receptor of interest connected to a pump [9]. To study more complex questions and processes, such as assessing the biocompatibility of vascular implants or imaging of leukocyte rolling, researchers may require more intricate flow chamber designs that introduce tubing with curvatures or branching, endothelial or smooth muscle cell coated and micro-patterned surfaces, and pulsatile flow pumps [10, 11]. **Figure 1** shows an example of a typical simple flow chamber loop.

Engineering the surface of a flow chamber system is rarely a simple task. A large amount of optimization is often needed to ensure the system most closely approximates a native environment, and this task can be especially difficult when creating a cell coated surface. As with standard cell culture, the incubation conditions have a significant effect on the cell phenotype, but culturing cells in a flow chamber involves additional considerations. In traditional cell culture approaches, a major consideration is the physical characteristics of the growing substrate, which affects cell anchoring and proliferation, among other properties. In cell-coated flow chambers, researchers must additionally consider how cells will attach, proliferate, and behave under different flow and shear conditions. For example, endothelial cells depend on native shear conditions in order to assume a healthy and functional phenotype, so incubation must often take place under flow [1]. Cells can be seeded in suspension or through micro-patterning, with the latter approach often used to ensure proper orientation and spacing.

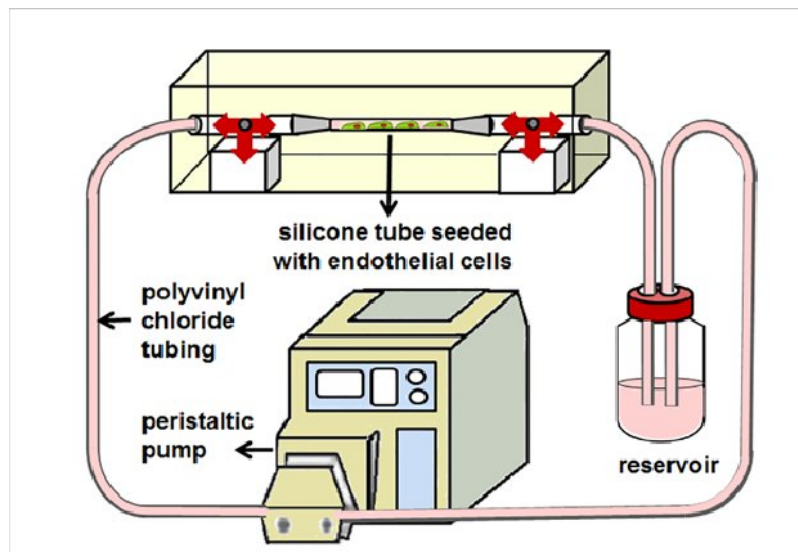


Figure 1: Example flow chamber loop containing peristaltic pump, tubing, endothelial-cell seeded flow chamber and fluid reservoir[12]

Finally, the choice of pump can greatly affect the function of the system and as such must be carefully chosen. Traditional positive displacement pumps often use impellers or other mechanical systems that come in direct contact with the fluid and involve areas of high focal variations in shear. Conversely, peristaltic (roller), syringe, and pressure pumps allow precise control of flow with sensitivity to shear and without requiring the mechanical components to be in direct contact with the circulating fluid.

Depending on the application, pumps can be set to either continuous or pulsatile flow, with more complex systems being able to approximate very specific flow patterns by including devices such as dampening chambers in the flow loop. For any given pump, it is important to consider potential adverse effects such as hemolysis and platelet activation when operating at higher shear rates.

Flow Chamber Applications

Vascular cells have numerous flow-dependent functions that can be studied using flow chamber systems. Much of what is known about how endothelial cells behave under different flow conditions has been deduced in part through use of flow chamber systems. These systems have been used to characterize the effect of flow on processes in vascular cells including cytoskeletal arrangement, glycocalyx formation, endothelial cell permeability, and secretion of signaling molecules involved in inflammation, hemostasis, angiogenesis, and regulation of vascular tone [9, 13-16]. In addition to the study of typical flow-dependent vascular processes, flow chamber systems have been used to characterize the conditions and mechanisms responsible for abnormal vascular phenotypes such as atherosclerosis, thrombosis, neo-angiogenesis, and enhanced endothelial permeability in tumor environments.

In addition to their use in basic research, flow chamber systems also have many translation applications. Flow chambers are frequently used to assess the performance and biocompatibility of implantable devices such as artificial vascular grafts or shunts. Significant research efforts have been devoted to creation of biocompatible polymers and surface bio-engineering of these devices using approaches such as pre-seeding with patient-derived endothelial progenitor cells and surface conjugation of extracellular matrix components or anti-thrombotic agents such as heparin [17]. Drug-eluting implants such as stents are commonly used to prevent in-stent thrombosis that may arise from neo-intimal hyperplasia or thrombosis [18]. Flow chamber systems, in addition to ex-vivo systems discussed later in this chapter, are a valuable tool in characterizing the flow-dependent performance of vascular implants under different conditions.

A more recent application of flow chamber technology has been the development of microfluidic systems such as lab-on-a-chip devices for point-of-care testing. These devices provide rapid, on-site biomarker quantification and require only small sample volumes due to their high surface area to volume ratio[19]. Microfluidic diagnostic devices consist of small channels bearing antibodies or ligands targeted to a specific circulating biomarker. After injection of a fluid sample, these devices are placed in a machine containing pumps and measurement equipment and designed for facile and mostly automated analysis.

Flow Chambers in Contrast-Enhanced Ultrasound Molecular Imaging

While flow chamber systems have many other applications, one specific example especially relevant to this thesis is development of novel contrast agents for ultrasound molecular imaging. Contrast-enhanced ultrasound molecular imaging probes, which are discussed in further detail in later chapters, are composed of gas-filled lipid-, protein-, or polymer-shelled microbubbles (MBs) typically bearing a targeting moiety on the surface, though some agents take advantage of non-specific binding of the shell components for targeting. One advantage of this approach is the ease of designing novel probes, as this process can be as simple as attaching a new targeting ligand or antibody intended for a specific target. However, in-vivo testing of novel probes is resource and time intensive, and it can be difficult to measure off-target binding. Instead, flow chamber systems are often used for initial testing.

An example of this from a study described in Chapter 5 is the development of a platelet-targeted MB for use in measuring platelet-endothelial interactions in non-human primates. Two potential candidate targeting ligands were selected, MBs bearing these ligands were produced along with a non-targeted control MB, and each MB product was differentially fluorescently labelled. Platelets derived from primate blood and fluorescently labelled were seeded onto a parallel plate flow chamber and a mixture containing the different MB probes was introduced via syringe pump. Microscopic imaging was then used to quantify MB adhesion to platelets in order to demonstrate successful targeting under different physiologic flow conditions and determine which targeting ligand was more effective. While this flow chamber study was useful in initial

testing, one major limitation of this approach was that it did not provide a measure of off-target binding to the endothelial surface. This would however be possible in an ex-vivo flow chamber system constructed from an excised arterial segment.

Histology

Many critical processes that occur in the endothelium or associated tissue are impractical or impossible to measure in-vivo. However, once a research animal is sacrificed or a patient expires, many of these processes can then be measured in manners that often require tissue processing not suitable for live subjects. Histology is defined simply as the study of microscopic anatomy, but when used in biomedical research often refers to the sectioning, staining, and imaging of tissue for the purposes of visualizing and/or quantifying cellular and molecular processes. In studying the endothelium, it is important to preserve the state of the tissue immediately upon expiration of the subject. As such, perfusion-fixation can be performed by flushing paraformaldehyde through the left ventricular apex in order to prevent post-mortem reactions that obscure the native state of the tissue [20]. Formaldehyde reagents preserve tissue by cross-linking peptides so they are anchored in place and cannot undergo additional reactions. Other methods of preservation involve freezing in a solution of optimal cutting temperature (OCT) compound, a water-based resin mixture that allows for clean frozen sectioning using a microtome-cryostat, which preserves tissue during processing [21].

Once a tissue is fixed and preserved, it can be stained in order to highlight individual components. Staining can be performed with chemical reagents or labelled antibodies (immunohistochemistry) and depending on the technique can label cells, individual proteins, or other tissue components. In any given setting, research or clinical, stain selection depends on the cellular, molecular, or metabolic process that needs to be measured, as well as technical and practical constraints. Immunohistochemistry offers high specificity and is more often used in research due to length staining protocols and the need for fluorescent imaging, while simple chemical stains such as hematoxylin and eosin (H&E) are commonly used in clinical pathology due their

simplicity, visibility under white light, and ability to clearly label different cell populations [20, 22, 23].

Immunohistochemistry is a quantitative technique involving the use of a targeted antibody that can be visualized on microscopy in order to provide a measure of a molecule of interest. Antibodies are labelled fluorescently or using enzymes such as horseradish peroxidase that activate a soluble fluorescent compound. Detection can depend on either labelling of the targeting (primary) antibody or a secondary antibody. Primary antibody labelling is simpler and involves fewer steps, while use of a secondary labelling antibody provides signal amplification, especially when using enzymatic fluorescent detection. Parallel staining of multiple targets is made possible by using fluorophores with distinct excitation and emission spectra, however this has a practical limitation of 3-4 fluorophores. Recently, more complex multiplex staining protocols involving sequential staining of several targets has allowed for the acquisition of large amounts of data from a single tissue slide and can also be combined with image cytometry algorithms that separate cell populations with distinct molecular signatures in a manner similar to flow cytometry [23, 24].

Many imaging techniques can be coupled with immunohistochemistry for specific applications, such as Förster resonance energy transfer (FRET), which provides a measure of colocalization between two targets [25]. Confocal microscopy is used in immunohistochemistry to improve resolution and acquire images at a tightly controlled depth of focus. Super-resolution microscopy techniques such as photo-activated localization microscopy (PALM) and stochastic optical reconstruction microscopy (STORM) allow for detection beyond the diffraction limit [26]. Although immunohistochemistry can provide a measure of intracellular molecular expression through cell permeabilization steps, this technique is more well suited to detection of surface markers. Techniques such as enzyme-linked immunosorbent assay (ELISA) and western blotting are far more common approaches for quantification of intracellular proteins, peptides, and hormones [27].

In endothelial biology, histology is often utilized to quantify pro-inflammatory endothelial activation, angiogenesis, platelet-endothelial interactions and vWF

dysregulation, and atherogenesis, among other targets. Specific examples of applied immunohistochemistry in endothelial imaging are detailed in **Chapters 6-8**

Blood, Plasma, and Serum Analysis

One of the primary mechanisms by which the heart and the vascular endothelium interact is through exposure to soluble blood factors. As such, biochemical analysis of blood, plasma, or serum samples are widely used in clinical diagnostics and in research, and provide critical information on the context in which the heart and vasculature are operating. Frequently measured soluble blood factors include metal ions, proteins and enzymes, metabolic byproducts, small molecules such as glucose and steroid-based compounds, macromolecules such as lipoproteins, and microparticles or extracellular vesicles [28].

Blood samples must be preserved after collection in order to ensure stability of the molecule of interest and compatibility with corresponding testing reagents [29]. For this reason there are many different methods for processing blood between collection and measurement that vary in the anticoagulant being used and the form in which the sample is stored (whole blood, plasma, or serum). Common anti-coagulants for blood sample collection sodium citrate, heparin, EDTA and SPS. Sodium citrate is especially useful in the study of platelet activity as it binds prevents further platelet activation through binding of calcium, but unlike EDTA, which also works through calcium binding, sodium citrate chelation is reversible [29, 30]. In addition to anti-coagulants, stop solutions are often added following collection to specifically prevent either further release of the molecule or breakdown of short-lived molecules. Depending on the molecule being measured, there are several common approaches for quantifying concentration within the blood. These range from simple techniques such as direct measurement of metal ions with ion-sensitive electrodes to immunological assays such as ELISA and flow cytometry, the latter of which may be used to quantify microparticles or extracellular vesicles [31, 32].

Blood sample analysis includes assays that report both on quantity of a substance as well as activity and function. For example, direct measurement of blood levels and degree of multimerization of VWF can be used to demonstrate VWF

dysregulation but do not reveal the cause. ADAMTS13 activity assays, which measure VWF cleavage in controlled conditions, can provide additional information on the cause of dysfunction [33]. A more common example of a functional blood assay is measurement of coagulation and thrombosis. Clinicians and researchers often use assays such as prothrombin time (PT), activated partial thromboplastin time (aPTT), and thromboelastographic to determine the extent and etiology of impaired or overactive coagulation [34].

Ex-Vivo Approaches

Arterial Ring Assays

A critical function of the endothelium is to regulate blood flow to a vascular territory based on metabolic need, driving vasodilation in tissues requiring increased blood flow and diverting blood flow from tissues that are not in need. This function is dependent on endothelial cell health, as the pathways involved in blood flow regulation can be perturbed under pathologic conditions. In disease settings such as insulin resistance and atherosclerosis, endothelial dysfunction is often present, limiting vascular reactivity. However, pathologic reductions in maximal vasodilation can have different causes given the complexity of the pathways involved. Arterial ring tension assays provide a means of exploring the molecular basis for endothelial dysfunction as well as assessing the efficacy of experimental therapies to improve blood flow.

Once excised, an arterial segment must be kept under physiologic circumstances to maintain sufficient native function [35]. Typically, this is accomplished by submerging arterial rings in an organ bath containing a buffer solution such as Krebs containing various electrolytes and a bicarbonate buffer at physiologic pH. Organ baths allow for the flow of oxygen and carbon dioxide through the solution to maintain proper tissue oxygenation and pH. In the organ bath, arterial rings are mounted onto a force transducer and pulled to a passive tension. In order to measure how certain factors affect vasodilation, norepinephrine is used to achieve sub-maximal pre-constriction and followed by acetylcholine-induced relaxation under different conditions. Maximal constriction is determined through measurement of tension after the addition of KCl, a

potent vasoconstrictor [36]. The degree of vasodilation increases with the concentration of acetylcholine. However, in the setting of endothelial dysfunction, that curve will shift as higher levels of acetylcholine are needed to achieve the same degree of relaxation. Addition of various inhibitory or activating reagents can be used to measure changes in vascular tone due to specific steps in the relaxation pathway.

This technique was applied to the study of endothelial dysfunction in chronic hyperlipidemia to test the hypothesis that lipid apheresis, which removes many lipoproteins and lipid particles from the plasma, can improve blood flow [37]. In this experiment, a *ex vivo* arterial ring tension assay as described above was used to assess vascular reactivity to acetylcholine in the presence of plasma obtained before or after apheresis. Segments of ovine coronary artery and a first order branch of the femoral artery were obtained, sectioned into 3 mm rings, and mounted on a force transducer (Model 420, Newport Corp, Fountain Valley, CA) interfaced with a polygraph (model 7D, Grass Instruments, Quincy, MA) and placed in an organ bath (Harvard Apparatus, Holliston, MA) at 37° C aerated with 95% O₂ and 5% CO₂. Experiments were performed with rings immersed in either: (a) Krebs buffer containing (in mM) NaCl (118), KCl (4.7), CaCl₂ (2.5), KH₂PO₄ (1.2,) MgSO₄ (1.2), NaHCO₃ (25), and glucose (11.1) at pH 7.4; (b) Krebs buffer containing the endothelial nitric oxide inhibitor L-N^G-Nitroarginine methyl ester (L-NAME) (100 mM); (c) pre-apheresis plasma (1:1 v:v with Krebs buffer), or (d) post-apheresis plasma (previously frozen, 1:1 v:v with Krebs buffer). Rings were pulled to a passive tension isometric force of 980 dyne then pre-constricted sub-maximally with norepinephrine (10⁻⁷ M) according to maximal tension achieved with KCl (40 mM). Relative relaxation compared to passive tension values were measured during infusion of incremental concentrations of acetylcholine (Ach) (10⁻⁹ to 10⁻⁶ M). Tension assays were also performed with sodium nitroprusside (10⁻⁹ to 10⁻⁵ M) to assess endothelium independent relaxation.

Data from four arterial rings were averaged for each condition and are shown in **Figure 3A-B**. This data supported clinical findings from patients with familial hypercholesterolemia that demonstrated an improvement of coronary but not peripheral blood flow after apheresis. These findings are likely due to differences in sensitivity to hypercholesterolemia between vascular beds, although this mechanism is not well

understood. **Figure 3C-D** shows results from an in-vitro study performed on murine endothelial cells (SVEC4-10, ATCC, Manassas, VA) grown to confluence in DMEM

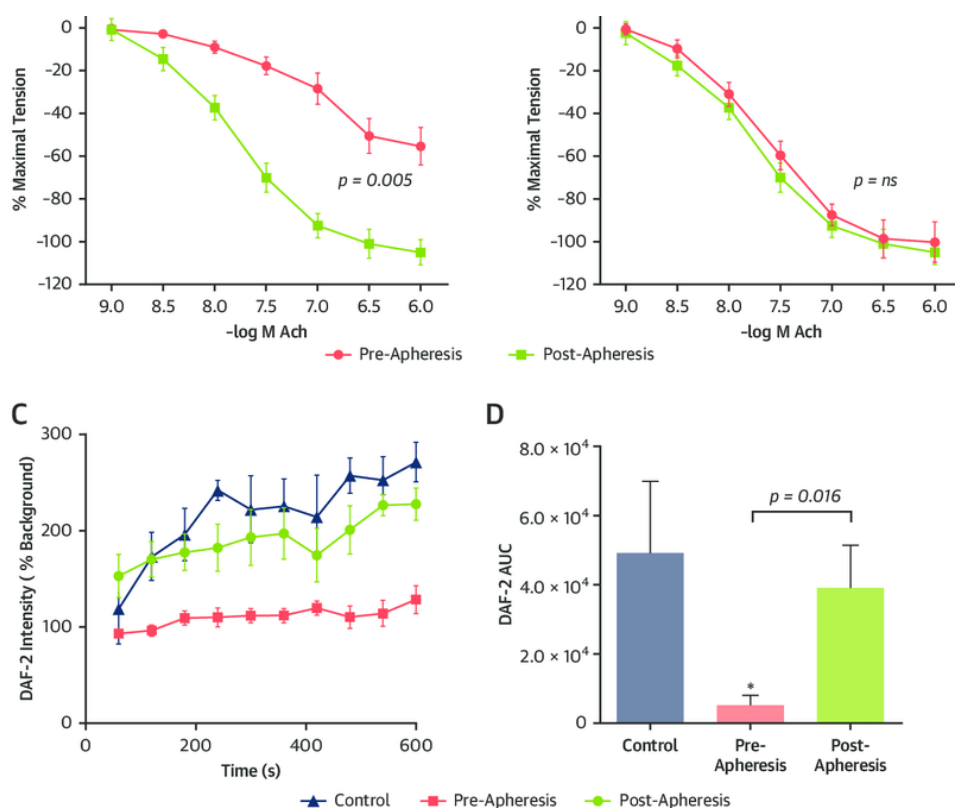


Figure 3: Tension assay dose-response curves illustrate degree of relaxation as a percentage of maximal tension (Mean ± SEM) according to acetylcholine (Ach) concentration for the **(A)** coronary and **(B)** femoral branch arteries in a water bath containing pre- and post- apheresis plasma. For coronary analysis, $p < 0.05$ versus pre-apheresis by half maximal inhibitory concentration analysis. **(C)** Mean ± SEM values for DAF-2 fluorescence over time, reflecting NO production, in cultured SVEC4-10 endothelial cells exposed to plasma from healthy volunteers or familial hypercholesterolemia patients pre- and post- apheresis. **(D)** Mean ± SEM area under the curve (AUC) for 10-min acquisition. * $p < 0.05$ versus healthy control subjects.

supplemented with 10% fetal bovine serum on fibronectin-coated culture dishes and exposed to plasma from pre- or post- apheresis hypercholesterolemic patients or from control patients for 45 minutes at 37°C. Production of NO in each case was measured using the fluorescent indicator 4,5-diaminofluorescein diacetate (DAF-2, Cayman Chemical Co.), added to the medium at a concentration of 10 μM. Fluorescence intensity was measured every minute for 10 minutes by microscopy with a silicone-intensified tube camera (SIT68, Dage-MTI, Michigan City, IN) during fluorescent illumination (460-

500 nm excitation). Results were reported as fluorescence normalized to background prior to the addition of DAF-2.

Summary

Countless other in-vitro and ex-vivo endothelial and vascular research techniques exist that are not mentioned in this chapter, but the above techniques provide an overview of common methods employed by our laboratory. Other such techniques include functional in-vitro assays such as transwell permeability assays to assess the tightness of endothelial cell junctions. Boyden chambers can be used to study vascular smooth muscle cell migration, which is a critical step in growth of atherosclerotic plaques. Other techniques not mentioned in this chapter include ex-vivo shunt loops, wherein prototype implantable vascular materials or devices can be sutured into an extracorporeal shunt loop in a live research animal to assess biocompatibility.

Despite in-vivo studies of the endothelium having the advantages of providing data in the native environment often at sequential time points in the same subject and without the need for sacrifice of the research animal, these methods have numerous practical limitations. Measurements of endothelial function are possible in-vivo, but acquisition of higher-throughput mechanistic data such as presented in Figure 3 is made easier using ex-vivo techniques such as the arterial ring tension assay. Molecular imaging techniques can provide an in-vivo measure of surface expression of specific molecules at the endothelial-blood pool interface, but these techniques are either costly, require specialized equipment, or lack the sensitivity offered by ex-vivo approaches, in addition to other limitations.

References

1. Chiu J-J, Chien S. Effects of disturbed flow on vascular endothelium: pathophysiological basis and clinical perspectives. *Physiological reviews*. 2011;91(1):327-87.
2. Kutys ML, Chen CS. Forces and mechanotransduction in 3D vascular biology. *Curr Opin Cell Biol*. 2016;42:73-9.

3. Heo K-S, Fujiwara K, Abe J-i. Shear stress and atherosclerosis. *Mol Cells*. 2014;37(6):435-40.
4. Schoeman RM, Lehmann M, Neeves KB. Flow chamber and microfluidic approaches for measuring thrombus formation in genetic bleeding disorders. *Platelets*. 2017;28(5):463-71.
5. Zwaginga JJ, Sakariassen KS, Nash G, King MR, Heemskerk JW, Frojmovic M, et al. Flow-based assays for global assessment of hemostasis. Part 2: current methods and considerations for the future. *J Thromb Haemost*. 2006;4(12):2716-7.
6. Zwaginga JJ, Nash G, King MR, Heemskerk JWM, Frojmovic M, Hoylaerts MF, et al. Flow-based assays for global assessment of hemostasis. Part 1: biorheologic considerations. *Journal of Thrombosis and Haemostasis*. 2006;4(11):2486-7.
7. Suki B, Hu Y, Murata N, Imsirovic J, Mondoñedo JR, de Oliveira CLN, et al. A microfluidic chamber-based approach to map the shear moduli of vascular cells and other soft materials. *Scientific reports*. 2017;7(1):2305-.
8. Hagen MW, Girdhar G, Wainwright J, Hinds MT. Thrombogenicity of flow diverters in an ex vivo shunt model: effect of phosphorylcholine surface modification. *J Neurointerv Surg*. 2017;9(10):1006-11.
9. Reininger AJ, Heijnen HFG, Schumann H, Specht HM, Schramm W, Ruggeri ZM. Mechanism of platelet adhesion to von Willebrand factor and microparticle formation under high shear stress. *Blood*. 2006;107(9):3537-45.
10. Erbelinger N, Rapp F, Ktitareva S, Wendel P, Bothe AS, Dettmering T, et al. Measuring Leukocyte Adhesion to (Primary) Endothelial Cells after Photon and Charged Particle Exposure with a Dedicated Laminar Flow Chamber. *Front Immunol*. 2017;8:627.
11. Hoesli CA, Tremblay C, Juneau P-M, Boulanger MD, Beland AV, Ling SD, et al. Dynamics of Endothelial Cell Responses to Laminar Shear Stress on Surfaces Functionalized with Fibronectin-Derived Peptides. *ACS Biomaterials Science & Engineering*. 2018;4(11):3779-91.
12. Salehi-Nik N, Amoabediny G, Shokrgozar MA, Mottaghy K, Klein-Nulend J, Zandieh-Doulabi B. Surface modification of silicone tubes by functional carboxyl and amine, but not peroxide groups followed by collagen immobilization improves endothelial cell stability and functionality. *Biomedical Materials*. 2015;10(1):015024.
13. Hoffman JI, Buckberg GD. Pathophysiology of subendocardial ischaemia. *Br Med J*. 1975;1(5949):76-9.
14. Thi MM, Tarbell JM, Weinbaum S, Spray DC. The role of the glycocalyx in reorganization of the actin cytoskeleton under fluid shear stress: A "bumper-car" model. *Proceedings of the National Academy of Sciences of the United States of America*. 2004;101(47):16483-8.
15. Zheng Y, Chen J, Lopez JA. Flow-driven assembly of VWF fibres and webs in in vitro microvessels. *Nat Commun*. 2015;6:7858.
16. Harding IC, Mitra R, Mensah SA, Herman IM, Ebong EE. Pro-atherosclerotic disturbed flow disrupts caveolin-1 expression, localization, and function via glycocalyx degradation. *Journal of Translational Medicine*. 2018;16(1):364.
17. Anderson DEJ, Glynn JJ, Song HK, Hinds MT. Engineering an endothelialized vascular graft: a rational approach to study design in a non-human primate model. *PLoS one*. 2014;9(12):e115163-e.
18. Htay T, Liu MW. Drug-eluting stent: a review and update. *Vasc Health Risk Manag*. 2005;1(4):263-76.
19. Nguyen T, Zoëga Andreassen S, Wolff A, Duong Bang D. From Lab on a Chip to Point of Care Devices: The Role of Open Source Microcontrollers. *Micromachines (Basel)*. 2018;9(8):403.
20. Alturkistani HA, Tashkandi FM, Mohammedsaleh ZM. Histological Stains: A Literature Review and Case Study. *Glob J Health Sci*. 2015;8(3):72-9.

21. Kumar A, Accorsi A, Rhee Y, Girgenrath M. Do's and don'ts in the preparation of muscle cryosections for histological analysis. *J Vis Exp*. 2015(99):e52793-e.
22. Matos LLd, Trufelli DC, de Matos MGL, da Silva Pinhal MA. Immunohistochemistry as an important tool in biomarkers detection and clinical practice. *Biomark Insights*. 2010;5:9-20.
23. Magaki S, Hojat SA, Wei B, So A, Yong WH. An Introduction to the Performance of Immunohistochemistry. *Methods Mol Biol*. 2019;1897:289-98.
24. Duraiyan J, Govindarajan R, Kaliyappan K, Palanisamy M. Applications of immunohistochemistry. *J Pharm Bioallied Sci*. 2012;4(Suppl 2):S307-S9.
25. Truong K, Ikura M. The use of FRET imaging microscopy to detect protein-protein interactions and protein conformational changes in vivo. *Curr Opin Struct Biol*. 2001;11(5):573-8.
26. Sigal YM, Zhou R, Zhuang X. Visualizing and discovering cellular structures with super-resolution microscopy. *Science*. 2018;361(6405):880-7.
27. Kelly BS, Levy JG, Sikora L. The use of the enzyme-linked immunosorbent assay (ELISA) for the detection and quantification of specific antibody from cell cultures. *Immunology*. 1979;37(1):45-52.
28. Quinn JG, Tansey EA, Johnson CD, Roe SM, Montgomery LE. Blood: tests used to assess the physiological and immunological properties of blood. *Adv Physiol Educ*. 2016;40(2):165-75.
29. Tammen H. Specimen collection and handling: standardization of blood sample collection. *Methods Mol Biol*. 2008;428:35-42.
30. Bowen RA, Adcock DM. Blood collection tubes as medical devices: The potential to affect assays and proposed verification and validation processes for the clinical laboratory. *Clin Biochem*. 2016;49(18):1321-30.
31. Burnett RW, Covington AK, Fogh-Andersen N, K lpmann WR, Lewenstam A, Maas AH, et al. Use of ion-selective electrodes for blood-electrolyte analysis. Recommendations for nomenclature, definitions and conventions. International Federation of Clinical Chemistry and Laboratory Medicine (IFCC). Scientific Division Working Group on Selective Electrodes. *Clin Chem Lab Med*. 2000;38(4):363-70.
32. Welsh JA, Holloway JA, Wilkinson JS, Englyst NA. Extracellular Vesicle Flow Cytometry Analysis and Standardization. *Front Cell Dev Biol*. 2017;5:78-.
33. Fu X, Pahl MN, Wang Y, Konkle BA, Chen J, Lopez JA. A Quantitative Assay of In Vivo Cleavage of Von Willebrand Factor By ADAMTS13 Reveals Excessive Cleavage in Type 2B Von Willebrand Disease and Diminished Cleavage in Thrombotic Thrombocytopenic Purpura. *Blood*. 2016;128(22):2532-.
34. Hunter SB, Royal FS, Green LD. An approach to the evaluation of hemostasis. *J Natl Med Assoc*. 1977;69(9):643-4.
35. Masson V V , Devy L, Grignet-Debrus C, Bernt S, Bajou K, Blacher S, et al. Mouse Aortic Ring Assay: A New Approach of the Molecular Genetics of Angiogenesis. *Biol Proced Online*. 2002;4:24-31.
36. Ko EA, Song MY, Donthamsetty R, Makino A, Yuan JXJ. Tension Measurement in Isolated Rat and Mouse Pulmonary Artery. *Drug Discov Today Dis Models*. 2010;7(3-4):123-30.
37. Wu MD, Moccetti F, Brown E, Davidson BP, Atkinson T, Belcik JT, et al. Lipoprotein Apheresis Acutely Reverses Coronary Microvascular Dysfunction in Patients With Severe Hypercholesterolemia. *JACC Cardiovasc Imaging*. 2019;12(8 Pt 1):1430-40.

Techniques for Live Imaging of Blood Flow

Introduction

This chapter covers various imaging modalities and techniques that allow for in-vivo characterization of blood flow, local perfusion, and cellular interactions at the endothelial surface. These techniques cover everything from 2D echocardiography, which measure global cardiac function and output, to perfusion imaging and intravital microscopy which are used to measure blood flow in specific tissues or even vascular segments. With the exception of intravital microscopy, which provides single vessel resolution, the techniques discussed in this chapter are non-invasive in nature and can be safely used clinically and in the lab to assess regional blood flow.

Ultrasound is the workhorse of non-invasive cardiovascular imaging and is capable of characterizing blood flow at scales ranging from ventricular ejection to individual tissue beds. In the heart, in addition to its ability to quantify global and regional myocardial function and probe as valve function and health, ultrasound imaging can provide a measure of cardiac output. In smaller vessels where traditional ultrasound may be inadequate for measuring blood flow, ultrasound perfusion imaging allows for quantitative measurements of blood flow using microbubble contrast agents. In addition to a basic review of ultrasound cardiac imaging techniques, this chapter will explore the physical basis for microbubble imaging and how it is applied for perfusion imaging. Laser doppler and associated optical flowmetry methods will also be discussed as a perfusion imaging technique.

For visualizing blood flow in individual small vessels, intravital microscopy presents an invasive means that can distinguish between red blood cells, leukocytes,

and platelets, and can produce video of events occurring at the endothelial surface, such as endothelial leukocyte rolling and platelet capture as well as platelet-leukocyte interactions.

Contrast Enhanced Ultrasound Perfusion Imaging

The primary role of the cardiovascular system is to deliver oxygen and nutrients to tissue, a task entirely dependent of maintenance of proper blood flow, both in terms of cardiac output and perfusion of individual vascular beds. As such, cardiac output and local perfusion serve as ideal measures of overall cardiovascular function.

Measurement of cardiac output is relatively simple as the volume of blood flow is equal to the change in volume of the left ventricle between end diastole and end systole, and the rate of flow is then easily deduced from the heartrate [1]. However, obtaining a reliable measure of local perfusion in any vascular territory presents more complex technical challenges than basic volumetric measurements. In measuring coronary perfusion, over 90% of myocardial blood volume is contained within the capillaries, so any technique must be capable of measuring microvascular blood flow while ignoring any signal arising from cardiac output [2]. Tracers such as radiolabeled or fluorescent microspheres can be used to measure perfusion in preclinical settings, and newer techniques such as CT myocardial perfusion imaging are being developed, but this section will focus on ultrasound as a platform for perfusion imaging [3, 4].

CEU imaging relies on receiving signal generated by encapsulated gas MBs when exposed to ultrasound [5, 6]. In the pressure fluctuations of an ultrasound field, MBs undergo volumetric oscillation. Steady expansion and contraction (stable cavitation) occurs at low pressure which can be non-linear with regard to the relationship between pressure and volume [7, 8]. Destruction of microbubbles can occur from exaggerated oscillation at high pressures, known as inertial cavitation [9]. Both inertial cavitation and non-linear stable cavitation result in emission of broad band ultrasound signals and ultrasound energy peaks at harmonic frequencies, thereby producing a unique acoustic signature that can be detected and isolated from background tissue signal [10-12]. Conventional MB agents used in humans are between 1 and 5 μm in diameter, have a core composed of a high-molecular weight inert gas

such as perfluorocarbons or sulfur hexafluoride, and have a shell composed of lipids or proteins such as albumin. A wide variety of other acoustically active experimental ultrasound contrast agents has been explored, but are out of the scope of this review [13]. MB agents are smaller than erythrocytes and have a microvascular rheology similar to that of erythrocytes [14, 15]. Accordingly, they normally pass unimpeded through capillaries, which is important for both safety considerations and their use as flow tracers. Lipid MBs also often contain surface “coats” composed of biocompatible polymers such as polyethylene glycol (PEG), which prevent their interaction with cells and plasma proteins [16-18]. In clinical cardiovascular medicine, CEU is most often used to opacify the left ventricular (LV) cavity on echocardiography in order to better evaluate global or regional function, LV dimensions, and the presence of intracavitary masses such as thrombi [19].

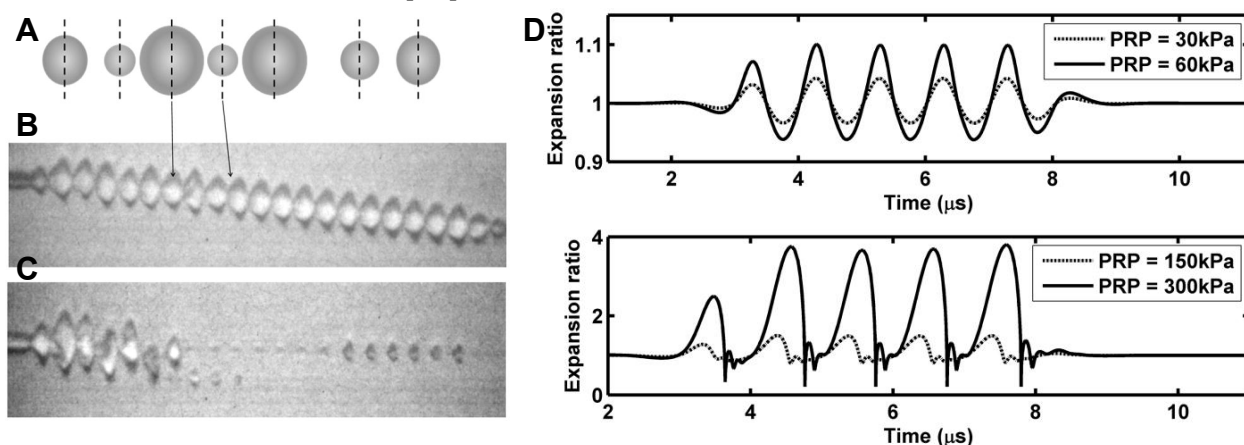


Figure 1: Microbubble oscillation dynamics under ultrasound excitation (A) schematic of pressure-mediated MB volumetric oscillations with corresponding high-speed images (B) of a microbubble oscillating over time (represented by the horizontal axis) under 2.25MHz ultrasound pulses at a PRP of 100kPa. (C) Microbubble dynamics at higher (300kPa) PRP demonstrating inertial cavitation and fragmentation. (C-D) predicted oscillation of expansion ratio over time of a 2µm microbubble in response to a 1-MHz 5-cycle pulse using equations and parameters described in Zhao et al., 2004. (C) shows stable cavitation at lower PRPs with harmonic oscillation near the frequency of the transmitted pulse while (D) demonstrates nonlinear oscillation at higher PRPs, resulting in greater increase to expansion ratio relative to the increase in pressure. [20, 21]

After intravenous injection, MBs remain in the vascular space, thereby opacifying the blood pool on ultrasound imaging. The response of a microbubble to excitation by ultrasound energy depends on several factors, most importantly frequency and peak negative acoustic pressure (PNAP). The unit mechanical index, defined as the PNAP

divided by the square root of the frequency, is a useful measure of the mechanical environment to which MBs are exposed under ultrasound excitation, and provides an indication of the MB response. For example, at a low mechanical index (less than 0.3 depending on MB design, tissue, and ultrasound characteristics), MBs are not detectable on ultrasound [22]. At what is known as the stable cavitation threshold, MBs begin to oscillate in volume along with pressure variation, leading to signal generation at fundamental and harmonic frequencies. The expansion ratio, a measure of bubble diameter change, increases mostly proportional to PNAP in the linear range. At higher mechanical indices these oscillations and the accompanying generated signal become nonlinear along with the relationship between expansion ratio and PNAP, leading to fragmentation and, at high enough acoustic intensity, destruction of MBs [9]. **Figure 1** illustrates these oscillations at different peak rarefaction pressures (PRP), which is equivalent to PNAP.

CEU perfusion imaging takes advantage of MB destruction MBs at high MI ultrasound pulses by measuring MB replenishment as a marker of blood flow in a given segment of tissue [23]. Figure 2A illustrates MB replenishment across the elevation (thickness) of the beam after a destructive ultrasound pulse at $t=0$. MBs travelling at velocity v will travel distance $d=vt$, so the concentration of MBs within the elevation as a function of time is proportional to vt/E as well as to video intensity [24]. Since a high-MI ultrasound pulse simultaneously destroys MBs in the field of view as well as provides ultrasound signal, repeated high-MI pulses at a given pulsing interval PI will measure the degree of MB replenishment within that interval. As the pulsing interval increases at a constant v , the distance travelled and by extension MB concentration will increase. At a high enough PI, full replenishment and video intensity as a function of PI will plateau. Performing repeated destruction-replenishment pulsing at several different PIs yields a curve of MB replenishment over time.

The simplified model shown in Figure 2A would yield a linear increase in video intensity relative to pulsing interval, which becomes a sharp plateau once full replenishment occurs (Figure 2B). However, observed destruction-replenishment within tissue follows a curvilinear trend (Figure 2C). The video intensity at the plateau is proportional to tissue blood volume (A -value) and determined by comparison to video

intensity in the LV cavity in which the volume of blood is known. The curvilinear function that describes tissue MB replenishment is $f(t)=A(1-e^{-\beta t})$, where $f(t)$ is the video intensity at a pulsing interval of t , and β , the rate constant, is equivalent to mean tissue blood velocity. Tissue blood flow (L/min) can then be calculated as the product of blood flow velocity and blood volume ($A \times \beta$).

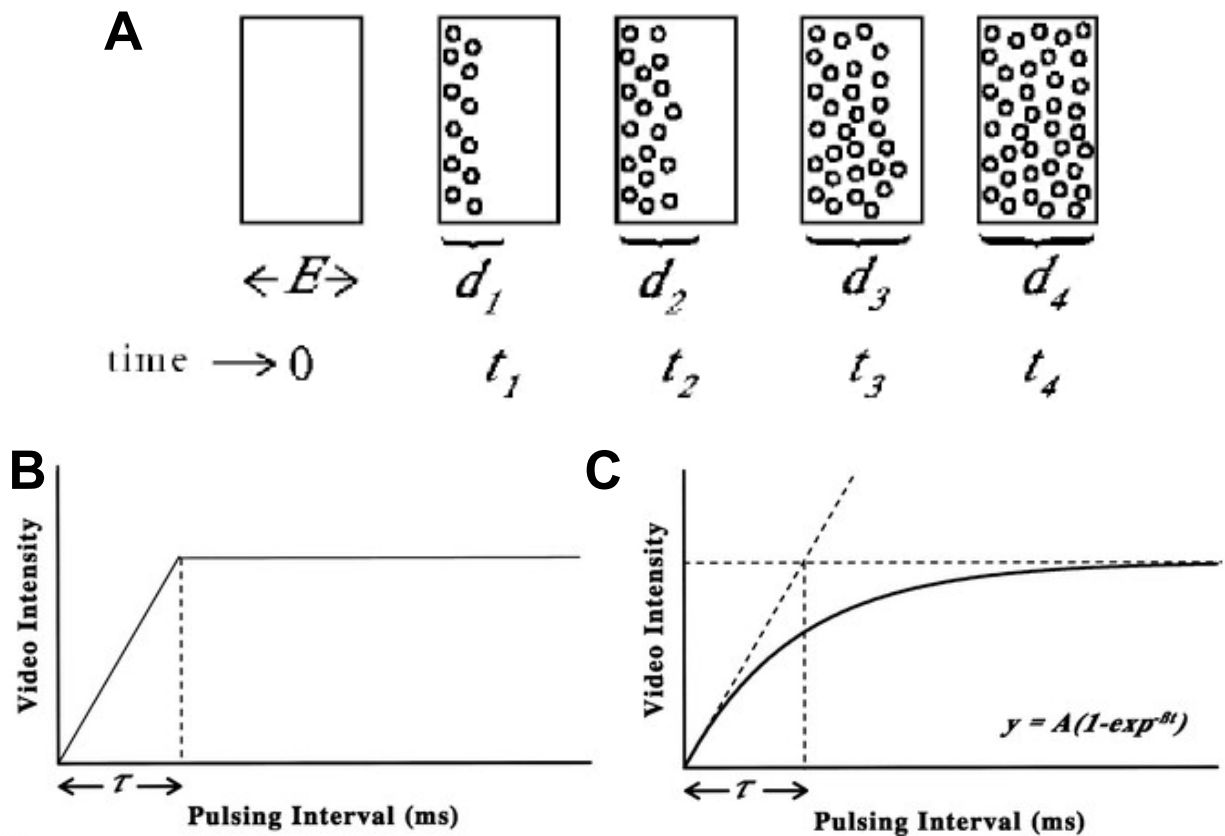


Figure 2: (A) Illustration of microbubble replenishment across the elevation (thickness) of an ultrasound beam, denoted as E . (B) Predicted video intensity, proportional to MB concentration, versus pulsing interval, assuming constant MB velocity during replenishment. (C) Observed video intensity versus pulsing interval, demonstrating curvilinear MB replenishment. [24]

While CEU was initially developed with a high MI pulsing scheme, it is also possible to image MB replenishment at low MI in real time after an initial high MI destructive pulse [25]. This approach is significantly easier for the operator, as in high MI CEU the operator must hold the probe steadily for prolonged periods of time as the ultrasound system cycles through multiple pulse cycles at each pulsing interval. With low-MI images, imaging occurs in real time and requires only seconds to acquire.

Additionally, high MI imaging may affect results through ultrasound bioeffects, which is explained later in this section.

There are many reasons to use CEU both clinically and in research settings. In the most common application of CEU perfusion, myocardial contrast echocardiography (MCE), images of an entire LV cross-section are captured and can then be segmented to obtain myocardial blood flow measurements in specific regions of the LV (e.g. apex, anterior wall) [26]. This approach has tremendous utility in both quantifying the extent of ischemia as well as locating perfusion defects, the latter of which does not necessarily require post-processing as severe perfusion defects are often readily apparent on an MCE image. While resting perfusion defects can be visible in severe ischemia, MCE is often combined with stress protocols to reveal regions of hypoperfusion not otherwise visible at rest. An example of MCE and an accompanying coronary angiogram are seen in **Figure 3**.

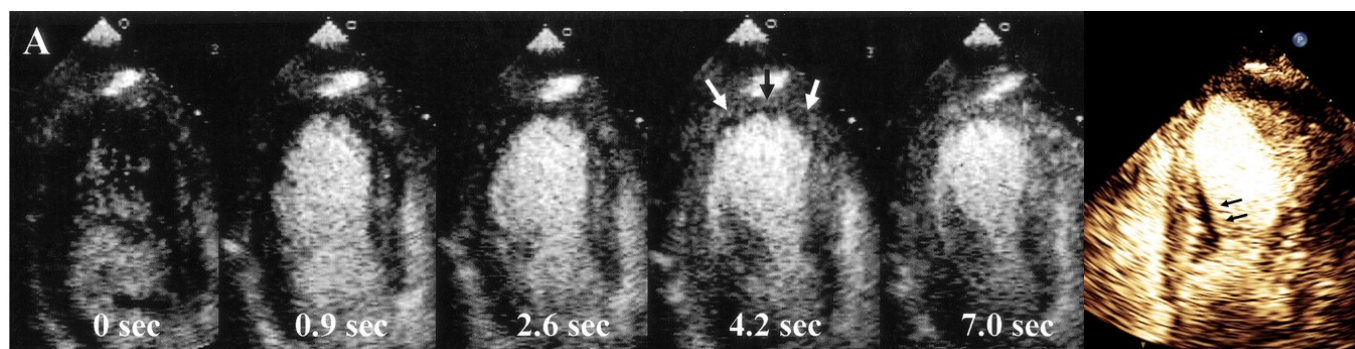


Figure 3: Apical 3-chamber view during a constant infusion of microbubbles at progressively higher pulsing intervals (A) in a patient with collateralized left anterior descending artery (B). Slow collateral-derived perfusion is seen in the apex despite an occluded IRA (apex). [23]

In coronary artery disease, MCE is an excellent tool for assessing microvascular disease, which can otherwise be difficult to visualize and diagnose as compared with large vessel stenosis [27, 28]. In research settings, MCE is used to study changes to coronary blood flow in response to pathologic processes or to novel therapies. MCE has been used in non-human primate, canine, and ovine disease models, among others, but is not practical in murine disease models. Murine resting heart rates often exceed 500 BPM and contrast imaging systems do not have sufficient framerates, while high-frequency ultrasound systems used for resolving the smaller murine organs lack sufficient ability to destroy contrast agents.

Aside from the heart, CEU can be applied to many other tissues, such as liver, skeletal muscle, and placenta, among others. Skeletal muscle CEU has been critical in discovering and defining a branch of therapeutic ultrasound that takes advantage of ultrasound bioeffects that result in increased blood flow [29]. In the diagnostic range of ultrasound MI, bioeffects such as tissue heating and changes to blood flow are mostly negligible. However, it has been shown that at high MI, ultrasound energy increases skeletal muscle perfusion, which could provide value as a peripheral arterial disease therapy, as well as perfusion in other organs, though this is not as well studied. Perfusion related ultrasound bioeffects, which are greatly potentiated by MBs, act through shear-mediated purinergic signaling and can lead to up to 10-fold increases in skeletal muscle blood flow. Imaging of murine hindlimbs with CEU was used both initially to demonstrate this effect as well as in mechanistic studies, which led to discovery of the complex pathway involved.

CEU perfusion imaging and more specifically, MCE, is a versatile, affordable, and safe technique that provides quantitative information on regional flow and can be performed at the patient bedside. Despite extensive validation, clinical adoption of CEU perfusion imaging and MCE has been slow, due to factors such as a steep learning curve for performing and troubleshooting CEU perfusion imaging, slow development of contrast-specific ultrasound packages and perfusion analysis software specifically for CEU, as well as other practical and technical limitations. Meanwhile, CEU perfusion imaging has been applied in a limited but successful manner in pre-clinical research, both for myocardial blood flow and perfusion imaging of other organs.

Intravital Microscopy

Intravital microscopy encompasses several research techniques for optical imaging of live blood flow. These techniques can be invasive, such as those that consists of surgically exposing a segment of optically translucent vascularized tissue and mounting it on a microscopic stage for viewing. [30] Intravital microscopy can also be performed non-invasively using techniques such as two-photon microscopy [31]. Using intravital microscopy, it is possible to obtain images of individual erythrocytes, leukocytes, and, and even platelets as blood flows by. This technique is a powerful

basic and translational tool for quantifying the effect of pharmacologic or other intervention on endothelial surface interactions. For example, intravital microscopy has been used to demonstrate a decrease in leukocyte capture and platelet-endothelial interactions in response to therapy targeted towards prevention of microvascular dysfunction.

This segment details methods and applications for intravital microscopy, specifically of the murine cremaster muscle. The murine cremaster muscle is an approximately 100 μ m thick, optically translucent, well vascularized segment of tissue surrounding the testes, and can be separated from surrounding anatomy without causing significant trauma, thus presenting an ideal target for live imaging. There are additional methods besides surgical cremaster exposure, including two-photon microscopy of the jugular vein, but this segment will focus on intravital microscopy performed on surgically excised murine cremaster muscles

To prepare the cremaster tissue for imaging, the animal is first anesthetized. While inhaled anesthesia such as isoflurane is generally easier to maintain when compared to intraperitoneally delivered anesthetic mixtures such as ketamine/xylazine, nose cones can create added difficulty in preparing and moving animals. Once the animal is anesthetized, the cremaster muscle is surgically exteriorized, spread over a specialized microscopy platform, and pinned around the edges. To maintain proper tissue function, a drip is introduced to provide a bicarbonate salt superfusion buffer at physiologic pH and temperature and with oxygen introduced via diffuser. Animals can be cannulated, often at the jugular vein, in order to introduce tracers or therapeutic compounds during imaging. After surgical preparation, the microscopy platform bearing the animal can be transferred to the microscope stage for imaging. A typical cremaster intravital microscopy preparation is illustrated in **Figure 4A**. An example of a bright field intravital image showing erythrocyte flow is seen in **Figure 4B**.

There are several ways to quantify changes to leukocyte-endothelial interactions using intravital microscopy. In order to view leukocytes, a fluorescent labelling compound such as Rhodamine-6-G can be introduced via venous catheter. Leukocyte flux fraction, defined as the ratio of rolling leukocytes to total leukocyte flux through an

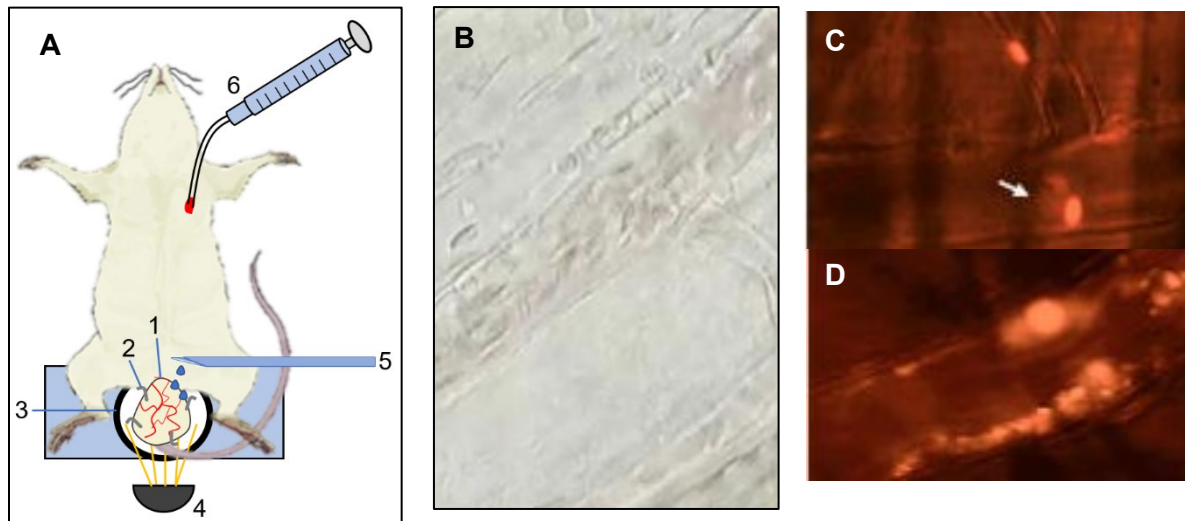


Figure 4: (A) Schematic of a murine cremaster intravital microscopy preparation: 1- exteriorized cremaster muscle; 2- pins; 3- intravital platform; 4- illumination source; 5- superfusion buffer drip; 6- jugular venous catheter (B) Bright field intravital image of murine cremaster showing erythrocyte flow through an arteriole (C-D) Fluorescent images of a murine cremaster muscle with platelets and leukocytes labelled with Rhodamine-6-G. A platelet-leukocyte complex is visible in (C) and platelet-VWF strings are visible in (D).

arterial segment, is a robust measure of endothelial leukocyte recruitment that depends on a number of factors including endothelial activation, leukocyte activation, and shear rate. However, it requires additional measurements of bulk blood flow rate and complete blood count to determine the proportion of circulating leukocytes within the blood. A simpler approach is to measure the number of rolling, adherent, and extravasated leukocytes, as well as leukocyte rolling velocity, which is inversely correlated to endothelial ECAM expression [32]. These velocity measurements can be performed in ImageJ using the particle tracking tool. Figure 4C-D shows examples of fluorescently labelled leukocytes in a murine cremaster arteriole.

Given the simultaneous activation within endothelial cells of platelet capture mechanisms in response to inflammatory activation, it is also important to measure platelet-endothelial and platelet-leukocyte interactions when investigating the effect of a pro-inflammatory pathologic process on the endothelial-blood pool interface. Platelets are also labelled by Rhodamine-6-G, and can be distinguished from leukocytes based on their smaller size and irregular shape. Given the string-like nature of ultra-long VWF multimers, platelets often appear as strings, with which leukocytes can be seen

transiently interacting or adhering through platelet P-selecting and leukocyte PSGL-1. String formation can be visualized in real time, as well as their occasional detachment and embolization. Repeat observations have shown that after embolization of a platelet string or aggregate, platelet-endothelial interactions seem to preferentially occur at the spot of initial attachment, which could potentially be due to further activation of the endothelium by nearby platelets, although this has not been conclusively shown.

Intravital microscopy provides unique value in that it produces live images of intravascular cellular interactions under flow, and has led to multiple important observations regarding platelet-endothelial interactions, some of which are detailed in Chapters 5 and 6.

Laser Doppler Flowmetry

The doppler effect has long been among the most valuable principles in the world of imaging. When the goal is to describe movement within a system, doppler shifts can be used to provide quantitative dynamic data. The physical principle underlying the doppler effect is the changing wavelength of reflected light after interaction with a moving object. An object approaching the observer and lo will result in higher received frequencies and lower wavelengths, while an object moving away produces the opposite effect. This principle is not limited to light waves but is true for sound and other waves as well, and thus can be applied to ultrasound as well as optical imaging.

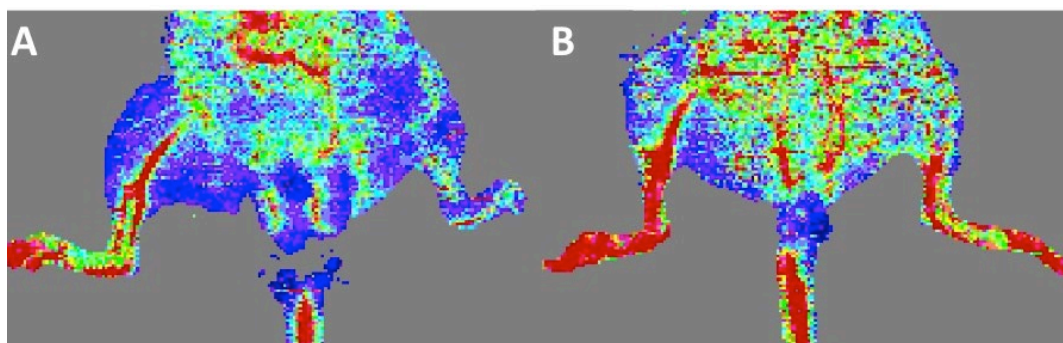


Figure 5: Laser doppler flowmetry images of mouse hindlimb blood flow after acute ischemia in (A) untreated animals and (B) animals treated with low-energy shockwave therapy. Treatment was shown to increase angiogenesis, which resulted in improved blood flow.

In the case of *in vivo* blood flow imaging, doppler shifts can be used to quantify microvascular blood flow velocity across multiple types of tissue. A laser doppler system captures this data through laser illumination of a tissue sample followed by detection of backscattered light and analysis of frequency distribution, which indicates the velocity of individual blood cells [33]. One major limitation of laser doppler is penetration depth. Depending on the tissue and the system capabilities, penetration past the skin layers may be challenging, although it is possible to invasively obtain organ blood flow through a laser doppler catheter. Laser doppler flowmetry also does not provide quantitative information of total blood flow, only the velocity distribution. This can however be a useful measure of relative changes in flow when this distribution changes and can also be used to detect regions of perfusion abnormalities by producing images based on local frequencies, as seen in Figure 5, rather than simply overall frequency distribution. Despite its drawbacks, laser doppler flowmetry is a safe and simple technique, and developments such as introduction of machine learning pattern recognition, similar to speckle tracking in ultrasound imaging, will continue to improve its utility.

Summary

Live imaging of blood flow provides information on what nutrients, factors, and cellular processes the endothelium is exposed to. Direct measurement of blood flow through perfusion imaging can be used to identify regions of hypoperfusion and hypoxia perfusion, but imaging of organ perfusion typically requires MCE or nuclear perfusion imaging. Imaging of cellular or molecular events in a live vessel can be performed using different types of intravital microscopy, including two-photon microscopy and invasive cremaster imaging. The latter is used extensively to detect interactions between the endothelium and fluorescently labelled platelets and leukocytes under *in vivo* conditions.

References

1. Hillis GS, Bloomfield P. Basic transthoracic echocardiography. *BMJ (Clinical research ed)*. 2005;330(7505):1432-6.
2. Le DE, Jayaweera AR, Wei K, Coggins MP, Lindner JR, Kaul S. Changes in myocardial blood volume over a wide range of coronary driving pressures: role of capillaries beyond the autoregulatory range. *Heart*. 2004;90(10):1199-205.

3. Reinhardt CP, Dalhberg S, Tries MA, Marcel R, Leppo JA. Stable labeled microspheres to measure perfusion: validation of a neutron activation assay technique. *Am J Physiol Heart Circ Physiol*. 2001;280(1):H108-16.
4. Slomka PJ, Miller RJH, Hu LH, Germano G, Berman DS. Solid-State Detector SPECT Myocardial Perfusion Imaging. *J Nucl Med*. 2019;60(9):1194-204.
5. Sirsi S, Borden M. Microbubble Compositions, Properties and Biomedical Applications. *Bubble Sci Eng Technol*. 2009;1(1-2):3-17.
6. De Jong N. Physics of Microbubble Scattering. In: N.C. N, R. S, B.B. G, editors. *Advances in Echo Imaging Using Contrast Enhancement*: Springer, Dordrecht; 1997.
7. Jong ND, Frinking P, Cate FT, Wouw PVD, editors. Characteristics of contrast agents and 2D imaging. 1996 IEEE Ultrasonics Symposium Proceedings; 1996 3-6 Nov. 1996.
8. Overvelde M, Garbin V, Sijl J, Dollet B, de Jong N, Lohse D, et al. Nonlinear shell behavior of phospholipid-coated microbubbles. *Ultrasound Med Biol*. 2010;36(12):2080-92.
9. Shi WT, Forsberg F, Tornes A, Ostensen J, Goldberg BB. Destruction of contrast microbubbles and the association with inertial cavitation. *Ultrasound Med Biol*. 2000;26(6):1009-19.
10. Burns PN. Harmonic imaging with ultrasound contrast agents. *Clin Radiol*. 1996;51 Suppl 1:50-5.
11. Burns PN PJ, Simpson DH, Brezina A, Kolin A, Chin CT et al., editors. Harmonic power mode Doppler using microbubble contrast agents: an improved method for small vessel flow imaging. *Proceedings of IEEE Ultrasonics Symposium*. 1994;31.
12. Simpson D, Chin CT, Burns PN. Pulse inversion Doppler: a new method for detecting nonlinear echoes from microbubble contrast agents. *IEEE Transactions on Ultrasonics, Ferroelectrics and Frequency Control*. 1999;46:372-82.
13. Paefgen V, Doleschel D, Kiessling F. Evolution of contrast agents for ultrasound imaging and ultrasound-mediated drug delivery. *Front Pharmacol*. 2015;6:197-.
14. Lindner JR, Song J, Jayaweera AR, Sklenar J, Kaul S. Microvascular rheology of Definity microbubbles after intra-arterial and intravenous administration. *Journal of the American Society of Echocardiography*. 2002;15(5):396-403.
15. Ismail S, Jayaweera AR, Camarano G, Gimple LW, Powers ER, Kaul S. Relation between air-filled albumin microbubble and red blood cell rheology in the human myocardium. Influence of echocardiographic systems and chest wall attenuation. *Circulation*. 1996;94(3):445-51.
16. Du H, Chandaroy P, Hui SW. Grafted poly-(ethylene glycol) on lipid surfaces inhibits protein adsorption and cell adhesion. *Biochimica et Biophysica Acta (BBA) - Biomembranes*. 1997;1326(2):236-48.
17. Fisher NG, Christiansen JP, Klivanov A, Taylor RP, Kaul S, Lindner JR. Influence of microbubble surface charge on capillary transit and myocardial contrast enhancement. *Journal of the American College of Cardiology*. 2002;40(4):811-9.
18. Chen CC, Borden MA. Ligand Conjugation to Bimodal Poly(ethylene glycol) Brush Layers on Microbubbles. *Langmuir*. 2010;26(16):13183-94.
19. Senior R, Becher H, Monaghan M, Agati L, Zamorano J, Vanoverschelde JL, et al. Clinical practice of contrast echocardiography: recommendation by the European Association of Cardiovascular Imaging (EACVI) 2017. *European Heart Journal - Cardiovascular Imaging*. 2017;18(11):1205-af.
20. Qin S, Caskey CF, Ferrara KW. Ultrasound contrast microbubbles in imaging and therapy: physical principles and engineering. *Phys Med Biol*. 2009;54(6):R27-R57.
21. Zhao S, Borden M, Bloch SH, Kruse D, Ferrara KW, Dayton PA. Radiation-force assisted targeting facilitates ultrasonic molecular imaging. *Mol Imaging*. 2004;3(3):135-48.

22. Deng CX, Xu Q, Apfel RE, Holland CK. Inertial cavitation produced by pulsed ultrasound in controlled host media. *J Acoust Soc Am*. 1996;100(2 Pt 1):1199-208.
23. Lepper W, Belcik T, Wei K, Lindner JR, Sklenar J, Kaul S. Myocardial contrast echocardiography. *Circulation*. 2004;109(25):3132-5.
24. Wei K, Jayaweera AR, Firoozan S, Linka A, Skyba DM, Kaul S. Quantification of Myocardial Blood Flow With Ultrasound-Induced Destruction of Microbubbles Administered as a Constant Venous Infusion. *Circulation*. 1998;97:473-83.
25. Sieswerda GT, Yang L, Boo MB, Kamp O. Real-time perfusion imaging: a new echocardiographic technique for simultaneous evaluation of myocardial perfusion and contraction. *Echocardiography*. 2003;20(6):545-55.
26. Averkiou MA, Bruce MF, Powers JE, Sheeran PS, Burns PN. Imaging Methods for Ultrasound Contrast Agents. *Ultrasound in Medicine and Biology*. 2020;46(3):498-517.
27. Lindner JR. Microvascular Dysfunction and Clinical Outcomes. *Circulation Cardiovascular imaging*. 2018;11(10):e008381-e.
28. Lindner JR, Skyba DM, Goodman NC, Jayaweera AR, Kaul S. Changes in myocardial blood volume with graded coronary stenosis. *Am J Physiol*. 1997;272:H567-H75.
29. Belcik JT, Mott BH, Xie A, Zhao Y, Kim S, Lindner NJ, et al. Augmentation of limb perfusion and reversal of tissue ischemia produced by ultrasound-mediated microbubble cavitation. *Circ Cardiovasc Imaging*. 2015;8(4).
30. Rius C, Sanz MJ. Intravital Microscopy in the Cremaster Muscle Microcirculation for Endothelial Dysfunction Studies. *Methods Mol Biol*. 2015;1339:357-66.
31. Masedunskas A, Milberg O, Porat-Shliom N, Sramkova M, Wigand T, Amornphimoltham P, et al. Intravital microscopy: a practical guide on imaging intracellular structures in live animals. *Bioarchitecture*. 2012;2(5):143-57.
32. Moccetti F, Brown E, Xie A, Packwood W, Qi Y, Ruggeri Z, et al. Myocardial Infarction Produces Sustained Proinflammatory Endothelial Activation in Remote Arteries. *Journal of the American College of Cardiology*. 2018;72(9):1015.
33. Oberg PA. Laser-Doppler flowmetry. *Crit Rev Biomed Eng*. 1990;18(2):125-63.

Molecular Imaging of the Cardiovascular System

Summary

This chapter will detail multi-modality molecular imaging techniques including those based on ultrasound, radionuclide, and MR that have recently been developed for use in cardiovascular imaging. Special focus will be given to ultrasound molecular imaging, its principles, and its clinical and research applications. Detailed examples of recent research advances utilizing CEU molecular imaging can be found in chapters 5,6, and 7. In addition to providing an overview of the various molecular imaging techniques and how they can be used to study cardiovascular and endothelial physiology, the various benefits and drawbacks of each technique as compared to others will be discussed.

Molecular Imaging

Over the past decade, there has been rapid development in molecular imaging techniques that are able to non-invasively assess molecular or cellular phenotype in animal models of disease and in humans. These techniques are advantageous in that they provide both spatial and temporal information on complex disease processes at the molecular level and can be combined with traditional measurements provided by imaging on structure, function and flow. Molecular imaging techniques can be applied in research settings to study cardiovascular disease pathophysiology and test novel therapies as well as clinical settings to detect pathological processes, risk-stratify patients, and guide personalized treatment (Figure 1) [1].

Methods for molecular imaging are diverse and span all forms of medical imaging including radionuclide, optical, magnetic resonance imaging (MRI), and ultrasound [2]. The general approaches to imaging a molecular profile in situ are diverse (Table 1) and rely primarily on the detector capabilities [1, 3]. One of the most common approaches is to use contrast agents that are functionalized to reveal a targeted molecular process. Some simple examples of are the radiolabeling of antibodies or antibody fragments for radionuclide imaging of disease process [4], or taking advantage of a metabolic process that uses a particular substrate such as the positron emission tomography (PET) imaging of the consumption rate of ^{18}F fluorodeoxyglucose(FDG), which enters the glycolysis pathway and becomes trapped in cells at a rate proportional to cellular glucose uptake [5]. While some of these processes can be measured through histological or other post-mortem analysis, in vivo molecular imaging is useful in research for providing data from multiple time points in a single animal. However, given the expanding range of options in both probes and detectors, it is essential to carefully consider many of the factors that govern whether a technique is well suited to a specific clinical or research application.

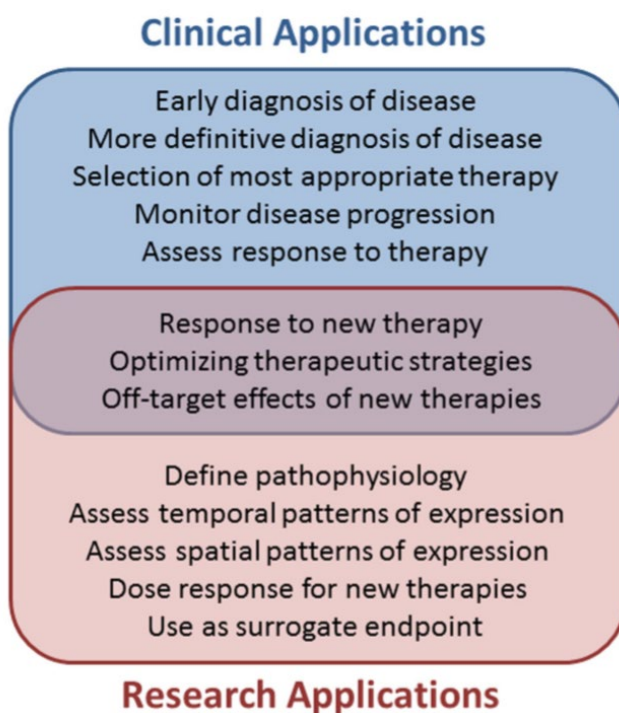


Figure 1: Schematic illustrating some of the major clinical and investigational roles of molecular imaging in medicine and science

Radionuclide Molecular Imaging

Strategy	Contrast	Modality
Tracer retention by ligand-receptor binding	Y	RN, US, CT, MR, OI
Cellular retention from metabolic machinery	Y	RN, US, MR, OI
Tracer activation by targeted enzymatic process	Y	OI
Endogenous signal characteristics	N	MR

N, No; *Y*, Yes; *CT*, computed tomography; *MR*, magnetic resonance imaging; *OI*, optical imaging; *RN*, radionuclide imaging; *US*, ultrasound

Table 1 General approaches for in vivo molecular imaging

Radionuclide(RN)-based molecular imaging is a powerful tool that makes use of probes such as antibodies, peptides, or small molecules conjugated to radioactive isotopes as well as radioactive compounds that are measured by a specialized nuclear detector such as a positron emission tomography (PET) or single photon emission computed tomography (SPECT) camera [6]. Choice of PET or SPECT mostly depends on the isotope, with PET providing a measure of positron emission and SPECT measuring gamma ray emission. Isotopes used for SPECT imaging typically have longer half lives on the order of hours to days and are relatively inexpensive, while PET isotopes tend to be shorter on the order of a few minutes to hours. Other differences include higher cost of PET equipment and tracers, which require a cyclotron to produce, but better spatial resolution compared to SPECT and incredible sensitivity on the order of pM, though both PET and SPECT have high sensitivity and low spatial resolution when compared to other modalities. Tracer retention can occur either through retention within cells following consumption or modification by metabolic processes or by direct ligand-receptor binding between the tracer and its target molecule. The latter mechanism is how RN molecular imaging is used to provide quantitative information on events at the endothelial surface [7].

While it is costly, involves ionizing radiation, and can involve long acquisition times, RN molecular imaging techniques are incredibly versatile and can provide measurements of biodistribution and pharmacokinetics or be combined with other modalities such as computer tomography (CT) or magnetic resonance (MR) to provide simultaneous high-resolution structural information. RN imaging is a widely-used clinical

tool and has a number of diagnostic and research applications, however it may be prohibitively expensive for or out of reach of many basic and translational research laboratories, especially if development of a novel probe is required. Micro-PET and SPECT equipment, when available, can be used for small animal imaging and like full-size RN equipment can be paired with CT or MR [8, 9].

Radionuclide Contrast Agents

There are two primary types of radionuclide contrast agents. Radiolabeled compounds are made via chemical synthesis that incorporates a radioactive isotope into the compound and are used to measure metabolic processes. These agents enter cells and are retained at a rate proportional to the rate at which the metabolic pathway of interest is operating. One example is (FDG), a glucose analog that accumulates in cells with high glucose uptake, such as those exposed to inflammatory activity. After entering a cell, FDG is phosphorylated as the first step in the glycolysis pathway, but due to the substitution of the glucose 2-hydroxyl with ^{18}F , it cannot be broken down further or leave the cell. FDG-PET is used extensively in tumor imaging, but has numerous applications including imaging of plaque inflammation in atherosclerosis. Many other radioactive compounds have been used to study atherosclerosis, such as ^{18}F -NaF for imaging plaque calcification [7].

Radionuclide contrast agents can also be constructed by conjugating a radiolabeled isotope to a targeting ligand that is retained via direct binding to its receptor. Antibodies are a commonly used targeting moiety and are advantageous to researchers interested in creating new probes as they can apply previously described radiolabeling techniques [10]. Radiolabeled antibodies have been used for a broad variety of applications, such as characterizing spatio-temporal distribution of T-Cell mediated inflammation using ^{89}Zr -anti-CD3-mAb Peptide and small molecule ligands are also used, such as ^{64}Cu -VEGF, used to quantify surface VEGF receptor expression on the endothelium and provide a measure of angiogenesis [11-13]. Previously described applications of ^{64}Cu -VEGF range from imaging of solid tumors to myocardial ischemia. Another example is ^{125}I -Annexin V, which binds to phosphatidylserine

residues in the cell membrane [7]. Conjugation is typically performed by chemically linking a chelate to the targeting moiety followed by introduction of the isotope.

Selection of radioactive isotope when designing a new probe depends on several considerations such as the kinetics and chemistry of the targeting moiety, radioactive half life, cost, and availability. The half life in commonly used isotopes ranges from 76 seconds (^{121}Rb) to over 78 hours (^{67}Ga). The half life for ^{18}F , one of the most commonly used tracers, is 110 minutes [14]. Some probes require up to a day or more for necessary biodistribution to occur, while others are distributed and cleared quickly. In clinical settings where multiple probes are needed, fast clearance can be advantageous. Type of probe places limitations on isotope selection, as chelation-based linking to targeting moieties requires metal ions, while radioactive compounds more often use non-metal PET tracers such as ^{18}F , ^{11}C , and ^{15}O . Availability of these PET tracers may be a concern in smaller research institutions without access to a nearby cyclotron.

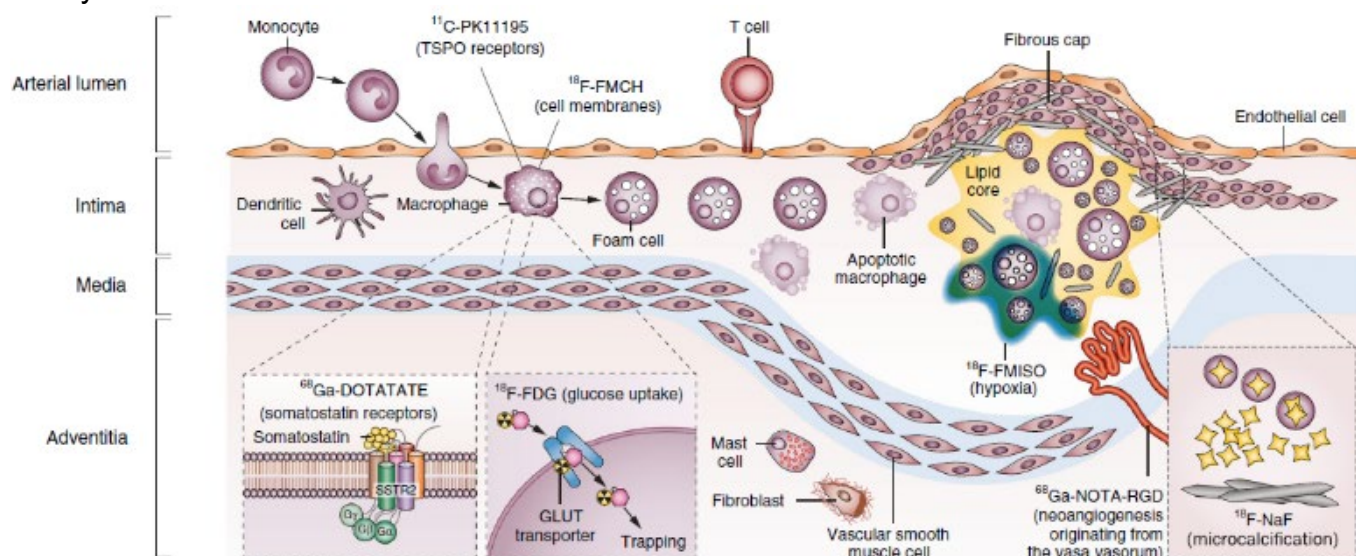


Figure 2: Illustration of pathways involved in atherosclerosis and their radionuclide imaging targets and probes at different anatomical locations and disease stages [15].

Radionuclide tracers can provide assessment of several pathways involved in atherosclerosis. **Figure 2** shows many of the common targets in the study of atherosclerosis along with corresponding RN probes that have been developed. These targeted processes include several markers of macrophage infiltration such as TSPO

and somatostatin receptors, hypoxia, glucose uptake, microcalcification, and neoangiogenesis or formation of plaque vaso vasorum.

Creating a novel probe is often costly and difficult, as commonly used synthesis methods are not necessarily applicable. For radiolabeled compounds, yielding sufficient tracer to be detectable at the necessary levels is often a major hurdle, owing to the rapid decay of many isotopes, the resources involved in producing sufficient amounts in a cyclotron, and complex organic synthesis protocols. Radiolabeled ligands also present synthesis challenges such as ensuring conjugation is homogenous and does not interfere with binding. Chelates are often incorporated to a peptide via linkage to cysteine or lysine residues, so site-specific synthesis protocols are often needed to create a consistent working probe [10]. Success of a probe in vivo also depends on its ability to be cleared from the blood pool while retained tracer can still be detected or to be distinguishable from retained tracer by kinetic modeling. Despite the cost and work associated with development and use of RN molecular imaging probes, they are widely used in research and clinical practice among and can provide excellent quantitative three-dimensional measurements of the endothelial surface.

Magnetic Resonance Molecular Imaging

Magnetic resonance (MR) imaging depends on differences in relaxation of nuclear spin excitation in the presence of a magnetic field. As a molecular imaging technique MR offers incredible spatial resolution and functional imaging capabilities, does not require ionizing radiation, and produces well-defined visualizations of tissue morphology. MR does come with a number of practical and technical limitations such as high equipment cost and space needs, lack of portability, long acquisition times, safety issues introduced from nearby or implanted metal objects, and low sensitivity, among others. One unique advantage of MR is its ability to provide some forms of molecular imaging without the need for contrast, based only on endogenous signal characteristics [9]. The most well-known example of this is blood-oxygen-level-dependent (BOLD) contrast, which takes advantage of the different paramagnetic properties between oxy- and deoxy- hemoglobin in order to image blood flow in the brain or other tissues. Probes for MR molecular imaging have also been developed and typically involve the

attachment of a targeting moiety to a paramagnetic metal such as iron or gadolinium [16-18].

Magnetic Resonance Contrast Agents

Since the principles of MR imaging involve the behavior of atoms in an electric field, paramagnetic metals or compounds are convenient tracers given their ability to stand out from background tissue signal. Common tracers include gadolinium-based contrast agents and micron-sized superparamagnetic Iron Oxide (MPIO), through other tracers such as manganese are in the early exploration phase [19]. MR tracers are typically paired with small molecule targeting moieties but require high binding efficiency and specificity given the sensitivity limits of MR contrast imaging. As with RN imaging, chelation-based conjugation strategies are widely used in synthesis of targeted MR contrast agents. Examples of small molecule MR agents include dextran and dendrimer-based compounds conjugated to iron or gadolinium tracers, which have been used in tumor and perfusion imaging [20-22]. Iron oxide nanoparticles have also been developed as a marker of inflammation, as they are taken up by macrophages and other inflammatory cells, and have been utilized for imaging of tumor metastasis and plaque inflammation in atherosclerosis, among other targets [17, 23-25]. Nanoparticle MR agents present the advantage of being able to cross the blood-brain barrier to measure inflammation and other processes in the brain [16].

Probes have been developed for MR using antibodies and other large molecules, but their practicality and performance compared to other modalities has thus far limited their use. The development of MPIO as a higher sensitivity tracer has allowed for small animal imaging of endothelial activation using targeting moieties such as anti-VCAM-1 mAb [25], which has been applied to measuring neuroinflammation in conditions such as multiple sclerosis. Compared to measurement of neuroinflammation using nanoparticle MR agents, which are hampered by heterogenous and enhanced permeability of the blood-brain barrier in many pathological settings such as solid tumors, antibody or peptide based MR agents that act as intravascular probes can sometimes provide a more reliable readout through measurement of endothelial activation [18].

The practical and technical constraints of MR molecular imaging have somewhat limited its use in research and clinical practice, but when affordable and feasible, it can provide a safer and higher resolution alternative to RN imaging with built in three-dimensional high-resolution structural and morphological imaging and excellent soft tissue contrast [9]. The unique ability of MR to perform molecular imaging using endogenous signal characteristics is advantageous for many reasons such as the ability to rapidly translate and adopt new techniques without the need for development, manufacturing, and regulatory approval of a new probe. Proof-of-concept studies have demonstrated many potential applications of antibody and large molecule based MR agents, but the feasibility and value of these techniques may depend on development of more sensitive tracers and detectors.

Optical Molecular Imaging

Light microscopy is among the most significant innovations in medical and scientific history. The widespread and long-standing use, low cost, simplicity, and versatility of the broader field of optical imaging have led to it becoming ubiquitous across nearly every scientific discipline. As such, the number of optical probes and detectors that have been developed make optical imaging akin to a swiss army knife of imaging techniques. However, the physical constraint of penetration depth limits its use in vivo, especially in the short wave visible spectrum where tissue penetration is typically limited to 2.5mm in tissue [26]. Near infrared (NIR) and infrared (IR) imaging is capable of increased penetration on the cm scale and is used in techniques such as optical coherence tomography (OCT). While X-rays are capable of deep penetration, they involve ionizing radiation, lack soft tissue contrast, and despite a handful of studies demonstrating nanoparticle molecular probes for X-ray imaging, it is not an ideal molecular imaging tool [27].

Fluorescent probes in optical imaging have been a rapidly emerging area of research and draw on a rich history of molecular probe technology that provide a varied toolkit of powerful detection methods, such as FRET for colocalization of different probes, as well as highly specific probes capable of interacting with cellular machinery through processes such as proteolytic fluorophore activation. In vivo optical molecular

imaging is used in research to identify novel pathways and test new therapies and is used clinically not only for diagnostic imaging but increasingly for image-guided surgical procedures such as tumor resection. Optical molecular imaging techniques has even been combined with PET in small animal imaging, which can accelerate development and translation of new probes by providing a means of comparing multi-modality techniques in co-registered images. When feasible, optical molecular imaging provides safe, simple, low cost and often portable and even catheter-based options for clinicians and researchers.

Optical Contrast Agents

Optical contrast agents vary greatly based on the type of detector as well as the tissue and molecular pathway of interest, among other factors. Common methods of detection include fluorescence and luminescence imaging, OCT, and Raman spectroscopy [28-30]. In vivo imaging of fluorescent and luminescent targeted contrast agents can be performed by detectors ranging from large devices designed for whole-body small animal imaging to catheter-based detectors and can produce two-dimensional images or employ fluorescence molecular tomography [6, 31].

Fluorescently labeled probes have been created to target an extremely wide array of processes utilizing antibodies, peptide ligands, small molecules, and nanoparticles, and are frequently available commercially. Fluorescent antibodies are commonly used for studying atherosclerotic plaque composition, but due to their extravasation are not ideal for differentiating events at the endothelial surface [32]. Activation dependent fluorescent and luminescent probes have long been in use in microscopy, and have more recently been incorporated as an in vivo molecular imaging tool. An example of this is imaging of blood ATP levels through light emitted by luciferin after oxidative activation by ATP-dependent firefly luciferase. This technique has been used to study the bioeffects of therapeutic ultrasound, which creates ATP-dependent vasoactivation [33]. While not directly measuring endothelial surface events, ATP molecular imaging is important for studying hypoperfusion due to endothelial dysfunction in the setting of atherosclerosis or post-ischemia. Another example of fluorescent molecular imaging in atherosclerosis is coronary detection of plaque metalloproteinase activity using an intracoronary catheter and protease-activated probe. Many different techniques exist

within fluorescence molecular imaging to meet specific needs, such as Time resolved fluorescence spectroscopy (TRFS), which adds kinetic modeling to standard fluorescence spectroscopy and can measure tracer decay [34].

A widely used clinical tool for optical imaging, OCT is most well known for retinal imaging, given the ability of light to penetrate deep through the translucent vitreous humor and provide high-resolution images without damaging the eye [28]. OCT has high resolution and fast framerates and operates by measuring interferometry in a light-scattering tissue and on a basic level can be thought of as a light analog to B-mode ultrasound imaging. It can employ visible white light which offers good axial resolution, or low-coherence NIR or IR OCT which provide better penetration depth. Contrast agents for OCT can be composed of particles that scatter light, such as gold nanorods, and are capable of providing very high sensitivity even at pM concentrations for some agents [35]. As with other molecular imaging modalities, OCT tracer particles can be conjugated to antibodies and small molecules.

Ultrasound Molecular Imaging

As described in Chapter 2, contrast-enhanced ultrasound (CEU) molecular imaging relies on the ultrasound detection of encapsulated gas microbubbles (MBs) or other acoustically active micro- or nanoparticles that are retained in tissue on the basis of their ability to bind to molecules or cells of interest. CEU has several unique characteristics that differentiate it from other molecular imaging techniques. It is able to rapidly (within 5–10min) obtain non-invasive measures of disease and can be done with portable and relatively inexpensive imaging technology, meaning that bedside molecular imaging is possible. While CEU molecular imaging is currently done using handheld probes, in the future there may be catheter-based options as well. From a research perspective, the rapid imaging protocols and the ability to “null” the signal from the agent provide an opportunity to examine multiple molecular processes in a short period of time. As a purely intravascular probe [36], MBs are an ideal tool for non-invasive interrogation of the endothelial blood pool interface, but they are poorly suited for examining either extravascular or intracellular events. This section will focus on some of

the principles underlying CEU molecular imaging and will highlight recent advancements in the application of targeted CEU to cardiovascular disease

Contrast Agent Properties

CEU imaging relies on receiving signal generated by encapsulated gas MBs when exposed to ultrasound [37]. In the pressure fluctuations of an ultrasound field, MBs undergo volumetric oscillation. Steady expansion and contraction (stable cavitation) occurs at low pressure which can be non-linear with regard to the relationship between pressure and volume [38, 39]. Destruction of microbubbles can occur from exaggerated oscillation at high pressures, known as inertial cavitation [40]. Both inertial cavitation and non-linear stable cavitation result in emission of broad band ultrasound signals and ultrasound energy peaks at harmonic frequencies, thereby producing a unique acoustic signature that can be detected and isolated from background tissue signal [41-43]. Conventional MB agents used in humans are between 1 and 5 μm in diameter, have a core composed of a high-molecular weight inert gas such as perfluorocarbons or sulfur hexafluoride, and have a shell composed of lipids or proteins such as albumin. A wide variety of other acoustically active experimental ultrasound contrast agents has been explored, but are out of the scope of this review [44]. MB agents are smaller than erythrocytes and have a microvascular rheology similar to that of erythrocytes [36, 45]. Accordingly, they normally pass unimpeded through capillaries, which is important for both safety considerations and their use as flow tracers. Lipid MBs also often contain surface “coats” composed of biocompatible polymers such as polyethylene glycol (PEG), which prevent their interaction with cells and plasma proteins [46-48].

After intravenous injection, MBs remain in the vascular space, thereby opacifying the blood pool on ultrasound imaging. In clinical cardiovascular medicine, CEU is most often used to opacify the left ventricular (LV) cavity on echocardiography in order to better evaluate global or regional function, LV dimensions, and the presence of intracavitary masses such as thrombi [49]. Myocardial contrast echocardiography (MCE) for evaluation of regional myocardial perfusion can also be performed with conventional MB agents, during which blood flow is quantified by measuring the rate

and extent of replenishment of MBs within the coronary circulation after a destructive ultrasound pulse [50, 51].

Molecular imaging with CEU is most commonly performed by imaging targeted MBs that have been retained by attachment to specific molecular processes within the vascular compartment. The retention of MBs can occur by two distinct approaches. Non-specific retention of MBs, by their binding to endothelial cells or to adherent and activated leukocytes, occurs through the endogenous ability of these cells to bind to MB shell constituents. There are many pathways involved in this binding, but the process that has been best defined is opsonization, whereby serum complement proteins bind to the MB surface and are then recognized by complement receptors on leukocytes or on endothelial cells [52, 53]. Choice of shell composition, charge and the presence of PEG all play key roles in determining the degree of MB attachment to leukocytes and endothelial cells, as well as the rate of their removal from the reticuloendothelial system [47, 54, 55]. These non-specific interactions with MBs can be leveraged for detecting pathological processes that heighten opsonization or complement-mediated attachment, as is the case with MBs with phosphatidylserine shells, which are known to preferentially bind in regions of ischemic myocardium [56].

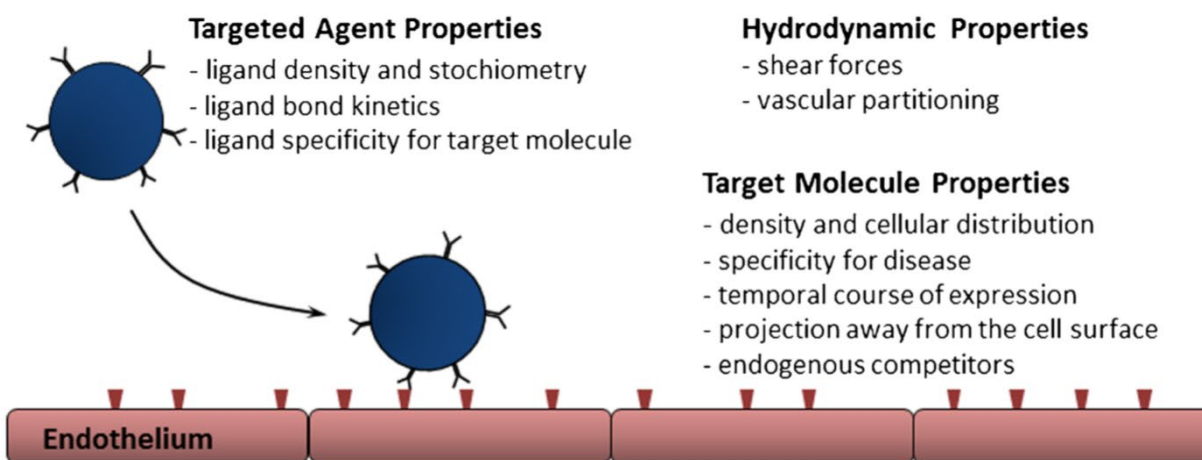


Figure 3: Major determinants of targeted microbubble retention in areas of disease. Factors that influence microbubble retention are separated into contrast agent variables, target molecular variables, and hydrodynamic properties

An alternate and more specific strategy for targeting of MBs occurs via direct binding of a targeting ligand on the MB surface, often an antibody, peptide, or

glycoprotein [57, 58]. Targeting ligands are attached to the MB surface via a variety of approaches, including biotin-streptavidin and direct covalent links. Conjugation is often at the end of the flexible PEG tethers in order to improve stoichiometry and reduce necessary bond force for retention [59]. In general, in excess of 25,000 ligands can be conjugated to each “multivalent” MB [60] and it is even possible to place several different ligands on each MB which may enhance their attachment efficiency [61]. Specificity of an MB probe for a target molecule is determined by factors such as off-target binding, specificity of the targeting ligand to the molecule of interest, bond kinetics, surface density of the targeting ligand, orientation of targeting ligands, and other factors shown in **Figure 3** [62]. Even with a highly specific probe, it is important to consider target molecule characteristics such as regional and temporal expression patterns, relevance of the target molecule to the disease pathway of interest, and bond kinetics under varying shear conditions.

In Vivo Protocol for Targeted CEU

There are several approaches used to detect targeted MB retention in tissue with ultrasound. Since circulating MBs are rapidly cleared by the reticuloendothelial system, it is possible to simply inject MBs as a venous bolus injection, then measure signal intensity for tracer retained in tissue 5–10min late, after the majority of freely circulating MBs have been cleared from the blood pool. The efficacy of this approach is further enhanced by protocols to eliminate the signal attributable to any remaining freely circulating MBs [57]. An alternative and somewhat more complex method is to use transfer kinetics to evaluate the retention fraction. With this method, one must measure video intensity constantly after an intravenous injection, and then deconvolve the curve that represent freely circulating tracer, and the curve representing tracer that is retained [63]. This latter method is particularly helpful in research settings where tissue perfusion, which influences the number of micro bubbles entering into tissue, changes substantially over time or between conditions.

Strengths and Limitations of CEU Molecular Imaging

Whether using molecular imaging as a research tool or for a clinical application, the selection of the most appropriate modality for any given application requires one to consider the relative advantages and disadvantages for each approach. For molecular imaging approaches that use targeted contrast agents, one important consideration is the biodistribution of the targeted probe relative to the target pathway. A limitation of CEU molecular imaging is that the imaging probes are restricted to the vascular compartment. Hence, CEU is not an ideal method for finding abnormal cell types within atherosclerotic plaque or for detecting abnormal matrix composition in certain myocardial diseases. On the other hand, in conditions where it is desirable to limit the evaluation to endothelial or intraluminal phenotype (e.g., transplant vasculopathy, thrombosis), techniques that employ purely intravascular probes may offer advantage in terms of specificity. There are other key differences between small molecule contrast agents and larger multivalent particle-based agents. The former generally bind in a 1:1 ratio to a target receptor or are retained by virtue of a metabolic process and are well suited to precisely quantifying the degree of expression or enzymatic activity [64]. For the latter, many bond formations have to occur for retention, resulting in a threshold-effect with regard to target molecular expression before attachment is seen, and a greater influence of vascular shear [65]. However, particle-based agents provide a form of biomimicry where their behavior can provide a readout of the molecular environment that influences cellular or platelet adhesion.

There are also practical considerations in terms of detector performance. In general, techniques such as MRI and CT are considered to have the highest spatial resolution, while radionuclide imaging (PET, SPECT) tends to have the highest sensitivity and dynamic range for detecting tracer. Accordingly, one must consider whether it is more important to spatially localize an event or to be able to detect very low levels of abnormal molecular expression. In general, CEU molecular imaging offers a balance in that it provides moderate spatial resolution and sensitivity, and is suitable for applications where a balance of both traits is needed. If it is necessary to co-localize regional molecular imaging signal with anatomical features, CEU has the advantage of near simultaneous structural and molecular imaging, while MR and hybrid PET-CT or

SPECT-CT have the advantage of providing more detailed views of smaller anatomical features.

Temporal resolution is also essential to consider when selecting the most appropriate molecular imaging modality. CEU molecular imaging can be performed with rapid acquisition times of less than 10 min, while commonly used PET/SPECT and MR protocols require anywhere from just under an hour to a day between contrast injection and imaging [66-68]. Additionally, rapid clearance of MBs from the blood pool allows multiple different targeted contrast agents to be administered sequentially.

There are certain practical issues other than speed that are important when considering different molecular imaging modalities, particularly if their use is intended as an approach for disease screening in large populations or for rapid detection in common diseases (e.g., myocardial ischemia, atherosclerosis). Safety is one key issue. CEU contrast agents have an excellent safety profile, with serious pseudo-anaphylactic reactions occurring in only 1 in 10,000 for conventional contrast agents [69-72]. An additional advantage of CEU molecular imaging is the relative ease and low cost of developing novel probes. Since radioactive decay is not a concern and conjugation chemistry is well described and fairly consistent, the main hurdle is often simply finding the best ligand. CEU molecular imaging also does not require ionizing radiation. Other advantages include ease of use, portability of ultrasound which allows for bedside diagnosis, and low cost for both equipment and production of contrast agents.

Applications of CEU Molecular Imaging

Ischemic Memory Imaging

In patients with acute coronary syndrome (ACS), the clinical diagnosis generally relies on clinical history, laboratory evaluation, and electrocardiogram (ECG). Unfortunately, many patients do not have classic angina symptoms [73], and many of those with ACS do not have diagnostic changes on the ECG [74]. Moreover, in those with unstable angina, ECG changes and even wall motion abnormalities detectable on point-of-care echocardiography can resolve before the initial evaluation by a healthcare provider. While high-sensitivity troponins have a high sensitivity for detecting non-ST-

elevation MI [75], their performance in unstable angina is less certain, and they often lack specificity in certain populations [76]. Methods for rapidly evaluating both the presence and the spatial extent of recently resolved myocardial ischemia have a high likelihood of improving the quality and efficiency of clinical care in those presenting with symptoms suspicious for ACS.

CEU molecular imaging is capable of assessing ongoing or recent, but resolved, myocardial ischemia at the patient bedside and provides a spatial readout of the affected area. Ischemic memory imaging has been achieved both with MBs bearing targeting ligands for the endothelial selectin family of adhesion molecules and with phosphatidylserine containing MBs (PS-MB) (Figure 4) [56, 77, 78]. Targeting of selectins on the endothelial surface, which has been validated in murine and non-human primate models of myocardial infarction, is based on early and late endothelial response to ischemia. In the first minutes following ischemia, P-selectin stored in endothelial Weibel-Palade bodies is mobilized to the cell surface where it can remain for many hours, whereas E-selectin expression requires approximately 1 h to be expressed due to its dependence on transcriptional upregulation [79]. Agents targeted to selectins are thereby retained in the microcirculation of the post-ischemic risk area, even in the absence of any significant necrosis, for hours after resolution of hypoperfusion.

Alternatively, ischemic memory imaging can be performed without a targeting ligand using PSMBs, as validated in murine and canine models of resolved myocardial ischemia [56]. The selective retention of phosphatidylserine MBs in areas of recent ischemia is mediated in part through opsonization and binding to complement receptors. The simplicity of this approach will likely accelerate its clinical translation.

Detection of Transplant Rejection or Myocarditis

Orthotopic heart transplantation is an important therapeutic option for eligible candidates with severely symptomatic heart failure. However, there have been a relatively flat number of allografts available for transplant in the USA each year. Approximately one-quarter of all allografts have evidence for rejection in the first year [80]. This figure together with the problem of sampling error for detecting rejection by

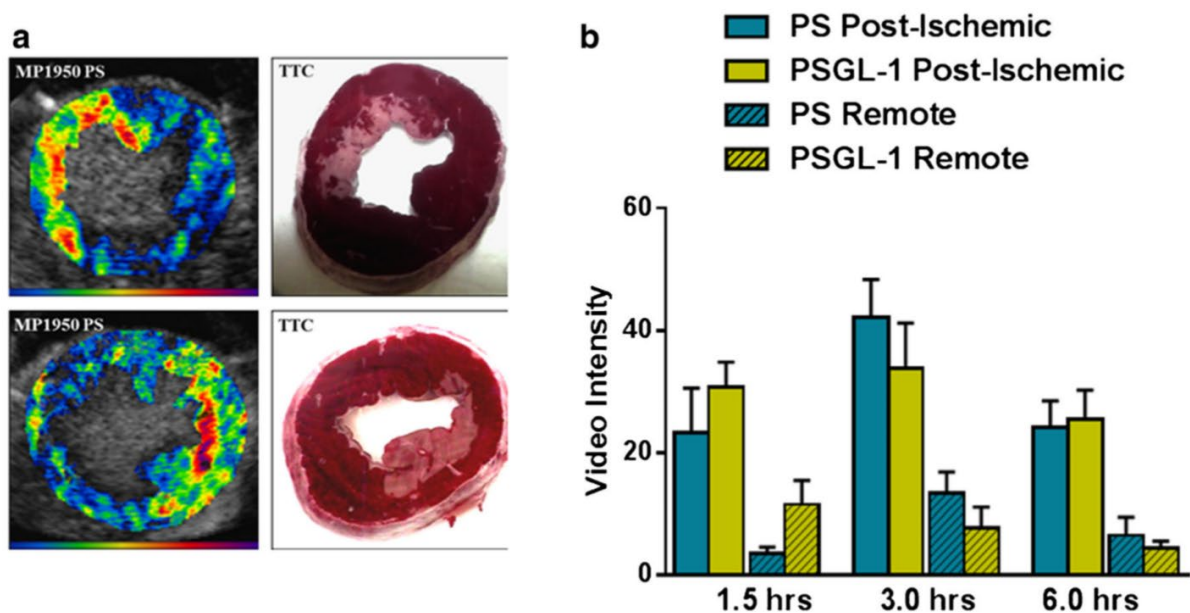


Figure 4: Molecular imaging of ischemic memory. a Examples of CEU molecular imaging with MB-PS (left panels) and triphenyltetrazolium chloride (TTC) staining (right panels) in a canine model of ischemia reperfusion of the LAD (top panels) or left circumflex coronary artery (bottom panels). Images demonstrate contrast enhancement that encompasses the entire risk area which extends beyond the region of infarction. The color-coded scale for CEU is provided at the bottom (modified from Christiansen JP et al. *Circulation* 2002 Apr 16;105(15):1764–7) [75]. b Graph illustrating signal enhancement on CEU molecular imaging from a murine model of brief ischemia reperfusion injury without infarction. Signal enhancement in the postischemic risk area was greater than in the remote area and was similar for MB-PS and P-selectin-targeted MBs and persisted for >6 h after ischemic injury. PS phosphatidylserine, PSGL-1 p-selectin glycoprotein ligand-1 (modified from Mott B, et al. *Cardiovasc Imaging*. 2016;9(8):937–46, with permission from Elsevier) [26]

endomyocardial biopsy has resulted in a need for better surveillance. Molecular imaging for this application would require a technique that ideally could be done rapidly and without repetitive exposure to ionizing radiation. The ability to detect transplant rejection has been demonstrated in a rat model using MBs targeted to ICAM-1 [81]. This study was predicated on the notion that rejection involved not only a T lymphocytic response to myocytes but also to the allograft endothelial cells resulting in endothelial activation and adhesion molecule expression. More recently, CEU molecular imaging has been used to directly assess T lymphocytes in a model of orthotopic heart transplantation [82]. This study relied on MBs bearing a CD3-targeted antibody that allowed them to assess lymphocytes in the process of intravascular recruitment.

The pathophysiology of myocarditis involves many common pathways with heart transplant rejection, and the most important of which involves recruitment of cells involved in both adaptive and innate immunity. Accordingly, CEU with MBs targeted to selectins, CD4, and phagocytic cells have been used in a rodent model of myocarditis and shown to detect not only severe fulminant disease but also more moderate involvement as well [83]. Because of the rapid and quantitative nature of CEU, and its ability to provide information immediately to the clinician, there is hope that it may provide unique diagnostic opportunities for all of these forms of myocardial inflammation in the future.

Atherosclerosis and Platelet-Endothelial Interactions

Atherosclerosis is a process that develops over decades and involves vascular inflammation, including expression of endothelial cell adhesion molecules (ECAMs) and secondary recruitment of leukocytes and platelets [84, 85]. Often, atherosclerosis is clinically silent for decades of plaque progression. Although biomarkers and other techniques have been developed for risk-stratifying patients [86, 87], many patients with severe atherosclerotic disease will not have major risk factors and many will experience MI as their first manifestation of disease [88]. Often, patients are diagnosed only once disease progression has reached the point of critical stenosis, which results in angina [60]. The ability to non-invasively detect the early molecular signatures of aggressive atherosclerosis may provide opportunity for early stratification to therapies that can arrest disease development. CEU is just one of many molecular imaging techniques that have been used to detect atherosclerotic plaque growth in the early stages of disease. CEU probes targeted against ECAMs including selectins, ICAM-1, and VCAM-1 have been shown to detect early and late stage atherosclerosis in rodent models of atherosclerosis [89-93]. In non-human primates on a Western diet, CEU molecular imaging of VCAM-1 and P-selectin has been shown to detect the very earliest stages of endothelial activation prior to any changes in intima media thickness [94, 95]

Recently, CEU molecular imaging of endothelial phenotype has provided in vivo evidence for the role of platelet-endothelial interactions in early disease progression [94, 95]. This process, first demonstrated in murine models of hypercholesterolemia involves

abnormal regulation of endothelial associated ultra-large multimers of VWF that mediate platelet attachment through ligation of platelet GPIIb/IIIa and increase atherosclerotic progression [85]. Similar results were observed in an insulin-resistant model of non-human primates fed a western style diet (WSD), made possible by the development of a small peptide mimicking the binding region of VWF A1 and functionalized for conjugation to MBs, creating a GPIIb/IIIa-targeted agent.

While these probes were developed for early detection of disease, they have also played an important role in identifying new therapeutic targets and for assessing the effects of either new or established therapies [91, 96, 97]. CEU was used in both murine and primate models of early atherosclerosis to demonstrate the efficacy of targeted antioxidant therapy with apocynin, an NADPH-oxidase inhibitor and broad-spectrum antioxidant, in reducing endothelial activation and platelet binding. Figure 5 shows CEU results from primates treated with apocynin and the full study can be found in Chapter 5. Platelet- and VWF- targeted CEU agents have also proved useful in researching other clinical situations in which platelet-endothelial interactions are of interest, including post-ischemic acceleration of atherosclerotic plaque growth and diffuse thrombotic microangiopathies in patients on and increased risk for atherothrombotic events caused by tyrosine kinase inhibitor therapy. These cases are discussed in detail in Chapters 6 and 7, respectively.

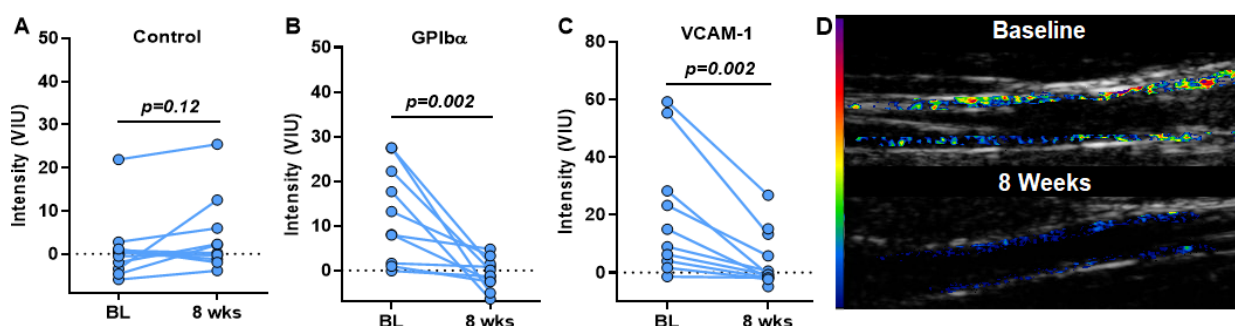


Figure 5: Individual data for CEU molecular imaging signal in WSD-fed animals at baseline (BL) and after 8 weeks of apocynin therapy for (A) control MB, (B) GPIIb/IIIa-targeted MB, and (C) VCAM-1-targeted MB. (D) Example carotid artery CEU molecular imaging of platelet GPIIb/IIIa (background-subtracted and color coded [scale at left] signal superimposed on a co-registered two-dimensional B-mode image) from an obese animal at baseline and after 8 weeks of apocynin therapy.

Thrombus Detection

There are many potential applications for a technique that can detect the presence of thrombus in cardiovascular disease. Some of the most common include need to diagnosis acute venous or peripheral arterial thrombus, detection of high-risk carotid or coronary arterial plaque, detection of left atrial or left ventricular thrombus, and detection of microvascular thrombosis in post-MI no-reflow phenomenon. Molecular imaging of thrombus has been performed with a variety of targeted ultrasound contrast agents [98]. The targeting moiety employed depends on the intended role of molecular imaging. MBs have been targeted by surface conjugation of ligands that recognize the platelet GPIIb/IIIa receptor, fibrin, or tissue factor [58, 99-101] As mentioned above, MBs have also been targeted to platelet GPIb α and VWF using peptide ligands for each. The relative value of each of these agents depends on (1) whether the thrombotic process of interest is platelet-rich or fibrin-rich; (2) the shear forces in the chamber/vessel involved; and (3) whether the process involves disruption of the endothelial barrier or not. An additional consideration is whether or not MBs need to outcompete endogenous ligands for the intended target. For example, MBs need to outcompete fibrinogen for GPIIb/IIIa, but little competition exists for GPIb α .

Summary

Molecular imaging techniques across modalities provide unique value to both clinicians and researchers, with significant recent development creating agents targeted to a broad array of molecular targets both inside and outside the vascular space. Selection of the ideal tool for a specific application requires consideration of both the technological and physical capabilities and limitations of the probe as well as biochemical, physical and physiological characteristics of how the probe is distributed and retained. These techniques can be leveraged to define pathophysiology, test the efficacy and guide new therapies, risk stratify patients, and provide diagnostic imaging.

CEU molecular imaging is a versatile technique that has many potential applications in clinical cardiovascular medicine and is already being used as a valuable research tool to understand cellular biology in disease. The technique is well suited to evaluating pathophysiologic events that occur at the interface between the blood pool

and the vessel wall. While other molecular imaging modalities are useful in vascular imaging for measurements such as inflammatory activity within a plaque or endothelial surface expression of inflammatory markers, they often are costly, involve long acquisition times, are performed by large and stationary machines, and require ionizing radiation. CEU occupies a niche in providing low-cost, functional, rapidly obtained information on cellular interactions at the endothelial surface without the need for ionizing radiation and with simultaneous structural imaging. Additionally, CEU can be performed at the bedside or in small laboratories that do not have space for or access to machinery involved in RN, MR, and CT imaging.

Accordingly, the most common cardiovascular applications of targeted CEU have involved imaging of endothelial activation, endothelial adhesion molecule expression, thrombus formation, and interactions between leukocytes or platelets and the vascular endothelium. However, clinical adoption will rely on both the development and testing of human-ready targeted contrast agents, and demonstration that CEU molecular imaging provides incremental value to conventional paradigms of care.

References

1. Osborn EA, Jaffer FA. The advancing clinical impact of molecular imaging in CVD. *JACC Cardiovasc Imaging*. 2013;6(12):1327-41.
2. Chen Z-Y, Wang Y-X, Lin Y, Zhang J-S, Yang F, Zhou Q-L, et al. Advance of Molecular Imaging Technology and Targeted Imaging Agent in Imaging and Therapy. *BioMed Research International*. 2014;2014:819324.
3. Lindner JR, Sinusas A. Molecular imaging in cardiovascular disease: Which methods, which diseases? *Journal of Nuclear Cardiology*. 2013;20(6):990-1001.
4. Sinusas AJ, Bengel F, Nahrendorf M, Epstein FH, Wu JC, Villanueva FS, et al. Multimodality cardiovascular molecular imaging, part I. *Circ Cardiovasc Imaging*. 2008;1(3):244-56.
5. Vaidyanathan S, Patel CN, Scarsbrook AF, Chowdhury FU. FDG PET/CT in infection and inflammation--current and emerging clinical applications. *Clinical radiology*. 2015;70(7):787-800.
6. Nahrendorf M, Sosnovik DE, French BA, Swirski FK, Bengel F, Sadeghi MM, et al. Multimodality cardiovascular molecular imaging, Part II. *Circulation Cardiovascular imaging*. 2009;2(1):56-70.
7. Pysz MA, Gambhir SS, Willmann JK. Molecular imaging: current status and emerging strategies. *Clinical radiology*. 2010;65(7):500-16.
8. Pektor S, Schlöder J, Klasen B, Bausbacher N, Wagner DC, Schreckenberger M, et al. Using immuno-PET imaging to monitor kinetics of T cell-mediated inflammation and treatment efficiency in a humanized mouse model for GvHD. *Eur J Nucl Med Mol Imaging*. 2020;47(5):1314-25.

9. Lindner JR, Sinusas A. Molecular imaging in cardiovascular disease: Which methods, which diseases? *J Nucl Cardiol*. 2013;20(6):990-1001.
10. Wu Y, Zhu H, Zhang B, Liu F, Chen J, Wang Y, et al. Synthesis of Site-Specific Radiolabeled Antibodies for Radioimmunotherapy via Genetic Code Expansion. *Bioconjugate Chemistry*. 2016;27(10):2460-8.
11. Chen K, Cai W, Li Z-B, Wang H, Chen X. Quantitative PET Imaging of VEGF Receptor Expression. *Molecular Imaging and Biology*. 2009;11(1):15-22.
12. Nagengast WB, Lub-de Hooge MN, Oosting SF, den Dunnen WF, Warnders FJ, Brouwers AH, et al. VEGF-PET imaging is a noninvasive biomarker showing differential changes in the tumor during sunitinib treatment. *Cancer Res*. 2011;71(1):143-53.
13. Hendrikx G, Vöö S, Bauwens M, Post MJ, Mottaghy FM. SPECT and PET imaging of angiogenesis and arteriogenesis in pre-clinical models of myocardial ischemia and peripheral vascular disease. *European journal of nuclear medicine and molecular imaging*. 2016;43(13):2433-47.
14. Nayak TK, Brechbiel MW. Radioimmunoimaging with longer-lived positron-emitting radionuclides: potentials and challenges. *Bioconjugate chemistry*. 2009;20(5):825-41.
15. Celeng C, de Keizer B, Merkely B, de Jong P, Leiner T, Takx RAP. PET Molecular Targets and Near-Infrared Fluorescence Imaging of Atherosclerosis. *Current Cardiology Reports*. 2018;20(2):11.
16. Huang C-H, Tsourkas A. Gd-based macromolecules and nanoparticles as magnetic resonance contrast agents for molecular imaging. *Curr Top Med Chem*. 2013;13(4):411-21.
17. McAteer MA, Schneider JE, Ali ZA, Warrick N, Bursill CA, von zur Muhlen C, et al. Magnetic resonance imaging of endothelial adhesion molecules in mouse atherosclerosis using dual-targeted microparticles of iron oxide. *Arteriosclerosis, thrombosis, and vascular biology*. 2008;28(1):77-83.
18. Gauberti M, Fournier AP, Docagne F, Vivien D, Martinez de Lizarrondo S. Molecular Magnetic Resonance Imaging of Endothelial Activation in the Central Nervous System. *Theranostics*. 2018;8(5):1195-212.
19. Zhen Z, Xie J. Development of manganese-based nanoparticles as contrast probes for magnetic resonance imaging. *Theranostics*. 2012;2(1):45-54.
20. Bryant LH, Jr., Brechbiel MW, Wu C, Bulte JW, Herynek V, Frank JA. Synthesis and relaxometry of high-generation (G = 5, 7, 9, and 10) PAMAM dendrimer-DOTA-gadolinium chelates. *J Magn Reson Imaging*. 1999;9(2):348-52.
21. Mardiguian S, Serres S, Ladds E, Campbell SJ, Wilainam P, McFadyen C, et al. Anti-IL-17A treatment reduces clinical score and VCAM-1 expression detected by in vivo magnetic resonance imaging in chronic relapsing EAE ABH mice. *Am J Pathol*. 2013;182(6):2071-81.
22. Wang SC, Wikström MG, White DL, Klaveness J, Holtz E, Rongved P, et al. Evaluation of Gd-DTPA-labeled dextran as an intravascular MR contrast agent: imaging characteristics in normal rat tissues. *Radiology*. 1990;175(2):483-8.
23. Kuriu Y, Otsuji E, Kin S, Nakase Y, Fukuda K, Okamoto K, et al. Monoclonal antibody conjugated to gadolinium as a contrast agent for magnetic resonance imaging of human rectal carcinoma. *J Surg Oncol*. 2006;94(2):144-8.
24. Trivedi Rikin A, Mallawarachi C, Jean-Marie UK-I, Graves Martin J, Horsley J, Goddard Martin J, et al. Identifying Inflamed Carotid Plaques Using In Vivo USPIO-Enhanced MR Imaging to Label Plaque Macrophages. *Arteriosclerosis, Thrombosis, and Vascular Biology*. 2006;26(7):1601-6.
25. Serres S, Mardiguian S, Campbell SJ, McAteer MA, Akhtar A, Krapitchev A, et al. VCAM-1-targeted magnetic resonance imaging reveals subclinical disease in a mouse model of multiple sclerosis. *Faseb j*. 2011;25(12):4415-22.

26. Zhang H, Salo D, Kim DM, Komarov S, Tai Y-C, Berezin MY. Penetration depth of photons in biological tissues from hyperspectral imaging in shortwave infrared in transmission and reflection geometries. *J Biomed Opt.* 2016;21(12):126006-.
27. Pratz G, Carpenter CM, Sun C, Rao RP, Xing L. Tomographic molecular imaging of x-ray-excitable nanoparticles. *Opt Lett.* 2010;35(20):3345-7.
28. Mattison SP, Kim W, Park J, Applegate BE. Molecular Imaging in Optical Coherence Tomography. *Curr Mol Imaging.* 2014;3(2):88-105.
29. MacRitchie N, Grassia G, Noonan J, Garside P, Graham D, Maffia P. Molecular imaging of atherosclerosis: spotlight on Raman spectroscopy and surface-enhanced Raman scattering. *Heart.* 2018;104(6):460.
30. Chang SK, Rizvi I, Solban N, Hasan T. In vivo optical molecular imaging of vascular endothelial growth factor for monitoring cancer treatment. *Clin Cancer Res.* 2008;14(13):4146-53.
31. Stephens DN, Park J, Sun Y, Papaioannou T, Marcu L. Intraluminal fluorescence spectroscopy catheter with ultrasound guidance. *J Biomed Opt.* 2009;14(3):030505-.
32. Nahrendorf M, Jaffer Farouc A, Kelly Kimberly A, Sosnovik David E, Aikawa E, Libby P, et al. Noninvasive Vascular Cell Adhesion Molecule-1 Imaging Identifies Inflammatory Activation of Cells in Atherosclerosis. *Circulation.* 2006;114(14):1504-11.
33. Belcik JT, Mott BH, Xie A, Zhao Y, Kim S, Lindner NJ, et al. Augmentation of limb perfusion and reversal of tissue ischemia produced by ultrasound-mediated microbubble cavitation. *Circ Cardiovasc Imaging.* 2015;8(4).
34. Boreham A, Brodewolf R, Walker K, Haag R, Alexiev U. Time-Resolved Fluorescence Spectroscopy and Fluorescence Lifetime Imaging Microscopy for Characterization of Dendritic Polymer Nanoparticles and Applications in Nanomedicine. *Molecules.* 2016;22(1):17.
35. Liba O, SoRelle ED, Sen D, de la Zerda A. Contrast-enhanced optical coherence tomography with picomolar sensitivity for functional in vivo imaging. *Scientific reports.* 2016;6:23337-.
36. Lindner JR, Song J, Jayaweera AR, Sklenar J, Kaul S. Microvascular rheology of Definity microbubbles after intra-arterial and intravenous administration. *Journal of the American Society of Echocardiography.* 2002;15(5):396-403.
37. Kaufmann BA, Wei K, Lindner JR. Contrast Echocardiography. *Curr Probl Cardiol.* 2007;32(2):51-96.
38. Jong ND, Frinking P, Cate FT, Wouw PVD, editors. Characteristics of contrast agents and 2D imaging. 1996 IEEE Ultrasonics Symposium Proceedings; 1996 3-6 Nov. 1996.
39. Overvelde M, Garbin V, Sijl J, Dollet B, de Jong N, Lohse D, et al. Nonlinear Shell Behavior of Phospholipid-Coated Microbubbles. *Ultrasound in Medicine & Biology.* 2010;36(12):2080-92.
40. Shi WT, Forsberg F, Tornes A, Ostensen J, Goldberg BB. Destruction of contrast microbubbles and the association with inertial cavitation. *Ultrasound Med Biol.* 2000;26(6):1009-19.
41. Burns PN. Harmonic imaging with ultrasound contrast agents. *Clinical radiology.* 1996;51(SUPPL. 1):50-5.
42. Burns PN, Powers JE, Simpson DH, Brezina A, Kolin A, Chin CT, et al., editors. Harmonic power mode Doppler using microbubble contrast agents: an improved method for small vessel flow imaging. 1994 Proceedings of IEEE Ultrasonics Symposium; 1994 31 Oct.-3 Nov. 1994.
43. Simpson DH, Chien Ting C, Burns PN. Pulse inversion Doppler: a new method for detecting nonlinear echoes from microbubble contrast agents. *IEEE Transactions on Ultrasonics, Ferroelectrics, and Frequency Control.* 1999;46(2):372-82.
44. Paefgen V, Doleschel D, Kiessling F. Evolution of contrast agents for ultrasound imaging and ultrasound-mediated drug delivery. *Frontiers in Pharmacology.* 2015;6:197.

45. Ismail S, Jayaweera AR, Camarano G, Gimple LW, Powers ER, Kaul S. Relation between air-filled albumin microbubble and red blood cell rheology in the human myocardium. Influence of echocardiographic systems and chest wall attenuation. *Circulation*. 1996;94(3):445-51.
46. Du H, Chandaroy P, Hui SW. Grafted poly-(ethylene glycol) on lipid surfaces inhibits protein adsorption and cell adhesion. *Biochimica et Biophysica Acta (BBA) - Biomembranes*. 1997;1326(2):236-48.
47. Fisher NG, Christiansen JP, Klibanov A, Taylor RP, Kaul S, Lindner JR. Influence of microbubble surface charge on capillary transit and myocardial contrast enhancement. *Journal of the American College of Cardiology*. 2002;40(4):811-9.
48. Chen CC, Borden MA. Ligand Conjugation to Bimodal Poly(ethylene glycol) Brush Layers on Microbubbles. *Langmuir*. 2010;26(16):13183-94.
49. Senior R, Becher H, Monaghan M, Agati L, Zamorano J, Vanoverschelde JL, et al. Clinical practice of contrast echocardiography: recommendation by the European Association of Cardiovascular Imaging (EACVI) 2017. *European heart journal cardiovascular Imaging*. 2017;18(11):1205-af.
50. Wei K, Jayaweera AR, Firoozan S, Linka A, Skyba DM, Kaul S. Quantification of myocardial blood flow with ultrasound-induced destruction of microbubbles administered as a constant venous infusion. *Circulation*. 1998;97(5):473-83.
51. Kaul S, Kelly P, Oliner JD, Glasheen WP, Keller MW, Watson DD. Assessment of regional myocardial blood flow with myocardial contrast two-dimensional echocardiography. *Journal of the American College of Cardiology*. 1989;13(2):468 - 82.
52. Lindner JR, Song J, Xu F, Klibanov AL, Singbartl K, Ley K, et al. Noninvasive ultrasound imaging of inflammation using microbubbles targeted to activated leukocytes. *Circulation*. 2000;102(22):2745-50.
53. Anderson DR, Tsutsui JM, Xie F, Radio SJ, Porter TR. The role of complement in the adherence of microbubbles to dysfunctional arterial endothelium and atherosclerotic plaque. *Cardiovasc Res*. 2007;73(3):597-606.
54. Yanagisawa K, Moriyasu F, Miyahara T, Yuki M, Iijima H. Phagocytosis of ultrasound contrast agent microbubbles by Kupffer cells. *Ultrasound in Medicine & Biology*. 2007;33(2):318 - 25.
55. Chen CC, Borden MA. The role of poly(ethylene glycol) brush architecture in complement activation on targeted microbubble surfaces. *Biomaterials*. 2011;32(27):6579-87.
56. Mott B, Packwood W, Xie A, Belcik JT, Taylor RP, Zhao Y, et al. Echocardiographic Ischemic Memory Imaging Through Complement-Mediated Vascular Adhesion of Phosphatidylserine-Containing Microbubbles. *JACC Cardiovasc Imaging*. 2016;9(8):937-46.
57. Lindner JR, Song J, Christiansen J, Klibanov AL, Xu F, Ley K. Ultrasound Assessment of Inflammation and Renal Tissue Injury With Microbubbles Targeted to P-Selectin. *Circulation*. 2001;104(17):2107-12.
58. Unger EC, McCreery TP, Sweitzer RH, Shen D, Wu G. In vitro studies of a new thrombus-specific ultrasound contrast agent. *The American Journal of Cardiology*. 1998;81(12, Supplement 1):58G-61G.
59. Klibanov AL, Gu H, Wojdyla JK, Wible JH, Kim DH, Needham D, et al. Attachment of ligands to gas-filled microbubbles via PEG spacer and lipid residues anchored at the interface. *Proceedings of 26th International Symposium on Controlled Release of Bioactive Materials*. 1999:124-5.
60. Takalkar AM, Klibanov AL, Rychak JJ, Lindner JR, Ley K. Binding and detachment dynamics of microbubbles targeted to P-selectin under controlled shear flow. *Journal of controlled release : official journal of the Controlled Release Society*. 2004;96(3):473-82.
61. Ferrante EA, Pickard JE, Rychak J, Klibanov A, Ley K. Dual targeting improves microbubble contrast agent adhesion to VCAM-1 and P-selectin under flow. *Journal of controlled release : official journal of the Controlled Release Society*. 2009;140(2):100-7.
62. Behm CZ, Lindner JR. Cellular and molecular imaging with targeted contrast ultrasound. *Ultrasound quarterly*. 2006;22(1):67-72.

63. Carr CL, Qi Y, Davidson B, Chadderdon S, Jayaweera AR, Belcik JT, et al. Dysregulated Selectin Expression and Monocyte Recruitment During Ischemia-related Vascular Remodeling in Diabetes Mellitus. *Arteriosclerosis, thrombosis, and vascular biology*. 2011;31(11):2526-33.
64. Truillet C, Oh HLJ, Yeo SP, Lee CY, Huynh LT, Wei J, et al. Imaging PD-L1 Expression with ImmunoPET. *Bioconjugate chemistry*. 2018;29(1):96-103.
65. Weller GER, Villanueva FS, Klibanov AL, Wagner WR, editors. Shear modulates adhesion of ultrasound contrast microbubbles targeted to dysfunctional endothelium. *Proceedings of the Second Joint 24th Annual Conference and the Annual Fall Meeting of the Biomedical Engineering Society* [Engineering in Medicine and Biology; 2002 23-26 Oct. 2002].
66. Alie N, Eldib M, Fayad ZA, Mani V. Inflammation, Atherosclerosis, and Coronary Artery Disease: PET/CT for the Evaluation of Atherosclerosis and Inflammation. *Clinical Medicine Insights Cardiology*. 2014;8(Suppl 3):13-21.
67. Klein C, Schmal TR, Nekolla SG, Schnackenburg B, Fleck E, Nagel E. Mechanism of late gadolinium enhancement in patients with acute myocardial infarction. *Journal of cardiovascular magnetic resonance : official journal of the Society for Cardiovascular Magnetic Resonance*. 2007;9(4):653-8.
68. Winter PM, Caruthers SD, Lanza GM, Wickline SA. Quantitative cardiovascular magnetic resonance for molecular imaging. *Journal of cardiovascular magnetic resonance : official journal of the Society for Cardiovascular Magnetic Resonance*. 2010;12:62.
69. Kurt M, Shaikh KA, Peterson L, Kurrelmeyer KM, Shah G, Nagueh SF, et al. Impact of Contrast Echocardiography on Evaluation of Ventricular Function and Clinical Management in a Large Prospective Cohort. *Journal of the American College of Cardiology*. 2009;53(9):802-10.
70. Goldberg YH, Ginelli P, Siegel R, Ostfeld RJ, Schaefer M, Spevack DM. Administration of perflutren contrast agents during transthoracic echocardiography is not associated with a significant increase in acute mortality risk. *Cardiology*. 2012;122(2):119-25.
71. Platts DG, Luis SA, Roper D, Burstow D, Call T, Forshaw A, et al. The safety profile of perflutren microsphere contrast echocardiography during rest and stress imaging: results from an Australian multicentre cohort. *Heart, lung & circulation*. 2013;22(12):996-1002.
72. Liu YN, Khangura J, Xie A, Belcik JT, Qi Y, Davidson BP, et al. Renal retention of lipid microbubbles: a potential mechanism for flank discomfort during ultrasound contrast administration. *J Am Soc Echocardiogr*. 2013;26(12):1474-81.
73. Brieger D, Eagle KA, Goodman SG, Steg PG, Budaj A, White K, et al. Acute coronary syndromes without chest pain, an underdiagnosed and undertreated high-risk group: insights from the Global Registry of Acute Coronary Events. *Chest*. 2004;126(2):461-9.
74. Pope JH, Aufderheide TP, Ruthazer R, Woolard RH, Feldman JA, Beshansky JR, et al. Missed diagnoses of acute cardiac ischemia in the emergency department. *The New England journal of medicine*. 2000;342(16):1163-70.
75. Neumann J, Sørensen N, Schwemer T, et al. Diagnosis of myocardial infarction using a high-sensitivity troponin i 1-hour algorithm. *JAMA Cardiology*. 2016;1(4):397-404.
76. Sandoval Y, Apple FS, Smith SW. High-sensitivity cardiac troponin assays and unstable angina. *European Heart Journal: Acute Cardiovascular Care*. 2016;7(2):120-8.
77. Davidson BP, Kaufmann BA, Belcik JT, Xie A, Qi Y, Lindner JR. Detection of Antecedent Myocardial Ischemia With Multiselectin Molecular Imaging. *Journal of the American College of Cardiology*. 2012;60(17):1690-7.
78. Villanueva FS, Lu E, Bowry S, Kilic S, Tom E, Wang J, et al. Myocardial ischemic memory imaging with molecular echocardiography. *Circulation*. 2007;115(3):345-52.

79. Jones SP, Trocha SD, Strange MB, Granger DN, Kevil CG, Bullard DC, et al. Leukocyte and endothelial cell adhesion molecules in a chronic murine model of myocardial reperfusion injury. *American journal of physiology Heart and circulatory physiology*. 2000;279(5):H2196-201.
80. Lund LH, Edwards LB, Kucheryavaya AY, Benden C, Christie JD, Dipchand AI, et al. The registry of the International Society for Heart and Lung Transplantation: thirty-first official adult heart transplant report--2014; focus theme: retransplantation. *The Journal of heart and lung transplantation : the official publication of the International Society for Heart Transplantation*. 2014;33(10):996-1008.
81. Weller GE, Lu E, Csikari MM, Klibanov AL, Fischer D, Wagner WR, et al. Ultrasound imaging of acute cardiac transplant rejection with microbubbles targeted to intercellular adhesion molecule-1. *Circulation*. 2003;108(2):218-24.
82. Liu J, Chen Y, Wang G, Lv Q, Yang Y, Wang J, et al. Ultrasound molecular imaging of acute cardiac transplantation rejection using nanobubbles targeted to T lymphocytes. *Biomaterials*. 2018;162:200-7.
83. Steini DC, Xu L, Khanicheh E, Ellertsdottir E, Ochoa-Espinosa A, Mitterhuber M, et al. Noninvasive Contrast-Enhanced Ultrasound Molecular Imaging Detects Myocardial Inflammatory Response in Autoimmune Myocarditis. *Circ Cardiovasc Imaging*. 2016;9(8).
84. Galkina E, Ley K. Immune and Inflammatory Mechanisms of Atherosclerosis. *Annual Review of Immunology*. 2009;27(1):165-97.
85. Wu MD, Atkinson TM, Lindner JR. Platelets and von Willebrand factor in atherogenesis. *Blood*. 2017;129(11):1415-9.
86. Fernández-Ortiz A, Jiménez-Borreguero LJ, Peñalvo JL, Ordovás JM, Mocoroa A, Fernández-Friera L, et al. The Progression and Early detection of Subclinical Atherosclerosis (PESA) study: Rationale and design. *American heart journal*. 2013;166(6):990-8.
87. Blankenberg S, Zeller T, Saarela O, Havulinna AS, Kee F, Tunstall-Pedoe H, et al. Contribution of 30 biomarkers to 10-year cardiovascular risk estimation in 2 population cohorts: the MONICA, risk, genetics, archiving, and monograph (MORGAM) biomarker project. *Circulation*. 2010;121(22):2388-97.
88. Canto JG, Kiefe CI, Rogers WJ, Peterson ED, Frederick PD, French WJ, et al. Number of coronary heart disease risk factors and mortality in patients with first myocardial infarction. *JAMA*. 2011;306(19):2120-7.
89. Kaufmann BA, Carr CL, Belcik JT, Xie A, Yue Q, Chadderdon S, et al. Molecular imaging of the initial inflammatory response in atherosclerosis: implications for early detection of disease. *Arterioscler Thromb Vasc Biol*. 2010;30(1):54-9.
90. Moguillansky D, Leng X, Carson A, Lavery L, Schwartz A, Chen X, et al. Quantification of plaque neovascularization using contrast ultrasound: a histologic validation. *Eur Heart J*. 2011;32(5):646-53.
91. Liu Y, Davidson BP, Yue Q, Belcik T, Xie A, Inaba Y, et al. Molecular Imaging of Inflammation and Platelet Adhesion in Advanced Atherosclerosis
Effects of Antioxidant Therapy With NADPH Oxidase Inhibition. *Circ Cardiovasc Imaging*. 2013;6:74-82.
92. Kee PH, Kim H, Huang S, Laing ST, Moody MR, Vela D, et al. Nitric oxide pretreatment enhances atheroma component highlighting in vivo with intercellular adhesion molecule-1-targeted echogenic liposomes. *Ultrasound Med Biol*. 2014;40(6):1167-76.
93. Moccetti F, Weinkauff CC, Davidson BP, Belcik JT, Marinelli ER, Unger E, et al. Ultrasound Molecular Imaging of Atherosclerosis Using Small-Peptide Targeting Ligands Against Endothelial Markers of Inflammation and Oxidative Stress. *Ultrasound Med Biol*. 2018;44(6):1155-63.
94. Shim CY, Liu YN, Atkinson T, Xie A, Foster T, Davidson BP, et al. Molecular Imaging of Platelet-Endothelial Interactions and Endothelial von Willebrand Factor in Early and Mid-Stage Atherosclerosis. *Circ Cardiovasc Imaging*. 2015;8(7):e002765.

95. Brown E, Belcik JT, Hodovan JM, Moccetti F, Ozawa K, Bader LA, et al. Platelet-Endothelial Interactions in Atherosclerosis-Prone Arteries in a Non-Human Primate Model of Obesity and Insulin Resistance. *Vascular Discovery: From Genes to Medicine Scientific Sessions 2018*; San Francisco 2018. p. 17.
96. Khanicheh E, Mitterhuber M, Xu L, Haeuselmann SP, Kuster GM, Kaufmann BA. Noninvasive Ultrasound Molecular Imaging of the Effect of Statins on Endothelial Inflammatory Phenotype in Early Atherosclerosis. *PLoS One*. 2013;8(3).
97. Moccetti F, Brown E, Xie A, Packwood W, Qi Y, Ruggeri Z, et al. Myocardial Infarction Produces Sustained Proinflammatory Endothelial Activation in Remote Arteries. *J Am Coll Cardiol*. 2018;72(9):1015-26.
98. Lindner JR. Molecular Imaging of Thrombus: Technology in Evolution. *Circulation*. 2012;125(25):3057-9.
99. Lanza GM, Wallace KD, Scott MJ, Cacheris WP, Abendschein DR, Christy DH, et al. A novel site-targeted ultrasonic contrast agent with broad biomedical application. *Circulation*. 1996;94(12):3334-40.
100. Alonso A, Della Martina A, Stroick M, Fatar M, Griebel M, Pochon S, et al. Molecular imaging of human thrombus with novel abciximab immunobubbles and ultrasound. *Stroke*. 2007;38(5):1508-14.
101. Xie F, Lof J, Matsunaga T, Zutshi R, Porter TR. Diagnostic Ultrasound Combined with Glycoprotein 2b/3a Targeted Microbubbles Improve Microvascular Recovery Following Acute Coronary Thrombotic Occlusions. *Circulation*. 2009;119(10):1378-85.

Translational Applications of Endothelial Imaging

Summary

Endothelial imaging techniques used in combination with other cardiovascular research tools have led to several recent translational research advancements, a few of which will be discussed in the following chapters. These examples demonstrate how similar methodologies can be applied not only to different pathologies but also to different stages of the journey from basic research to clinical practice. While the pathologies addressed by each of these studies are unique, the biological pathways involved are similar and all involve activation of the endothelium to an inflamed and pro-thrombotic state characterized by release of pro-inflammatory cytokines, augmented recruitment of leukocytes, mostly monocytes and neutrophils, and a sharp increase in platelet-endothelial interactions mediated by oxidative dysregulation of VWF. These events can be triggered in a number of disease states, and similar pathways of VWF dysregulation and platelet aggregation are found in conditions such as thrombotic thrombocytopenic purpura, but the effect on the vasculature varies by setting. As such, the ability to resolve molecular and cellular interactions at the endothelial surface are of great value in understanding the mechanics of these pathways and evaluating potential therapies. Each of the following chapters will detail one study focused on these pathways. At the end of each chapter will be a summary of how the techniques used in the study were chosen in order to create a holistic picture of the cardiovascular processes in question.

Platelet-Endothelial Interactions in Early Atherosclerosis

Summary

Platelet-endothelial interactions can occur from increased oxidative stress and are thought to contribute to early atherogenesis, although most data supporting this role are from gene-modified mice. In this study, we used *in vivo* molecular imaging of the carotid endothelium to test the hypothesis that platelet-endothelial interactions occur at early stages of plaque development in

Six adult rhesus macaques fed a Western-style diet (WSD) for a median of 4 years were studied at baseline and after 8 weeks of therapy with the NOX2-inhibitor apocynin (50 mg/kg/d). Six matched lean animals were also studied. At each study, intravenous glucose tolerance test (IVGTT), body composition by DEXA, carotid intimal thickening (IMT) measurement, and contrast ultrasound molecular imaging of platelet GPIIb/IIIa and VCAM-1 of the carotid arteries bilaterally were performed.

At baseline, animals on WSD versus controls were obese (median body mass: 16.0 vs 8.7 kg, $p=0.003$; median truncal fat: 49% vs 20%, $p=0.002$), were insulin resistant (4-fold higher insulin-glucose AUC on IVGTT, $p=0.002$) with associated lipid abnormalities, and had greater carotid IMT (median: 0.26 vs 0.37 mm, $p=0.004$) with discrete plaque in 3 arteries. Obese versus lean animals had greater carotid CEU signal (median [95% CI]) for GPIIb/IIIa (10.7 [1.0-27.4] vs -0.4 [-3.1-4.3] IU, $p<0.01$) and VCAM-1 (12.0 [1.7-27.4] vs -1.9 [-6.0-0.6] IU, $p<0.01$). There was a modest but significant ($p<0.05$) correlation between carotid IMT and signal for GPIIb/IIIa and VCAM-1. Apocynin significantly reduced ($p<0.01$) signal for GPIIb/IIIa and VCAM-1 (1.3 [-1.8-4.8] and 2.9 [-2.3-13.3] IU, respectively); but did not affect IMT, body mass, or response to IVGTT.

Background

Platelet-endothelial interactions are thought to contribute to early atherogenesis.[1, 2] In pre-clinical models of atherosclerosis, this adhesion is mediated largely through interactions with endothelial-associated von Willebrand Factor (VWF) in lesion-prone arterial regions.[3-6] Adherent platelets potentially accelerate atherosclerosis by directly recruiting leukocytes, serving as a source for pro-inflammatory secreted factors and inflammasome activation, and suppressing inflammation resolution.[1, 7-10] Data implicating platelet-endothelial interactions in atherogenesis has come primarily from gene-modified mice and hyperlipidemic rabbits; and from in vitro experiments where human-derived platelets are co-incubated with vascular endothelial cells.

Obesity and insulin resistance (IR) are risk factors for atherosclerosis that produce vascular endothelial and platelet activation.[11-13] The pathways responsible for cellular activation overlap and include oxidative stress, increased cytokine production, and toxic effects of glycation and free fatty acids.[12-14] Oxidative modification in particular is known to increase endothelial-associated ultralarge VWF multimers through transcriptional regulation, mobilization of endothelial Weibel-Palade granules, and reduction in the ability of ADAMTS13 (a disintegrin and metalloproteinase with a thrombospondin type-1 motif member 13) to proteolytically cleave VWF multimers.[15-18] While obesity and IR are associated with platelet activation, whether they also increase platelet adhesion at atherosclerosis-prone sites is unknown. In this study, molecular imaging was used in rhesus macaques to test whether platelet-endothelial interactions occur in primate models of diet-induced obesity, and whether they are associated with the degree of IR, or with other markers of endothelial inflammatory activation. Because of the putative role of reactive oxygen species (ROS) in promoting excess endothelial-associated UL-VWF,[17, 18] we also investigated whether platelet adhesion occurs in concert with proteomic markers of increased oxidative stress; and whether platelet adhesion could be suppressed by apocynin, an acetovanillone that inhibits endothelial NADPH-oxidase-2 (NOX2) and has been demonstrated to reduce platelet-endothelial interactions and progression of atherosclerosis in hyperlipidemic mice.[19, 20]

Methods

Study Design

The study was approved by the Animal Care and Use Committee of the Oregon National Primate Research Center at Oregon & Science University and was performed in accordance to the guidelines of the US Department of Agriculture and Association for Assessment and Accreditation of Laboratory Animal Care concerning handling of non-human primates. We studied adult male rhesus macaques (*Macaca mulatta*) ages 6-18 years (n=6) fed a Western-style diet (WSD) (caloric content: 18.4% protein, 36.6% fat, and 45.0% carbohydrates, with 612 ppm cholesterol) for 2-6 years in order to produce obesity and insulin resistance of various degree. Obese animals were studied at baseline and after 8 weeks of therapy with oral apocynin (50mg/kg/day). Age-matched control macaques (n=6) on chow diet (14.7% calories from fat with 27 ppm cholesterol) were also studied. Each study was performed over three days and included: (a) dual x-ray absorptiometry (DEXA) assessment of central adiposity, (b) intravenous glucose tolerance testing (IVGTT), (c) carotid ultrasound imaging for plaque and intima-medial dimension, (d) carotid molecular imaging for platelet GPIIb/IIIa and vascular cell adhesion molecule-1 (VCAM-1), (e) assessment of vascular mechanical properties by pulse-wave velocity (PWV), (f) coronary microvascular flow reserve by vasodilator stress myocardial contrast echocardiography (MCE) perfusion imaging, and (g) proteomic analysis for oxidative stress. Anesthesia was induced with ketamine (10mg/kg IM) and maintained with isoflurane (1.0-1.5%) except for DEXA and IVGTT procedures for which telazolol (5mg/kg IM) was used.

Intravenous Glucose Tolerance Test

Animals were fasted overnight, after which dextrose (600mg/kg) was administered intravenously. Venous blood samples were collected prior to injection and after 1, 3, 5, 10, 20, 40, and 60 minutes. Concentrations of blood glucose and plasma insulin were measured by radioimmunoassay and plotted as time-concentration curves. Results were reported as the product of the areas under the curve (AUC) of glucose and insulin, and

as the basal HOMA-Insulin Resistance (HOMA-IR) index, calculated as follows: HOMA-IR= [fasting insulin ($\mu\text{IU/mL}$) \times fasting glucose (mmol/L)]/22.5.

Body Composition

Body composition was assessed by performing DEXA (Discovery A, Hologic Inc). Visceral adiposity was calculated by dividing truncal fat mass by total truncal mass.

Molecular Imaging Agent Preparation

Biotinylated, lipid-shelled decafluorobutane microbubbles (MB) were prepared by sonication of a gas-saturated aqueous suspension of distearoylphosphatidylcholine, polyoxyethylene-40-stearate, and distearoylphosphatidylethanolamine-PEG (2000) biotin. Microbubbles were targeted to VCAM-1 and platelet GPIIb α as previously described,[5] via surface conjugation of mouse anti-human monoclonal IgG1 against VCAM-1 (1.G11B1), or a 15 amino acid cyclic peptide (CCP-015b) based on the previously-reported OS1 peptide that binds with high affinity to primate GPIIb α (Quell Pharma Inc., Halfmoon Bay, CA).[21] Unconjugated microbubbles with no targeting ligand were used as controls. Microbubble concentration was measured by electrozone sensing (Multisizer III, Beckman-Coulter).

Validation of Platelet-targeted Contrast Agent

Because CEU molecular imaging in non-human primates has been established for VCAM-1 but not platelet GPIIb α ,[22] an *in vitro* by flow chamber assay was used to assess attachment of GPIIb α -targeted MBs to rhesus macaque platelets. Collagen-coated culture dishes were blocked with human serum albumin (2.5%) and mounted on a rectangular flow chamber. Plates were exposed to a dwell of platelet-rich plasma from HFD-fed rhesus macaques for 10 minutes and washed with PBS. Suspensions of GPIIb α -targeted and control MBs ($5 \times 10^6 \text{ mL}^{-1}$ in PBS) differentially-labeled with the lipophilic fluorophores and dioctadecyl tetramethylindocarbocyanine perchlorate (DiI) and dioctadecyloxacarbocyanine perchlorate (DiO), respectively, were drawn through the chamber at a shear stress of 1.0, 2.0 or 8.0 dyne/cm² for 5 minutes. Plates were washed with PBS at the same shear rates for 5 min after which the microbubble attachment to

adherent platelets was assessed by fluorescent microscopy in 10 randomly-selected non-overlapping optical fields (0.03 mm^2). Data were expressed as a ratio of fluorescent MB area to platelet area, and were separately analyzed for regions with: (a) single platelets or aggregates $<50 \text{ mm}^2$, or (b) platelet aggregates $>50 \text{ mm}^2$; because of the tendency of the latter to produce regional variations in shear.

CEU Molecular Imaging

Carotid CEU molecular imaging was performed bilaterally. Imaging of the distal common carotid artery and bulb was performed in long-axis using multi-pulse contrast-specific imaging at 7 MHz, a mechanical index of 1.9, a dynamic range of 55dB and a frame rate of 1 Hz (Sequoia, Siemens Medical Imaging, Mountain View, CA). Intravenous injections of 1×10^8 targeted MB agents were performed in random order. After each injection ultrasound was paused for 1 min, after which 2-D ultrasound at low-power (mechanical index <0.10) was used to locate the carotid artery before activating contrast-specific imaging for several frames. To minimize signal from freely-circulating agent, the left ventricle of the heart was simultaneously (at 1 min post-injection) exposed to high-MI (1.3) ultrasound at 1.3 MHz and a frame rate of 25-30 Hz. Signal for retained agent in each carotid was quantified by digitally averaging the first two frames acquired and subtracting several averaged frames acquired after more than 5 destructive pulse sequences. Signal from regions-of-interest drawn on the near and far walls of the distal common and proximal internal carotid were averaged.

Myocardial Perfusion Imaging

The carotid artery was imaged in long axis by 2 –D ultrasound using a linear array probe at 18 MHz (Logiq E9, GE Healthcare, Waukesha, WI). Common carotid IMT was expressed as the average of ≥ 3 far-wall measurements. Carotid plaque was defined by focal thickening of $>1 \text{ mm}$ or the presence of calcification. Pulse-wave velocity, an index of vascular stiffness was assessed by spectral pulse-wave Doppler measurement of the time delay of the onset of systolic forward velocity between the aortic arch and femoral artery, using the ECG as a time reference, divided by the distance between them. Data were averaged for 3 cardiac cycles.

Carotid Morphometry and Vascular Stiffness

The carotid artery was imaged in long axis by 2 –D ultrasound using a linear array probe at 18 MHz (Logiq E9, GE Healthcare, Waukesha, WI). Common carotid IMT was expressed as the average of ≥ 3 far-wall measurements. Carotid plaque was defined by focal thickening of >1 mm or the presence of calcification. Pulse-wave velocity, an index of vascular stiffness was assessed by spectral pulse-wave Doppler measurement of the time delay of the onset of systolic forward velocity between the aortic arch and femoral artery, using the ECG as a time reference, divided by the distance between them. Data were averaged for 3 cardiac cycles.

Myocardial Perfusion Imaging

Transthoracic MCE was performed with a phased-array probe (Sonos 5500, Philips Ultrasound, Andover, MA). MCE was performed using power modulation imaging at 1.6 MHz and a MI of 0.18 during an intravenous infusion of lipid-shelled decafluorobutane microbubbles ($1 \times 10^8 \text{ min}^{-1}$). End-systolic images were acquired after a high-power (MI 1.0) destructive pulse sequence. Imaging was performed in the apical 4- and 2-chamber views at rest and during adenosine stress (140 mg/kg/min). Post-destructive time-intensity data from two separate coronary artery territories were fit to the function:

$$y = A(1 - e^{-\beta t}) \quad (1)$$

where y is intensity at time t , A is plateau intensity representing relative microvascular blood volume, β is the microvascular flux rate, and the product of A and β is an index of myocardial blood flow.

Plasma Lipid, Cytokine and VWF Measurement

Cytokine levels from venous blood samples were determined using a monkey 29-Cytokine levels from venous blood samples were determined using a monkey 29-plex cytokine panel (ThermoFisher Scientific, Waltham, MA) following the manufacturer's instructions. Samples were analyzed on a Milliplex Analyzer (EMD Millipore, Billerica, MA) bead sorter with Xponent Software version 3.1 (Luminex, Austin, TX). Data were calculated using Milliplex Analyst software version 5.1 (EMD Millipore). Intra-assay CVs

for all analytes were <15%. Citrated venous blood samples were used to quantify circulating VWF concentration via sandwich ELISA.[23]

Blood Oxidative Markers

Proteomic markers of oxidative stress in citrated whole blood were measured, which included total and proportion reduced thiols and reduced glutathione, and presence of cysteine disulfides such as cysteine-glutathione-ss-cysteine (CG-ss-Cys) which have been recently identified as a plasma biomarker of oxidative stress.[24] Plasma samples were used to determine total cysteine, protein-bound cysteine, and cysteine-glycine. Aliquots of whole blood and plasma were snap frozen and stored at -80° C until analysis. Total protein To measure small molecular thiols and disulfides, samples were mixed 1:1 with 5 mM N-ethylmaleimide in 5 mM PBS, pH 6.0, for 30 minutes at 37° C.. For total thiols and disulfides, 20 mL samples were reduced with 80 mL of 12 mM dithiothreitol in 20 mM PBS, pH 7.4, for 20 min at 65° C. Samples were then alkylated with 40 mL of 60 mM N-ethylmaleimide in 5 mM PBS, pH 6.5, for 20 minutes at 65° C. Protein precipitation was performed with methanol (80% final v/v) for 1 hour at -20° C followed by centrifugation at 20,000 g for 20 min. The supernatant was diluted (10% v/v) in 0.01% acetic acid. LC-MS/MS analysis was performed using a Waters ACQUITY I-Class ultra-performance liquid chromatograph coupled to a SCIEX QTRAP 6500 mass spectrometer with standard electrospray ionization source. Analytes were separated using a Waters HSS T3 column at 40° C. Analysis was performed as described in on-line Supplemental Methods, and whole blood samples were normalized to hemoglobin concentration while plasma samples were normalized to total protein.

Statistical Analysis

Data were analyzed on Prism v.7.0. Depending on whether data were normally or non-normally distributed (based on the D'Agostino and Pearson omnibus test), differences between cohorts were assessed by a one-way ANOVA or Kruskal-Wallis test with Dunn's multiple comparison. Post-hoc testing was performed with a Mann Whitney U test or, for differences between baseline and post-apocynin conditions, a

Wilcoxon rank sum test. Correlations were made using linear regression and a Spearman rho test. Comparisons were considered significant at $p < 0.05$.

Results

Body Morphometry, Metabolic Status and Plasma Lipids

For animals on WSD, the median duration on the diet was 4.0 years (interquartile range [IQR]: 3.5 to 4.6 years). Compared to lean controls, animals on WSD prior to treatment with apocynin (baseline) had greater body mass and truncal adiposity on DEXA (Figure 1A and 1B). The insulin and glucose AUC product on IVGTT and HOMA-IR index showed variable degrees of IR in the obese animals on WSD (Figure 1C and 1D). Obese animals also had significantly elevated baseline plasma total cholesterol, LDL cholesterol, and triglycerides (Figure 1E to 1H). Treatment of obese animals with 8 weeks of apocynin did not significantly alter the body mass, truncal fat, degree of IR, or lipid status.

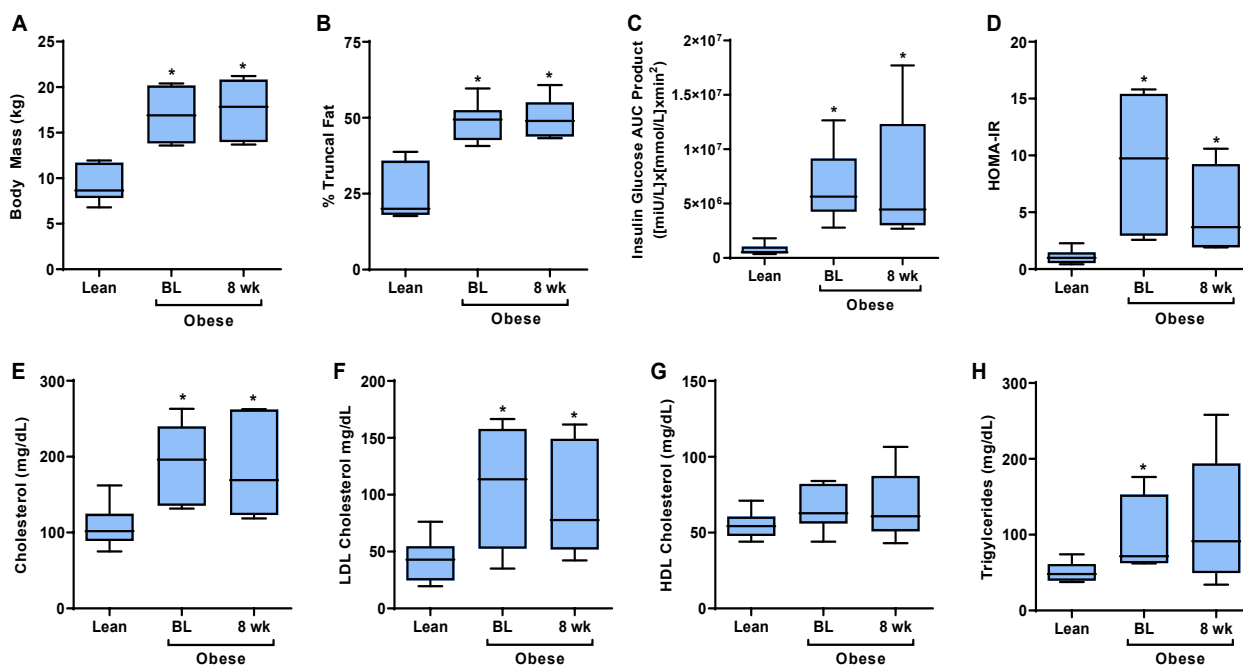


Figure 1: Indices of metabolic status in lean rhesus macaques, and obese animals on WSD at baseline (BL) and after 8 weeks of apocynin treatment. Bar-whisker plots illustrate the median (bar), interquartile range (box) and range (whiskers) for (A) body mass, (B) truncal fat on DEXA, (C) product of insulin and

glucose area-under-the-curve (AUC) on IVGTT, (D) HOMA-IR index, (E) serum cholesterol, (F) LDL cholesterol, (G) HDL cholesterol, and (H) serum triglyceride. * $p < 0.05$ vs lean.

Blood Markers of Oxidative Stress

When compared to lean controls, obese animals on WSD had evidence of increased oxidative stress evidenced by lower levels of reduced blood thiols and a lower proportion of thiols in a reduced state (Figure 2A-C). Glutathione was by far the most abundant thiol (>85% of total thiols). Both reduced blood glutathione and proportion of glutathione in a reduced state were lower in obese animals. Plasma CG-ss-Cys, along with other cysteine disulfides, has been shown to be a sensitive marker of oxidative stress,[24] and tended to be higher in obese animals (Figure 2H), though this difference did not reach statistical significance. Plasma concentrations of 8-series F₂-isoprostane were also higher in HFD-treated animals therapy (Figure 2I). Cumulatively, these results indicate greater oxidative status in NHPs on WSD. Statistical power for detecting changes in oxidative stress after apocynin treatment was limited by hemolysis in several samples. Yet apocynin was found to result in significant increases in the proportion of reduced thiols (median 0.50 [IQR 0.46 to 0.54] vs 0.56 [IQR 0.53 to 0.59], $p=0.03$) and the proportion of reduced glutathione (median 0.49 [IQR 0.45 to 0.52] vs 0.55 [IQR 0.52 to 0.58], $p=0.03$).

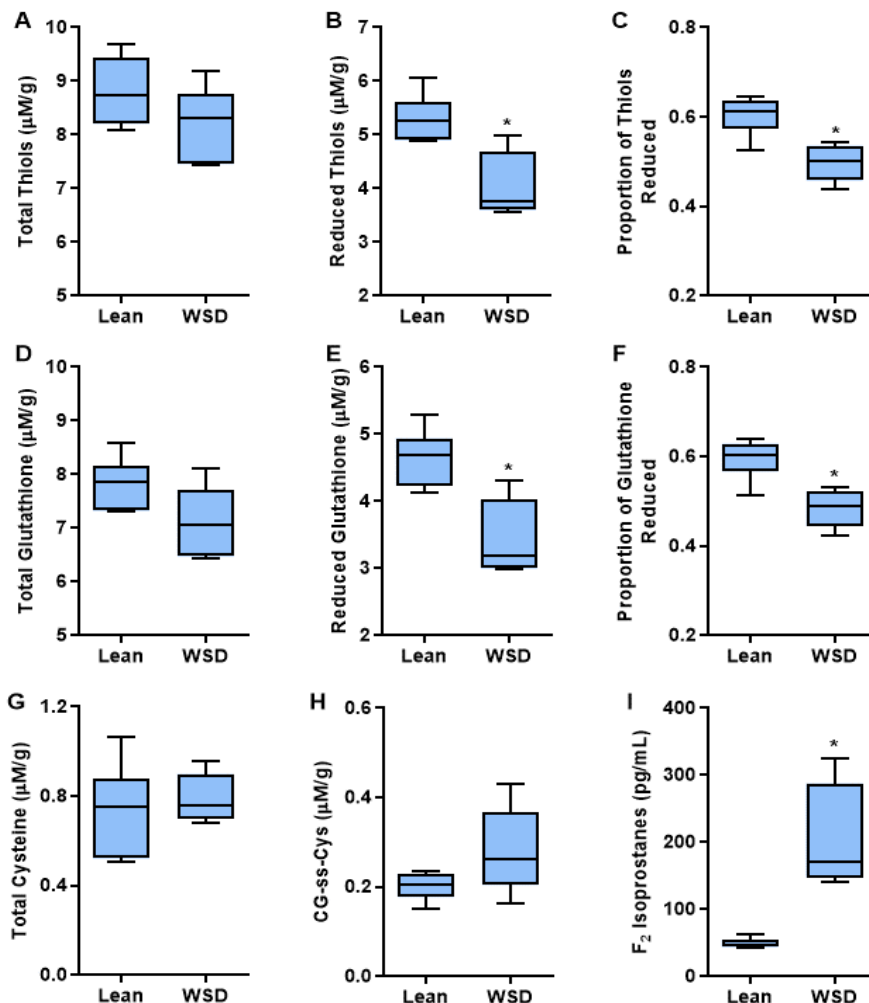


Figure 2: Blood proteomic markers of oxidative stress which include: (A) total thiol concentration in whole blood normalized to hemoglobin, (B) reduced thiols, (C) proportion of thiols in a reduced state, (D) total glutathione concentration normalized to hemoglobin, (E) reduced glutathione, (F) proportion of glutathione in a reduced state, (G) plasma cysteine concentration normalized to total protein, and (H) plasma GS-ss-Cys disulfide concentration. Plasma F₂-isoprostane concentrations by ELISA are also shown (I). *p<0.05 vs lean controls.

Vascular Morphology and Function

There were no significant group-wise or stage-wise differences in heart rate, systolic or diastolic blood pressure. Carotid IMT was greater in obese animals on WSD than lean controls (Figure 3). Three obese animals had evidence for mild discrete plaque in one common or external carotid artery. There were no group-wise differences in aortic

stiffness on PWV. In obese animals, neither carotid IMT nor PWV were significantly changed by 8 weeks of apocynin treatment.

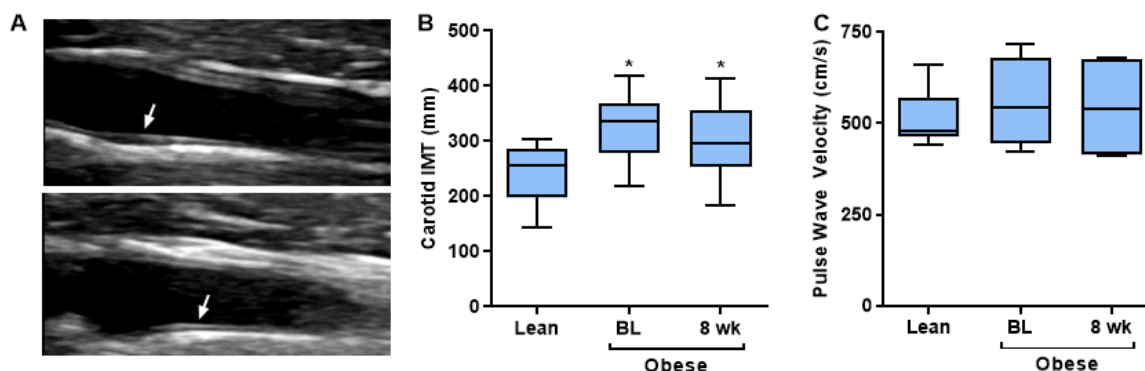


Figure 3: Vascular morphology and functional analysis in lean rhesus macaques, and obese animals on WSD at baseline (*BL*) and after 8 weeks of apocynin treatment. **(A)** Example of intima-media thickness (IMT) measurement from the common carotid artery (*top*) and carotid bulb (*bottom*). Bar-whisker plots illustrate the median (bar), interquartile range (box) and range (whiskers) for **(B)** carotid IMT, and **(C)** pulse wave velocity. * $p < 0.05$ vs lean.

MCE perfusion imaging at rest and during adenosine was performed to assess coronary microvascular response, abnormalities of which are often associated with impaired endothelial function and oxidative stress. A significant group-wise difference was found for microvascular flux rate (b-value) during adenosine stress (Table 1). Although post-hoc analysis between groups for all measurements did not meet statistical significance after correcting for multiple comparisons, there were consistent trends towards lower resting and hyperemic values for microvascular flux rate (b-value), blood flow, b-reserve, and flow reserve in obese animals versus lean controls. Treatment of obese animals with apocynin also tended to produce higher hyperemic microvascular flux rate and perfusion, and greater b-reserve and flow reserve. Vital signs at rest and during stress were similar between groups.

Carotid Molecular Imaging

In vitro flow chamber studies were used to assess binding of GPIIb/IIIa-targeted MB to platelets from rhesus macaques. Platelet-targeted MBs selectively attached to single platelets and platelet aggregates, whereas attachment for non-targeted control agent was rare (Figure 4A and 4B). Shear-dependency of attachment was observed for

attachment to single platelets or small platelet aggregates. Shear-dependency was not found for large aggregates, likely because of the potential of large aggregates to interrupt laminar flow and create regions of marked shear heterogeneity along the aggregate surface.

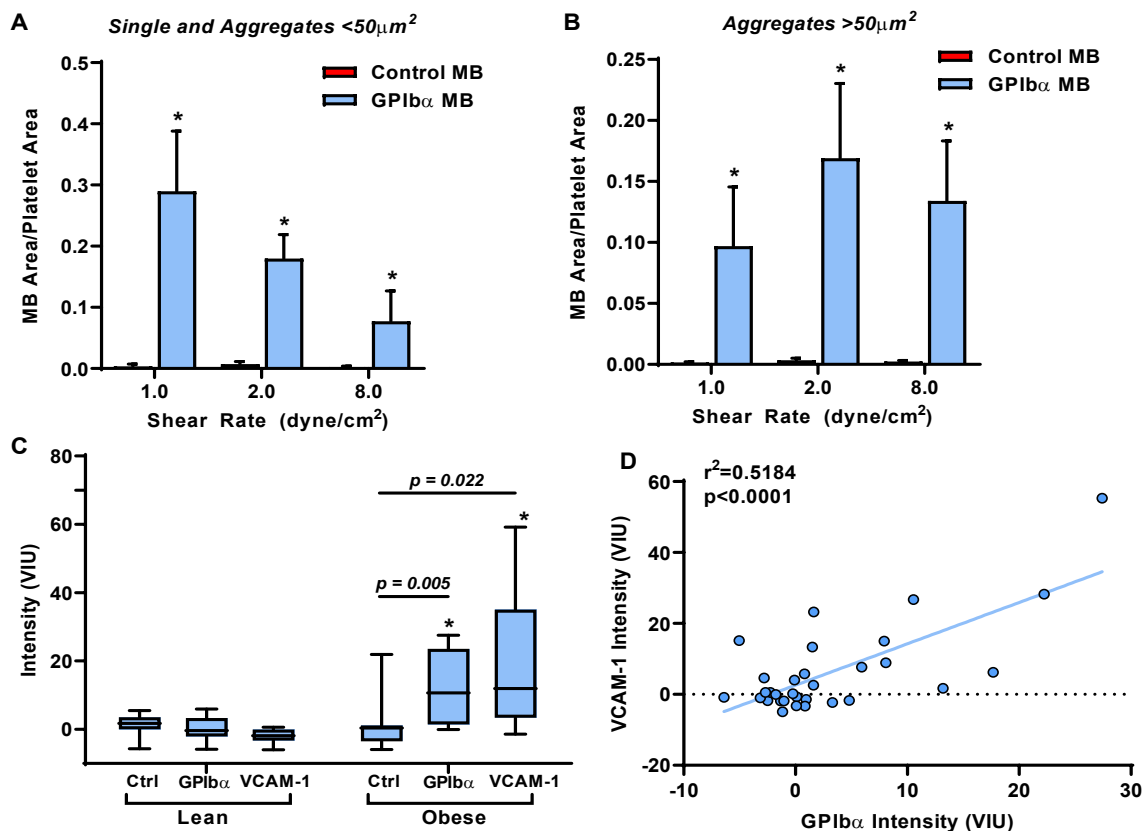


Figure 4: In vitro flow chamber data (shear rates of 1.0 to 8.0 dyne/cm²) for attachment of control and GPIb α -targeted microbubbles (MB) for (A) single platelets and small platelet aggregates (<math><50\mu\text{m}^2</math>), and for (B) large platelet aggregates (>math>>50\mu\text{m}^2</math>). Data are quantified as mean (\pm SEM) fluorescent area normalized to platelet area * $p<0.05$ vs control MB. (C) Bar-whisker plots illustrating the median (bar), interquartile range (box) and range (whiskers) for CEU molecular imaging for control (Ctrl) and targeted MB agents in lean and obese animals. VIU, video intensity units. * $p<0.05$ versus lean. (D) Correlation between VCAM-1 and GPIb α signal on CEU molecular imaging on a per-artery basis.

On CEU molecular imaging of the carotid arteries for platelet GPIb α at the arterial surface and for endothelial VCAM-1, a marker of inflammatory activation, signal was low in lean control animals and similar to that from control agent (Figure 4C). In animals on WSD, signal for both VCAM-1 and platelet GPIb α were elevated compared to non-targeted agent, and higher than that from lean control animals. Signal for platelet GPIb α showed a modest correlation with VCAM-1 within the same carotid arteries (Figure 4D).

There was no morphologic evidence for carotid thrombus formation at the sites of platelet signal enhancement. Neither platelet GPIb α nor VCAM-1 signal on CEU were found to be closely correlated with body mass, truncal adiposity, time on WSD, or degree of IR on IVGTT (Table 2); although a modest but significant relationship was found between GPIb α signal and body mass and adiposity. Carotid IMT was found to have a modest but significant correlation with signal for both platelet GPIb α and VCAM-1 signal (Table 2, Figure 5).

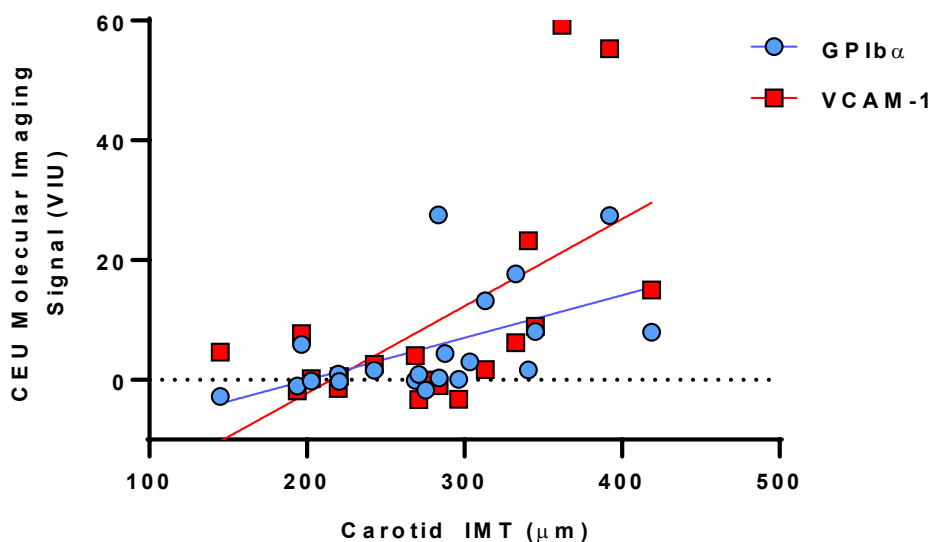


Figure 5: Correlation between common carotid average IMT and CEU-derived molecular imaging signal for GPIb α or VCAM-1.

Table 2. Correlation of Morphometric and Metabolic Data With Molecular Imaging

	GPIba Signal		VCAM-1 Signal	
	r ²	p-value	r ²	p-value
Body mass	0.25	0.02	0.06	0.29
Truncal adiposity	0.31	<0.01	0.11	0.16
Time on WSD*	0.18	0.22	0.26	0.14
IVGTT AUC Product	0.16	0.07	0.15	0.09
Carotid IMT	0.29	0.01	0.35	<0.01

*Analysis performed for obese animals only. AUC, insulin-glucose area-under-the-curve; IMT, intima-medial thickness; IVGTT, intravenous glucose tolerance test; WSD, Western-style diet.

In obese animals, eight weeks of therapy with apocynin significantly reduced the carotid molecular imaging signal for platelet GPIb α and VCAM-1, whereas no significant change was observed for the control agent signal (Figure 5). Arteries with the highest GPIb α or VCAM-1 signal at baseline had the greatest relative decrease in signal after therapy. A limited array of plasma cytokines that could be obtained from NHP plasma did not show any major group-wise differences between lean and obese animals except a non-significant trend toward higher CCL-2 concentrations ($p=0.067$). Apocynin had no major effect on cytokine concentration in obese animals (Figure 6). Plasma VWF antigen levels were higher in obese versus lean animals; but did not significantly change with apocynin treatment. These data indicate that groupwise differences in endothelial phenotypes on molecular imaging were not necessarily reflected by groupwise differences in circulating pro-inflammatory cytokines.

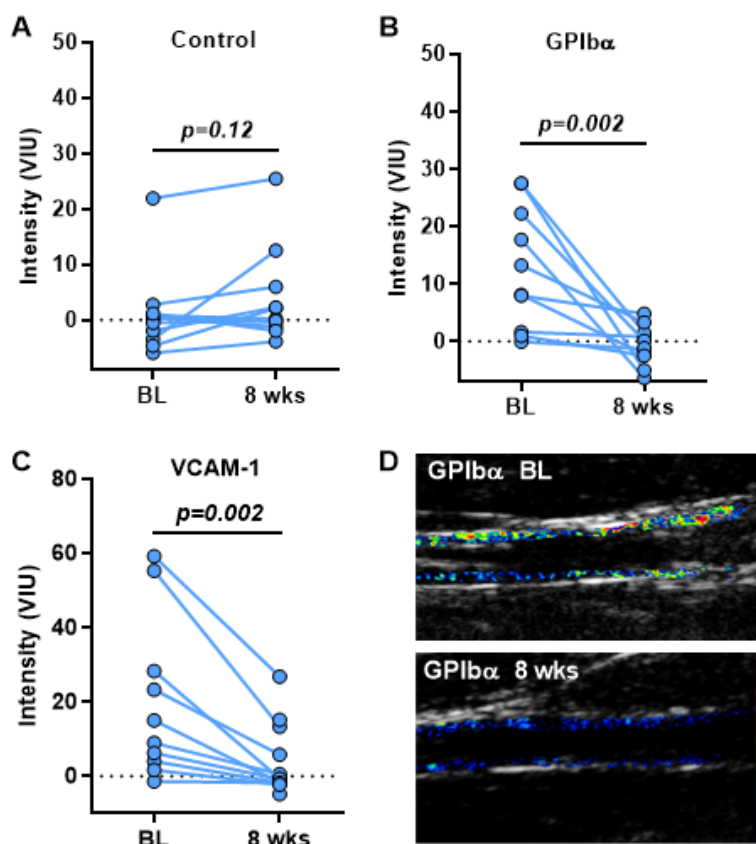


Figure 6: Individual data for CEU molecular imaging signal in obese animals at baseline (BL) and after 8 weeks of apocynin therapy for: (A) control MB, (B) GPIb α -targeted MB, and (C) VCAM-1-targeted MB. (D) Example carotid artery CEU molecular imaging of platelet GPIb α from an obese animal at baseline

and after apocynin therapy. Images show background-subtracted and color-coded (scale at right) CEU signal superimposed on a co-registered two-dimensional B-mode image.

phenotypes on molecular imaging were not necessarily reflected by groupwise differences in circulating pro-inflammatory cytokines.

animals on HFD, signal for VCAM-1 and platelet GPIIb/IIIa were elevated compared to chow-fed controls, and significantly higher than for control, non-targeted contrast agent. Signal for platelet GPIIb/IIIa showed a modest correlation with VCAM-1 within the same carotid arteries. There was no morphologic evidence for carotid thrombus formation at the sites of platelet signal enhancement. Neither platelet GPIIb/IIIa nor VCAM-1 signal on CEU were found to be closely correlated with body mass, truncal adiposity, time on WSD, or degree of IR on IVGTT (Table 2); although a modest but significant relationship was found between GPIIb/IIIa signal and body mass and adiposity. Carotid IMT was found to have a modest but significant correlation with signal for both platelet GPIIb/IIIa and VCAM-1 signal (Table 2).

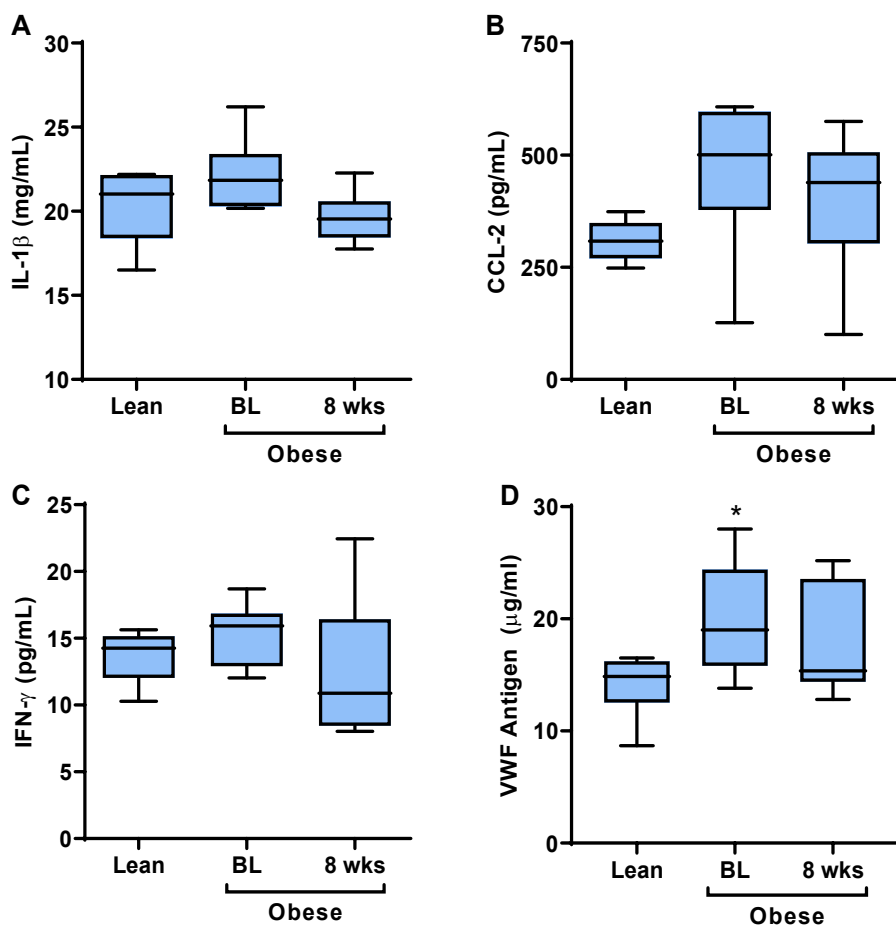


Figure 7: Bar-whisker plots illustrate the median (bar), interquartile range (box) and range (whiskers) for plasma (A) IL- α , (B) CCL-2, (C) interferon gamma (*IFN- γ*), and (D) von Willebrand Factor (VWF) antigen. * $p < 0.05$ vs lean.

In obese animals, eight weeks of therapy with apocynin therapy significantly reduced molecular imaging signal for carotid artery molecular imaging signal for platelet GPIIb/IIIa and VCAM-1, while no significant change was observed with respect to control agent signal (Figure 5). Arteries with the highest GPIIb/IIIa or VCAM-1 signal at baseline had the greatest relative decrease in signal after therapy. A limited array of plasma cytokines did not show any major group-wise differences between lean and obese animals except a non-significant trend toward higher CCL-2 concentrations ($p = 0.067$); nor were there any major differences between baseline and post-apocynin treatment in obese animals (Figure 7). Plasma VWF antigen levels were higher in obese versus lean animals; but did not significantly change with apocynin treatment.

Discussion

The critical role platelets play in acute atherothrombotic events in patients with late state atherosclerotic disease is well established. It is increasingly recognized that platelet adhesion can promote atherosclerotic early plaque development and progression through multiple pathways.[1, 2, 10, 25] An important component of “thromboinflammation” in plaque development is the ability for platelets to influence the local balance of pro-inflammatory cytokines, ROS, and inflammasome activation status. An obstacle to studying pro-atherogenic effects of platelets is the lack of methods for assessing adhesion *in vivo* in animal models that closely resemble humans. In this study, noninvasive ultrasound molecular imaging with targeted probes confined to the vascular compartment was used to examine carotid endothelial-platelet adhesion in NHPs with diet-induced obesity and IR. Our results indicate that (a) platelet adhesion occurs in atherosclerosis-prone arteries of obese rhesus macaques before significant plaque development; (b) the degree of platelet adhesion is independent of the degree of IR or obesity; (c) there is an association between the degree of platelet adhesion and other markers of endothelial activation such as VCAM-1 expression, and (d) inhibition of NOX2 with apocynin reduces both platelet adhesion and VCAM-1 expression without major changes in metabolic function or plasma cytokine levels.

Atherosclerosis is a disease that, in most individuals, becomes clinically evident decades after disease initiation. Important insights into the pathobiology of plaque progression has been provided through gene-modified mice. Yet, our understanding of human atherosclerosis must also rely on models where the temporal course, spatial distribution, and biologic pathways are similar to those in humans. We employed an NHP model where adult rhesus macaques were fed a diet moderately high in saturated fat and cholesterol for an average of four years in order to study vascular changes that occur as a result of obesity and IR. Similar to what occurs in humans, the severity of IR and lipid derangement varied substantially between individual animals. Despite the wide variation in metabolic response that occurs with this model,[26] *in vivo* imaging has previously demonstrated a relatively uniform time-dependent increase in endothelial VCAM-1, endothelial selectin expression, and IMT for two years after starting WSD.[22] These data indicate that endothelial inflammatory responses are influenced by diet-induced obesity, but are not tightly coupled to the degree of IR. Neither platelet-endothelial interactions nor the oxidative pathways that can promote these interactions have been studied previously.

Platelet-endothelial interactions, primarily through interaction of GPIIb/IIIa and endothelial-associated VWF, have been shown in small animal models to promote atherogenesis.[3-6] Characterization of these interactions in human-like models of obesity and insulin resistance is important to study for several reasons. Increased oxidative stress and certain lipid derangements associated with metabolic disease are known to interfere with ADAMTS13-mediated cleavage of endothelial VWF.[17, 18, 23] In small clinical trials of patients with diabetes, low ADAMTS13 activity has been associated with increased rates of cardiovascular events.[27] Yet plasma levels of VWF are higher in patients with diabetes or high-risk metabolic syndrome,[28, 29] and are known to progressively increase after initiating WSD in NHPs.[22] In aggregate, these data suggest that IR may be associated with increased endothelial VWF production or mobilization, and reduced ability to proteolytically cleave endothelial-associated ultralarge VWF multimers.

For the current study, platelet adhesion was imaged by using targeted MBs that are similar to platelets in their size distribution and that bear a cyclic peptide that binds to constitutively-expressed platelet GPIIb/IIIa in primates.[21] CEU signal from this agent in the carotid artery was significantly increased in NHPs that had diet-induced obesity, IR,

dyslipidemia. These obese animals also had evidence of early atherosclerotic changes in the form of increased IMT on carotid ultrasound, and evidence for endothelial dysfunction on coronary microvascular vasodilator testing. The molecular imaging signal for platelet adhesion did not correlate closely with the degree of obesity or IR, indicating that simply the presence and not the degree of metabolic derangement determines platelet adhesion. Because of the multiple pathways by which platelets can activate the endothelium through cytokines, growth factors, chemokines, and ROS;[25] CEU was also used to examine endothelial VCAM-1 expression which correlated with the degree of platelet signal. The idea that platelet adhesion had a deterministic role in VCAM-1 expression is supported by studies in atherosclerotic mice where endothelial expression of VCAM-1 has been shown to be influenced by manipulation of ADAMTS13 activity and GPIb α -mediated platelet adhesion (unpublished data).

The generation of ROS is likely to be a common pathway linking endothelial dysfunction, VWF-mediated platelet adhesion, and diet-induced obesity or IR. Oxidative pathways have been shown to be enhanced in patients with diabetes mellitus;[12] including oxidative modification specifically of VWF.[30] In our studies, oxidative proteomics and F₂-isoprostanes from blood indicated elevated oxidative stress in animals on WSD. The effects of apocynin, a plant-derived α -methoxyphenol that inhibits cytosolic assembly of NOX2 subunits,[19] was investigated based on several lines of reasoning. Murine studies have revealed a critical role of the NOX2 isoform in atherosclerosis.[31] Moreover, apocynin has been shown to reverse oxidative endothelial abnormalities attributable to hyperglycemia,[32] and also to reduce not only atherosclerosis progression but also endothelial platelet adhesion in mice.[20] This latter finding is congruent with the notion that ROS can stimulate endothelial secretion of VWF,[16] and render VWF less susceptible to proteolysis.[17] Apocynin was found to reduce carotid artery CEU signal for platelet GPIb α and VCAM-1, and to improve microvascular function in general in obese animals. This effect was independent of any major changes in the degree of obesity, IR, lipid status, or cytokine levels.

There are several important limitations of this study that should be considered. The number of animals studied was low based on the resources needed to produce NHP models of sustained IR produced by WSD for several years. The extensive profiling of these animals allowed us to derive as much information as possible from this valuable

resource. While CEU molecular imaging provides an *in vivo* assessment of endothelial phenotype, histologic validation of the technique has been performed in mice, not primates. Instead, we relied on flow chamber assays for *ex vivo* validation of MB adhesion in shear. We are, however, reassured by previous studies showing time-dependent increase in CEU signal for endothelial inflammatory activation after starting WSD;[22] and by our current findings that CEU signal correlated with carotid IMT. The premise for this study is that platelets contribute vascular inflammatory activation at an early stage of disease. While our study is the first to show platelet adhesion in a human-like model of obesity and IR, we did not conclusively demonstrate causative relationship between platelet adhesion, VCAM-1, and IMT. Finally, when considering the role of oxidative stress, we were neither powered nor have the tools to determine the quantitative relationship between ROS generation and platelet adhesion.

In summary, our findings indicate that platelet-endothelial interactions occur in a NHP model of diet-induced obesity and IR, and are found at early stages of atherosclerotic intimal-medial thickening in the carotid artery. The degree of platelet adhesion correlates with the degree of VCAM-1 expression, supporting but not proving the hypothesis that platelet adhesion contributes to endothelial inflammatory activation. Treatment of animals with NOX2-inhibitor apocynin, significantly reduced carotid platelet adhesion and VCAM-1 expression without altering metabolic status. Whether this approach can suppress plaque formation will require studies with longer duration of therapy. Based on our results, we believe that further investigation of strategies to reduce platelet-endothelial interaction are warranted using human relevant models.

Summary of Techniques

The primary innovation of this study was the use of CEU molecular imaging to measure platelet-endothelial interactions in primates. While we were unable to perform further studies beyond flow chamber analysis to validate the platelet-targeted CEU agent developed for this study, we previously validated a similar agent in murine models of atherosclerosis using histological analysis and intravital microscopy.

While this study was primarily concerned with vascular biology, it was nevertheless important to take a holistic view of the pathophysiology of early atherosclerosis in order to fully understand how different processes interact. Unlike the case studies in Chapter 6 and 7, this study did not involve major cardiac or vascular dysfunction. However, use of MCE and PWV were necessary to contextualize our findings to a specific stage in disease progression. The major finding of this study is that platelet-endothelial interactions can be found at the earliest stages of disease, before endothelial dysfunction becomes severe enough to impair blood flow. While there was a trend towards decreased coronary microvascular flux rate during adenosine stress, our findings neither met statistical significance nor correlated with CEU molecular imaging signal for platelet adhesion and VCAM-1 expression. Similar findings showing no correlation between metabolic markers and platelet and VCAM molecular imaging signal suggests that early endothelial activation and platelet-endothelial interactions cannot be inferred from measures of metabolic disorder or vascular function. The holistic approach in this study, which drew on a wide array of metabolic, vascular, and cardiac techniques, provided preliminary evidence that oxidative stress, endothelial inflammation and platelet recruitment are more closely linked than other pathways driving early atherosclerosis, and that there is significant heterogeneity between subjects in their vascular response to diet-induced insulin resistance and obesity.

References

1. Wu MD, Atkinson TM, Lindner JR. Platelets and von Willebrand factor in atherogenesis. *Blood*. 2017;129(11):1415-9.
2. Nording HM, Seizer P, Langer HF. Platelets in inflammation and atherogenesis. *Front Immunol*. 2015;6:98.
3. Theilmeier G, Michiels C, Spaepen E, Vreys I, Collen D, Vermylen J, et al. Endothelial von Willebrand factor recruits platelets to atherosclerosis-prone sites in response to hypercholesterolemia. *Blood*. 2002;99(12):4486-93.
4. Massberg S, Brand K, Gruner S, Page S, Muller E, Muller I, et al. A critical role of platelet adhesion in the initiation of atherosclerotic lesion formation. *J Exp Med*. 2002;196(7):887-96.
5. Shim CY, Liu YN, Atkinson T, Xie A, Foster T, Davidson BP, et al. Molecular Imaging of Platelet-Endothelial Interactions and Endothelial von Willebrand Factor in Early and Mid-Stage Atherosclerosis. *Circ Cardiovasc Imaging*. 2015;8(7):e002765.
6. Moccetti F, Brown E, Xie A, Packwood W, Qi Y, Ruggeri Z, et al. Myocardial Infarction Produces Sustained Proinflammatory Endothelial Activation in Remote Arteries. *J Am Coll Cardiol*. 2018;72(9):1015-26.

7. Weyrich AS, Lindemann S, Zimmerman GA. The evolving role of platelets in inflammation. *J Thromb Haemost.* 2003;1(9):1897-905.
8. Barrett TJ, Schlegel M, Zhou F, Gorenchtein M, Bolstorff J, Moore KJ, et al. Platelet regulation of myeloid suppressor of cytokine signaling 3 accelerates atherosclerosis. *Sci Transl Med.* 2019;11(517).
9. Gerdes N, Seijkens T, Lievens D, Kuijpers MJ, Winkels H, Projahn D, et al. Platelet CD40 Exacerbates Atherosclerosis by Transcellular Activation of Endothelial Cells and Leukocytes. *Arterioscler Thromb Vasc Biol.* 2016;36(3):482-90.
10. Rolfes V, Ribeiro LS, Hawwari I, Bottcher L, Rosero N, Maasewerd S, et al. Platelets Fuel the Inflammasome Activation of Innate Immune Cells. *Cell Rep.* 2020;31(6):107615.
11. Santilli F, Vazzana N, Liani R, Guagnano MT, Davi G. Platelet activation in obesity and metabolic syndrome. *Obes Rev.* 2012;13(1):27-42.
12. Vazzana N, Ranalli P, Cucurullo C, Davi G. Diabetes mellitus and thrombosis. *Thromb Res.* 2012;129(3):371-7.
13. Ormazabal V, Nair S, Elfeky O, Aguayo C, Salomon C, Zuniga FA. Association between insulin resistance and the development of cardiovascular disease. *Cardiovasc Diabetol.* 2018;17(1):122.
14. Schleicher E, Friess U. Oxidative stress, AGE, and atherosclerosis. *Kidney Int Suppl.* 2007(106):S17-26.
15. Xiang Y, Hwa J. Regulation of VWF expression, and secretion in health and disease. *Curr Opin Hematol.* 2016;23(3):288-93.
16. Vischer UM, Jornot L, Wollheim CB, Theler JM. Reactive oxygen intermediates induce regulated secretion of von Willebrand factor from cultured human vascular endothelial cells. *Blood.* 1995;85(11):3164-72.
17. Chen J, Fu X, Wang Y, Ling M, McMullen B, Kulman J, et al. Oxidative modification of von Willebrand factor by neutrophil oxidants inhibits its cleavage by ADAMTS13. *Blood.* 2010;115(3):706-12.
18. Wang Y, Chen J, Ling M, Lopez JA, Chung DW, Fu X. Hypochlorous acid generated by neutrophils inactivates ADAMTS13: an oxidative mechanism for regulating ADAMTS13 proteolytic activity during inflammation. *J Biol Chem.* 2015;290(3):1422-31.
19. Yu J, Weiwer M, Linhardt RJ, Dordick JS. The role of the methoxyphenol apocynin, a vascular NADPH oxidase inhibitor, as a chemopreventative agent in the potential treatment of cardiovascular diseases. *Curr Vasc Pharmacol.* 2008;6(3):204-17.
20. Liu Y, Davidson BP, Yue Q, Belcik T, Xie A, Inaba Y, et al. Molecular imaging of inflammation and platelet adhesion in advanced atherosclerosis effects of antioxidant therapy with NADPH oxidase inhibition. *Circ Cardiovasc Imaging.* 2013;6(1):74-82.
21. Benard SA, Smith TM, Cunningham K, Jacob J, DeSilva T, Lin L, et al. Identification of peptide antagonists to glycoprotein Ibalph that selectively inhibit von Willebrand factor dependent platelet aggregation. *Biochemistry.* 2008;47(16):4674-82.
22. Chadderdon SM, Belcik JT, Bader L, Kirigiti MA, Peters DM, Kievit P, et al. Proinflammatory endothelial activation detected by molecular imaging in obese nonhuman primates coincides with onset of insulin resistance and progressively increases with duration of insulin resistance. *Circulation.* 2014;129(4):471-8.
23. Chung DW, Chen J, Ling M, Fu X, Blevins T, Parsons S, et al. High-density lipoprotein modulates thrombosis by preventing von Willebrand factor self-association and subsequent platelet adhesion. *Blood.* 2016;127(5):637-45.

24. Fu X, Cate SA, Dominguez M, Osborn W, Ozpolat T, Konkle BA, et al. Cysteine Disulfides (Cys-ss-X) as Sensitive Plasma Biomarkers of Oxidative Stress. *Sci Rep.* 2019;9(1):115.
25. Gawaz M, Langer H, May AE. Platelets in inflammation and atherogenesis. *J Clin Invest.* 2005;115(12):3378-84.
26. Chadderdon SM, Belcik JT, Bader L, Peters DM, Kievit P, Alkayed NJ, et al. Temporal Changes in Skeletal Muscle Capillary Responses and Endothelial-Derived Vasodilators in Obesity-Related Insulin Resistance. *Diabetes.* 2016;65(8):2249-57.
27. Rurali E, Noris M, Chianca A, Donadelli R, Banterla F, Galbusera M, et al. ADAMTS13 predicts renal and cardiovascular events in type 2 diabetic patients and response to therapy. *Diabetes.* 2013;62(10):3599-609.
28. Meigs JB, O'Donnell C J, Tofler GH, Benjamin EJ, Fox CS, Lipinska I, et al. Hemostatic markers of endothelial dysfunction and risk of incident type 2 diabetes: the Framingham Offspring Study. *Diabetes.* 2006;55(2):530-7.
29. Seligman BG, Biolo A, Polanczyk CA, Gross JL, Clausell N. Increased plasma levels of endothelin 1 and von Willebrand factor in patients with type 2 diabetes and dyslipidemia. *Diabetes Care.* 2000;23(9):1395-400.
30. Taye A, Saad AH, Kumar AH, Morawietz H. Effect of apocynin on NADPH oxidase-mediated oxidative stress-LOX-1-eNOS pathway in human endothelial cells exposed to high glucose. *Eur J Pharmacol.* 2010;627(1-3):42-8.
31. Barry-Lane PA, Patterson C, van der Merwe M, Hu Z, Holland SM, Yeh ET, et al. p47phox is required for atherosclerotic lesion progression in ApoE(-/-) mice. *J Clin Invest.* 2001;108(10):1513-22.
32. Oggianu L, Lancellotti S, Pitocco D, Zaccardi F, Rizzo P, Martini F, et al. The oxidative modification of von Willebrand factor is associated with thrombotic angiopathies in diabetes mellitus. *PLoS One.* 2013;8(1):e55396.

Remote Endothelial Activation Following Myocardial Ischemia

Summary

In the months after acute MI, risk for acute atherothrombotic events in non-culprit arteries increases several-fold. We hypothesized that sustained pro-inflammatory and pro-thrombotic endothelial alterations occur in remote vessels after MI. We studied wild type mice, atherosclerotic mice with double knockout (DKO) of the LDL receptor and Apobec-1, and DKO mice treated with the Nox-inhibitor apocynin were studied at baseline and 3 and 21 days after closed-chest MI. Ultrasound molecular imaging of P-selectin, VCAM-1, von Willebrand factor (VWF) A1-domain, and platelet GPIIb/IIIa was performed. Intravital microscopy was used to characterize post-MI leukocyte and platelet recruitment in the remote microcirculation after MI.

Aortic molecular imaging for P-selectin, VCAM-1, VWF-A1, and platelets was increased several fold ($p < 0.01$) three days post-MI for both wild-type and DKO mice. At 21 days, these changes resolved in wild-type mice but persisted in DKO mice. Signal for platelet adhesion was abolished 1 hour after administration of ADAMTS13 which regulates VWF multimerization. In DKO and wild-type mice, apocynin significantly attenuated the post-MI increase for molecular targets, and platelet depletion significantly reduced P-selectin and VCAM-1 signal. On intravital microscopy, MI resulted in remote vessel leukocyte adhesion and platelet string or net complexes. On histology, high-risk inflammatory features in aortic plaque increased in DKO mice 21 days post-MI which were completely prevented by apocynin.

Acute MI stimulates a spectrum of changes in remote vessels including upregulation of endothelial inflammatory adhesion molecules, and platelet-endothelial

adhesion from endothelial-associated VWF multimers. These remote arterial alterations persist longer in the presence of hyperlipidemia, are associated with accelerated plaque growth and inflammation, and are attenuated by Nox inhibition.

Introduction

Major acute atherothrombotic events such as myocardial infarction (MI), stroke, or limb ischemia lead to a markedly increased risk for recurrent events in separate vascular territories. After MI, the risk for stroke or recurrent MI from non-culprit lesions is increased by several-fold over the ensuing six to twelve months (1–3). These findings indicate that a focal ischemic event can lead to systemic adverse vascular responses. Murine studies have demonstrated that acute MI triggers the splenic production and mobilization of inflammatory Ly-6C^{high} monocytes, and the accelerated entry of these cells and other CD11b+ myeloid cells into remote arterial plaque for weeks after the initial event (4). With regards to remote vascular endothelial responses, MI in mice leads to upregulation of mRNA for endothelial cell adhesion molecules within the non-infarct myocardial microcirculation (5). However, little is known about endothelial-specific alterations in remote arterial atherosclerotic lesions, including in non-coronary locations.

In this study, *in vivo* imaging methods unique in their ability to investigate events at the endothelial-blood pool interface were used to study post-MI endothelial alterations in remote arteries that can predispose to accelerated plaque growth and atherothrombotic events. Contrast-enhanced ultrasound (CEU) molecular imaging and direct microvascular observation with intravital microscopy were used to characterize the endothelial responses that occur in remote arteries after MI. CEU molecular imaging with targeted microbubble contrast agents that are confined to the vascular compartment was selected based on extensive experience in murine and non-human primate models to detect arterial events that occur at the endothelial-blood pool interface (6–8). Specifically, we hypothesized that acute MI leads to (i) remote arterial upregulation of endothelial cell adhesion molecules on the plaque surface, and (ii) platelet adhesion to the intact endothelial surface which contributes to pro-inflammatory activation and can occur, in part, from abnormal endothelial-associated ultra-large self-

associated multimers of von Willbrand factor (VWF) which occur secondary to dysregulation of normal proteolytic regulation by ADAMTS13 (a disintegrin and metalloprotease with thrombospondin type I repeats-13) (9–11).

Methods

Animal Model

The study was approved by the Animal Care and Use Committee of the Oregon Health & Science University. We studied wild-type C57Bl/6 mice and mice with susceptibility to age-related atherosclerosis through dual gene-targeted deletion or “double knockout” (DKO) of the LDL-receptor and apolipoprotein-B mRNA editing enzyme catalytic polypeptide 1 (ApoBec-1) on a C57Bl/6 background. DKO mice develop reproducible, age-dependent development of atherosclerosis on a chow diet (6,12), and were studied at 20–25 weeks of age when plaque size is modest with early intraluminal encroachment (6). For all studies, mice were anesthetized with 1.0–2.0% inhaled isoflurane and a jugular cannula was placed for intravenous injection of contrast agents or drugs.

Imaging Study Design

The proximal thoracic aorta was selected as a remote arterial site to study endothelial activation after MI. CEU molecular imaging of the aorta was performed using microbubble contrast agents targeted to P-selectin (MB_P), vascular cell adhesion molecule-1 (VCAM-1) (MB_V), GPIIb α as an indicator of platelet adhesion (MB_{PII}), and endothelial VWF (MB_{VWF}). Studies were also performed with control non-targeted microbubbles (MB). Animals were studied in the following experimental conditions:

- i. Molecular imaging performed at baseline and at either 3 or 21 days after MI in wild-type and DKO mice. Mice were also studied 3 days after sham procedure.
- ii. Molecular imaging was performed 3 days after MI in DKO mice treated 1 hour prior to imaging with recombinant human ADAMTS13 (5 μ g I.V.), the key regulatory protease which reduces VWF multimer size through cleavage at the VWF A2 domain (10,11).

- iii. Molecular imaging performed 3 and 21 days after MI in DKO mice treated with apocynin (50 mg/kg/d) starting on the day of MI. Apocynin (acetovanillone) is a potent inhibitor of NADPH-oxidase (Nox) which has been implicated in transcriptional upregulation of adhesion molecule expression, and has been demonstrated to reduce platelet-endothelial adhesion in early and late atherosclerosis (13,14).
- iv. Molecular imaging was performed 21 days after MI in DKO mice undergoing platelet depletion by I.V. injection of 2 µg/g rat anti-mouse GPIIb/IIIa mAb (7) at days 1, 4, 9 and 15 post-MI to determine the contribution of platelets to sustained endothelial adhesion molecule expression.

Myocardial Infarction

A closed-chest model of MI was used to allow for the resolution of the acute inflammatory responses after thoracotomy and cardiac exposure. At least five days prior to scheduled MI, mice were anesthetized, intubated, and placed on positive pressure mechanical ventilation with weight-adjusted tidal volumes and respiratory rates. A limited left lateral thoracotomy was performed to expose only the basal anterior wall. A 6-0 prolene suture was placed under the LAD but left unsecured. The free ends of the suture were exteriorized through the chest wall and left in a subcutaneous location after closure. After 5–7 days, mice were anesthetized, the suture was exteriorized through a limited skin incision and the tension was placed on the suture for 40 min to produce ST-elevation on ECG monitoring and wall motion abnormalities on high-frequency transthoracic 2-D echocardiography (Vevo 2100, Visualsonics Inc., Toronto, Canada). Sham-treated animals received a suture without tightening.

Targeted Microbubble Preparation

Biotinylated lipid-shelled decafluorobutane microbubbles were prepared by sonication of a gas-saturated aqueous suspension of distearoylphosphatidylcholine (2 mg/mL), polyoxyethylene-40-stearate (1 mg/mL), and distearoylphosphatidylethanolamine-PEG(2000)biotin (0.4 mg/mL). Conjugation of biotinylated ligand to the microbubble surface was performed with biotin-streptavidin

bridging as previously described.(15) Ligands used for targeting were: dimeric murine recombinant A1 domain of VWF A1 (mature VWF amino acids 445 to 716) for targeting platelet GPIIb α for MB_{Pt}, a cell-derived peptide representing the N-terminal 300 amino acids of GPIIb α for MB_{VWF},(7) and monoclonal antibodies against the extracellular domain of either P-selectin (RB40.34, BD Biosciences), or VCAM-1 (clone 429, BD Biosciences) for MB_P and MB_V, respectively. Control MB were prepared with isotype control antibody (R3-34, BD Biosciences). Microbubble concentrations and size distributions were measured by electrozone sensing (Multisizer III, Beckman Coulter).

Imaging Protocols

Contrast-enhanced ultrasound (CEU) molecular imaging of the ascending aorta and proximal aortic arch were imaged using a right parasternal window with a linear-array probe (Sequoia, Siemens Medical Systems). Multi-pulse phase-inversion and amplitude-modulation imaging at 7 MHz was performed with a dynamic range of 55 dB and a mechanical index of 1.0. Gain was set at a level that just eliminated pre-contrast background speckle and kept constant for all studies. Images were acquired 8 min after intravenous injection of targeted or control microbubbles (1×10^6), performed in random order, in order to allow almost all free microbubbles to clear from blood pool. Signal from retained microbubbles alone was determined as previously described by acquiring the first ultrasound frame and then digitally subtracting several averaged frames obtained after complete destruction of microbubbles at a mechanical index of 1.4 to eliminate signal from the low concentration of freely-circulating microbubbles in the blood pool (15). Signal intensity was measured from a region-of-interest encompassing the entire ascending aorta to just beyond the origin of the brachiocephalic artery. Region selection was facilitated by fundamental 2-D imaging at 14 MHz acquired after each CEU imaging sequence.

Echocardiography

High-frequency (40 MHz) transthoracic echocardiography was performed at each post-MI study interval in DKO mice to evaluate any differences in left ventricular (LV) diameter, infarct size, stroke volume, or peak aortic shear rate related to treatment with

apocynin. A parasternal long-axis and parasternal short-axis at the mid-ventricular level imaging planes were used to assess infarct size quantified by calculating a wall motion score index. LV dimensions at end-systole and end-diastole were measured from the parasternal long-axis view using linear measurements of the LV at the level of the mitral leaflet tips during diastole. Stroke volume was calculated as the product of the left ventricular outflow tract cross-sectional area and time-velocity integral on pulsed-wave Doppler. Longitudinal strain was calculated using speckle-tracking echocardiography from a parasternal long-axis view and was quantified as the average of a standard **single 6-segment model**.

Histology

Histology of the aortic root and the mid-ascending aorta for DKO mice was performed 21 days or 3 months after MI (randomized evenly for each group). Perfusion-fixed transaxial sections were stained with Masson's trichrome for assessment of plaque area and collagen content. Immunohistochemistry was performed with antibody against Mac-2 (M3/38, eBioscience) to assess macrophage content, against CD41 (sc20234, Santa Cruz Biotechnology, Santa Cruz CA) for platelets; and for VCAM-1 (BS-0369r, Bioss Inc Atlanta, GA). For each epitope, secondary staining was performed with species-appropriate secondary antibodies labeled with ALEXAFluor-488, -555, or -594 (Invitrogen Grand Island, NY). Plaque collagen content, necrotic core and MAC-2 area are expressed as percent of plaque area.

Intravital Microscopy

Direct observation of post-MI potentiation of platelet- and leukocyte-endothelial interactions was performed with intravital microscopy in wild-type and DKO mice, with or without MI 3 days prior to study. Mice were anesthetized with ketamine and xylazine (I.P.) and the cremaster muscle was exteriorized and prepared for intravital microscopy as previously described (16). Microscopy was performed with combined fluorescent epi-illumination and low-intensity transillumination (Axioskop2-FS, Carl Zeiss, Inc) and digital recordings were made with a high-resolution CCD camera (C2400, Hamamatsu Photonics). In vivo fluorescent labeling of platelets was performed with rhodamine-6G (1

mg/mL, 75 μ L I.V.). The number of adherent leukocytes and platelet adhesive events (>5 s), and the formation of platelet “strings” indicative of ultra-large VWF multimers were quantified as fluorescent platelet area normalized to vessel area. Rolling velocity of leukocytes in 15–35 μ m post-capillary venules was calculated by the distance traveled by video calipers divided by time.

Statistical Analysis

Data analysis was performed with Prism v7.0a (Graph Pad, La Jolla, California). Continuous variables that were normally distributed are displayed as mean \pm SD unless stated otherwise; whereas those that were not normally distributed are displayed as box-whisker plots with a bar representing median, box representing 25–75% quartiles, and whiskers representing range. Student *t* test (paired or unpaired) were performed for comparisons of normally distributed data. For non-normally distributed data, either a Mann-Whitney *U* test or Wilcoxon signed-rank test was used as appropriate according to experimental conditions (group-wise comparisons versus paired data within a group). For multiple comparisons, a one-way ANOVA was performed for normally distributed data with post-hoc testing with Holm-Sidak’s multiple comparisons correction. A Kruskal-Wallis test followed by Dunn’s multiple comparison test was performed for non-normally distributed data.

Results

Post-MI Ventricular Function and Aortic Shear

Electrocardiographic ST-segment elevation and regional hypokinesia or akinesia involving the mid to distal anterior, anterolateral, and anteroseptal walls on echocardiography was observed in all mice at the time of closed-chest LAD ischemia, but were not seen in any of the animals undergoing sham surgical procedure. Myocardial infarction resulted in LV enlargement, reduction of LV systolic function and stroke volume, and lower peak aortic shear rate at day 3 and 21 (Figure 1). Chronic therapy with apocynin starting on the day of MI did not affect the infarct-related changes in LV dimension or function on echocardiography, or the aortic peak shear rate.

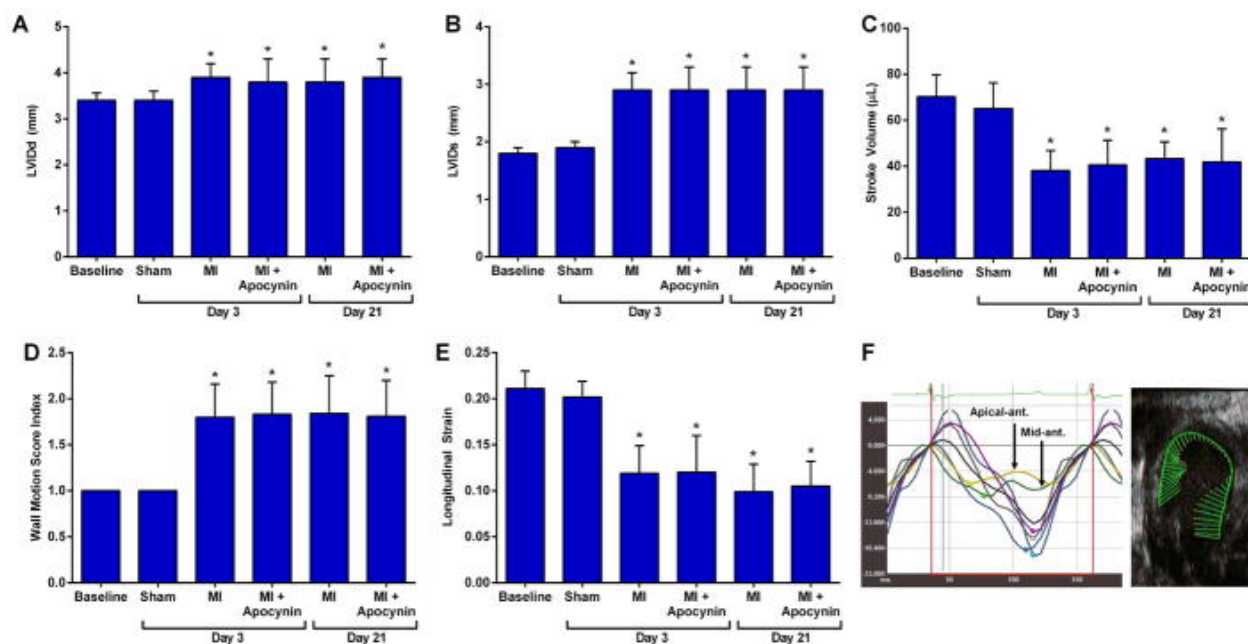


Figure 1: Mean (\pm SD) values are shown for LV internal diameter at **(A)** end-diastole and **(B)** end-systole, **(C)** stroke volume, **(D)** wall motion score index, and **(E)** longitudinal strain. Data are combined for wild-type and DKO mice which were not significantly different from each other. * $p < 0.05$ versus baseline. **(F)** Example of LV strain curves from a long-axis view illustrating severe hypokineses in the LAD territory at day 3 post-MI and corresponding vector mapping of endocardial strain.

Remote Arterial Endothelial Activation and Platelet Adhesion After MI

At baseline prior to any procedures, molecular imaging signal enhancement of the thoracic aorta for endothelial P-selectin, VCAM-1, Von Willebrand factor (VWF) A1-domain, and platelet GPIIb/IIIa were all found to be higher in DKO than wild-type mice (Figure 2A), consistent with greater aortic endothelial adhesion molecule expression, endothelial-associated active form of VWF, and platelet adhesion in DKO mice. In DKO but not wild-type mice, signal for all four targeted microbubble agents was significantly greater than for control microbubbles. At day 3 post-MI, signal for endothelial P-selectin, VCAM-1, VWF and platelet GPIIb/IIIa all increased significantly in both wild-type and DKO mice (Figure 2B to 2D). In wild-type mice, the post-MI increase for all four targeted agents completely resolved and returned to baseline levels at day 21; whereas in DKO mice signal enhancement remained elevated at 21 days. Signal from control MBs was low in all mice and did not change significantly after MI. Sham procedure did not produce any changes on CEU molecular imaging (Figure 2E).

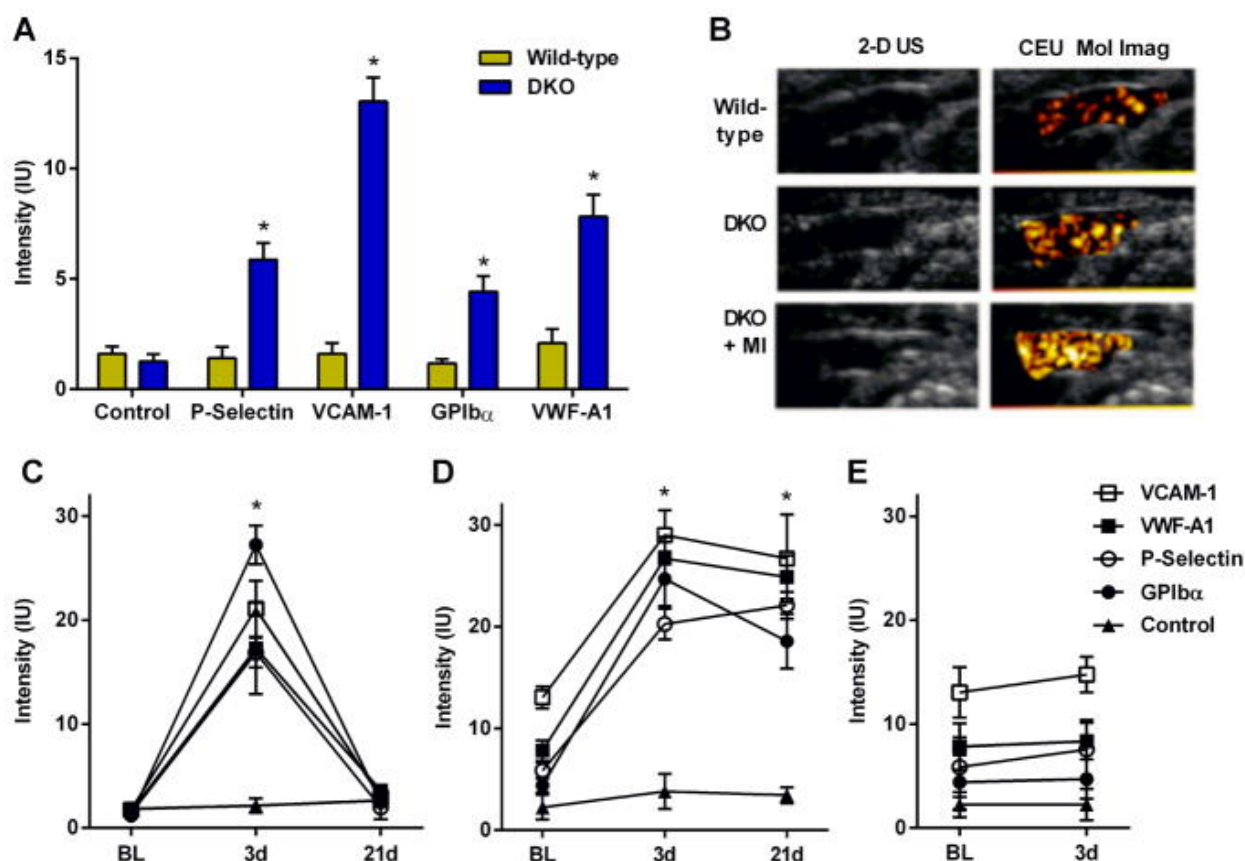


Figure 2: Background-subtracted signal intensity (mean \pm SEM) on (A) CEU molecular imaging of the thoracic aorta from wild-type and DKO mice. * p <0.05 vs control non-targeted signal. (B) Examples of 2-D ultrasound and CEU molecular imaging for VCAM-1 of the thoracic aorta of wild-type, DKO, and post-MI (day 3) DKO mice. (C–E) Mean (\pm SEM) signal intensity on CEU molecular imaging of the aorta from: (C) post-MI wild-type mice; (D) post-MI DKO mice; and (E) DKO mice undergoing sham surgery. * p <0.05 for all actively-targeted agents vs baseline values and vs control non-targeted signal.

Effect of ADAMTS13 on Platelet Adhesion

In DKO mice, aortic CEU molecular imaging 3 days post-MI was performed before and 1 hour after treatment with recombinant ADAMTS13, a protease that removes endothelial-associated VWF and controls VWF size (10,17). ADAMTS13 abolished platelet GPIb α signal (Figure 3A), indicating that platelet adhesion in remote vessels after MI occurs secondary to inducible abnormalities in the enzymatic regulation of endothelial-associated VWF. The lack of effect on P-selectin signal confirmed that this signal was primarily endothelial rather than platelet in origin.

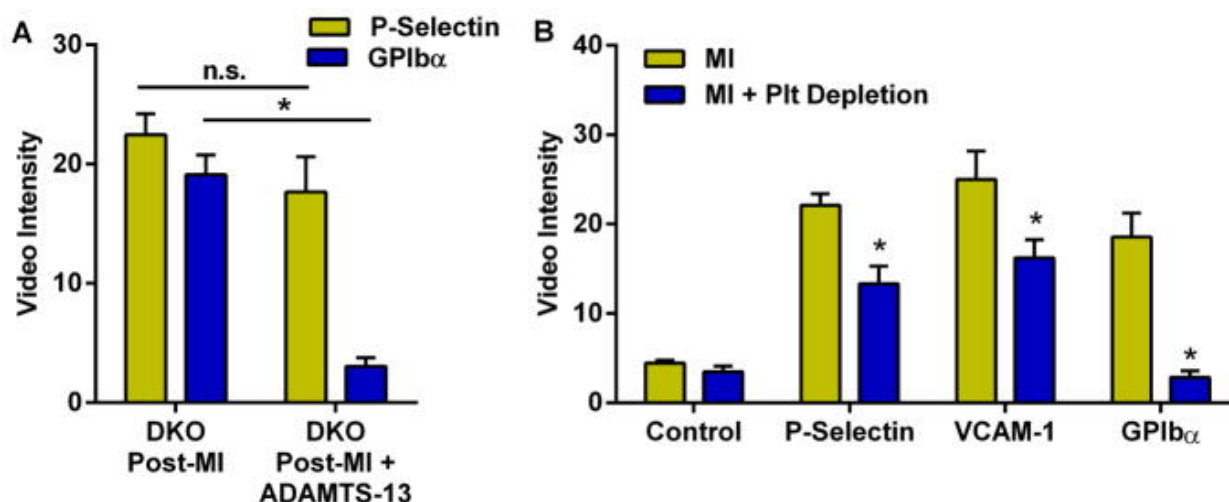


Figure 3: (A) CEU molecular imaging intensity for P-selectin and platelet GPIb α in DKO mice at day 3 post-MI before and 1 hour after ADAMTS-13 (5 μ g, I.V.). **(B)** Aortic molecular imaging signal in DKO mice with and without platelet depletion at 21 days post-MI. * p <0.05 vs non-treated.

Effect of Platelet Depletion on Endothelial Activation

In DKO mice studied at day 21, platelet immune-depletion started on day 1 after MI completely prevented the post-MI increase in platelet adhesion on aortic molecular imaging, and also significantly but modestly reduced endothelial P-selectin and VCAM-1 signal enhancement (Figure 3B).

Nox Inhibition Reduced Endothelial Activation and Platelet Adhesion

Apocynin started on the day of MI significantly attenuated the post-MI increase in remote aortic molecular imaging signal for P-selectin, VCAM-1, platelet GPIb α , and VWF A-1 in wild-type mice at day 3 and in DKO mice at day 3 and 21 (Figure 4A to 4C).

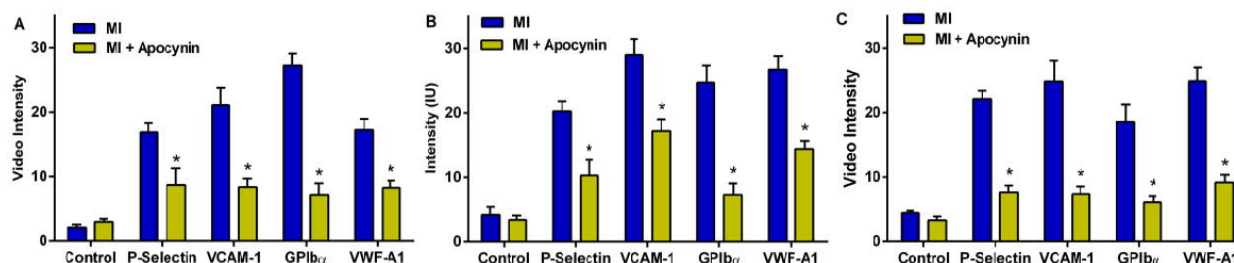


Figure 4: Mean (\pm SEM) signal intensity on quantitative CEU molecular imaging depicting effect of apocynin in: **(A)** wild-type mice 3 days post-MI; **(B)** DKO mice 3 days post-MI; and **(C)** DKO mice 21 days post-MI. * p <0.05 vs non-treated.

Remote Endothelial Activation in the Microcirculation

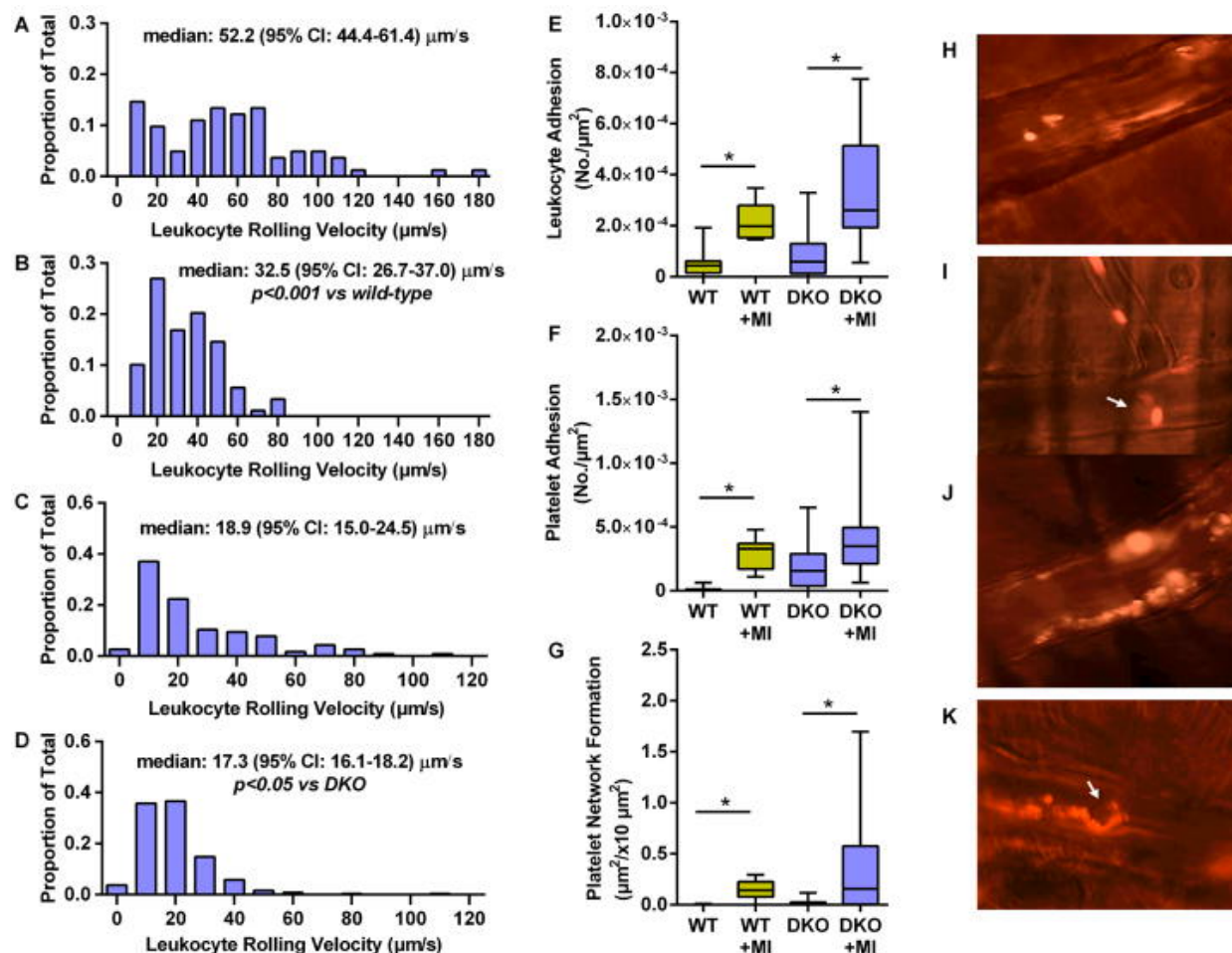


Figure 5: Histograms and median leukocyte rolling velocities in cremasteric venules are shown for (A) wild-type mice, (B) wild-type mice 3 days post-MI, (C) DKO mice, and (D) DKO mice 3 days post-MI. Box-whisker plots depict (E) leukocyte adhesion (number per vessel area); (F) isolated platelet adhesion; and (G) platelet string or net complex formation rate on venules. * $p < 0.001$; † $p < 0.0001$. Pseudocolored intravital microscopy images illustrate rhodamine-6G-labeled platelets adhering in post-capillary venules in the form of: (H), individual platelets; (I), single platelet-leukocyte complex; (J), large platelet net complexes on the endothelium; and (K), platelet strings attached (downstream) to adherent leukocytes. Arrow=leukocytes.

Intravital microscopy of the cremaster muscle was used to interrogate for similar post-MI remote endothelial-related events in the microcirculation. Venular leukocyte rolling velocity in both wild-type and DKO mice decreased after MI (Figure 5A to 5D, Online Videos). Leukocyte firm adhesion in venules and platelet adhesion were also significantly increased 3 days post-MI in both wild-type and DKO mice (Figure 5E to 5G). Almost all platelet adhesion events in non-ischemic mice were in the form of single

platelets or small linear aggregates, whereas platelet adhesion post-MI was in the form of large string or net assemblies, consistent with ultra-large multimers of VWF on the endothelium or anchored to adherent leukocyte-platelet hetero-aggregates (Figure 5H to 5K, Online Videos).

Post-MI Acceleration of Plaque Progression is Suppressed with Nox-2 Inhibition

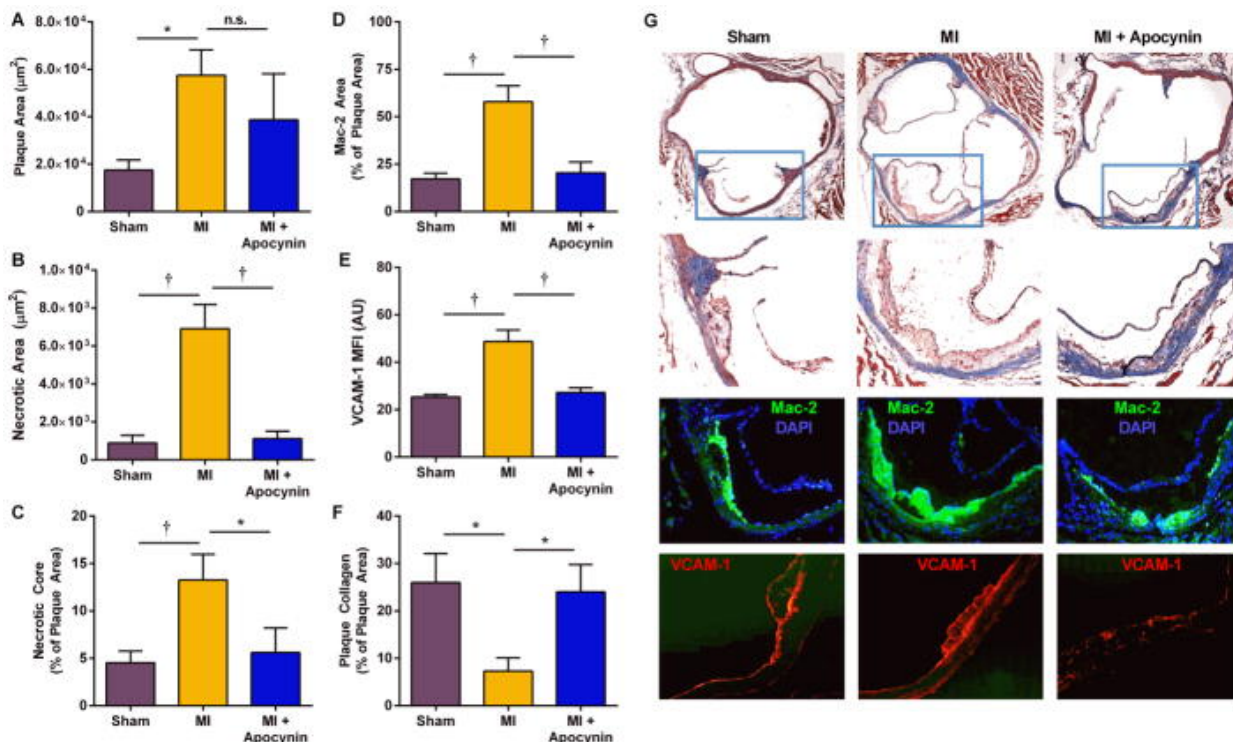


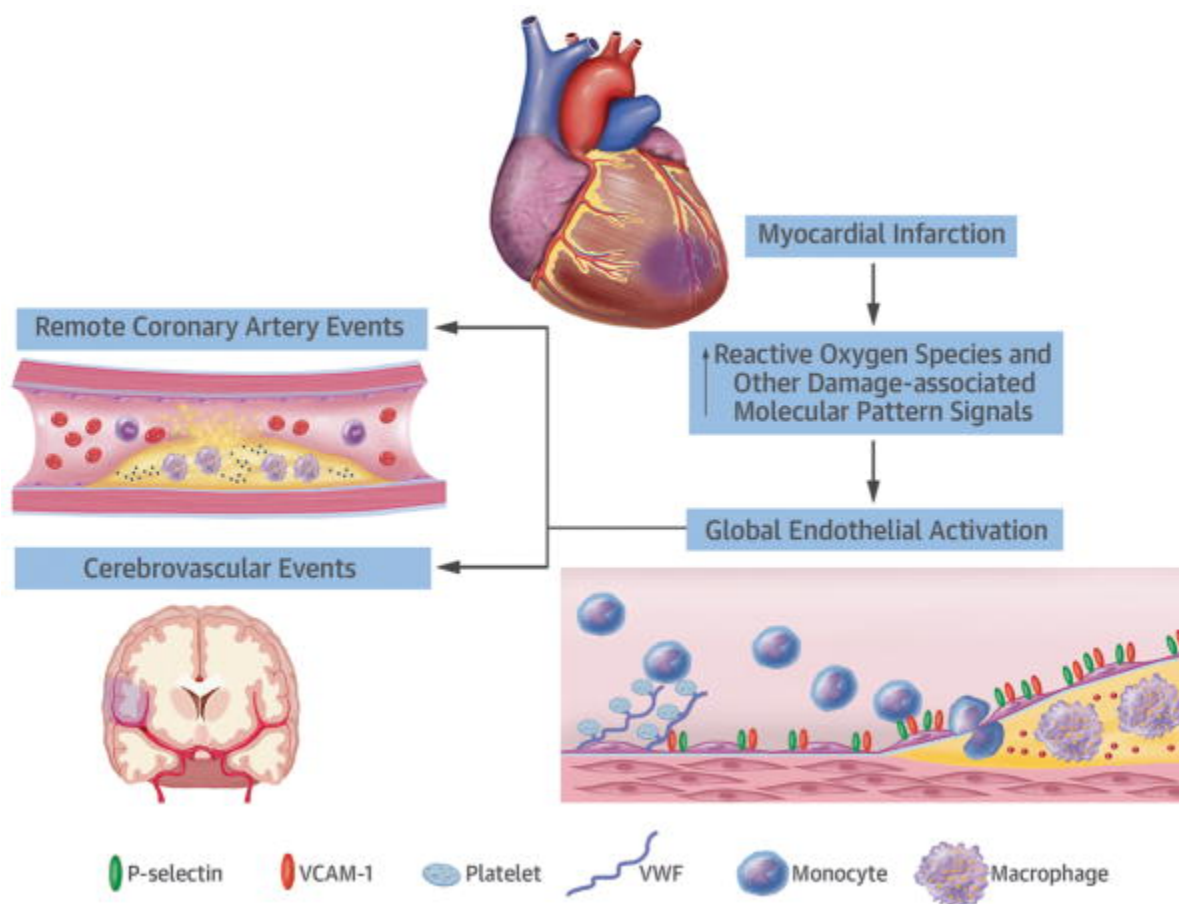
Figure 6: Data are from DKO mice at 21 days after sham procedure or after MI, with or without apocynin treatment. **(A)** plaque cross-sectional area averaged for the aortic sinuses and distal ascending aorta; **(B)**, necrotic core area; **(C)**, necrotic core area as a percentage of total plaque area; **(D)**, Mac-2 area averaged for plaques in the aortic sinuses and distal ascending aorta; **(E)**, VCAM-1 staining area; and, **(F)** plaque collagen content as a percentage of the total plaque area. * $p < 0.05$; † $p < 0.01$ **(J)** Examples of histology with Masson's trichrome, and immunohistochemistry for Mac-2 and VCAM-1 from DKO mice 21 days after either sham procedure or MI with or without apocynin treatment.

Aortic histology demonstrated that at 21 days, DKO mice undergoing MI compared to sham-treated mice had larger plaque area, larger necrotic core area, increased macrophage content, greater VCAM-1 staining, and lower collagen content (Figure 6). The increase in VCAM-1 staining was present in endothelium overlying atherosclerotic plaques, as well as non-plaque endothelium. Apocynin therapy in post-MI DKO mice attenuate all of the high-risk features in terms of macrophage content,

VCAM-1 staining and collagen content; whereas the reduction in plaque size did not reach statistical significance. Histology obtained at 3 months demonstrated persistently larger plaque size and macrophage content, and lower collagen content in DKO mice undergoing MI compared with sham-treated controls.

Discussion

Our results indicate that acute MI stimulates a spectrum of adverse events in remote arterial and microvascular beds including endothelial upregulation of VCAM-1 and P-selectin, and platelet adhesion that occurs through primarily through VWF that is either endothelial-associated or from adherent leukocyte-platelet complexes (Central Illustration). These adverse changes at the vascular endothelial surface persist longer when there is pre-existing atherosclerosis and hyperlipidemia, and are associated with acceleration of plaque growth and inflammation in arteries spatially remote from the MI. Our data also suggest that reduction of oxidative stress through Nox inhibition attenuates adverse endothelial responses in remote arteries.



Central Illustration: Myocardial infarction triggers systemic effects, including an increase in reactive oxygen species (ROS) and other damage-associated molecular patterns (DAMPs). These molecular intermediates result in endothelial activation including upregulation of adhesion molecules for inflammatory cells, increase in endothelial associated VWF, and secondary platelet adhesion. The pro-inflammatory and pro-thrombotic endothelial changes found in our experiments are changes could be associated with increased risk for atherothrombotic events in humans.

There is increasing evidence that global inflammatory responses after a major acute ischemic event contribute to the heightened risk for events in remote arterial beds. Leukocytosis and elevated plasma levels of cytokines and chemokines commonly occurs in the subacute phase after MI, the degree of which is associated with intermediate-term prognosis (18–20). In studies performed in atherosclerotic mice, acute MI has been shown to lead to an increase of pro-inflammatory Ly-6C^{high} monocytes and other myeloid cells (4). Carotid activity with 18F-fluorodeoxyglucose positron emission tomography has been shown to be higher in patients with recent acute MI than those with chronic stable angina (21), although cross-sectional design precluded any comments on causation. Little is known regarding

endothelial changes that promote the recruitment of innate immune cells into atherosclerotic lesions in distant vessels after MI.

We applied CEU molecular imaging with targeted tracers confined to the vascular compartment to reveal that reperfused MI triggers remote arterial upregulation of endothelial cell adhesion molecules that are critical for the recruitment of inflammatory cells (9,22). Although our primary aim was to study events in large arteries, corroborative evidence in other vascular territories was provided by intravital microscopy of a non-coronary microvascular bed where leukocyte rolling velocity and adhesion were used as indicators of endothelial expression of selectins and integrin counter-receptors. These studies confirmed that MI promotes global endothelial activation. We believe that endothelial activation was in part responsible for the acceleration of plaque growth, inflammation, and necrotic core at 21 days and 3 months post-MI; all consistent with a more “high risk” plaque appearance on histology. However, it is possible that increased plaque macrophage content contributed to the persistence of the endothelial activation at day 21 in DKO mice, consistent with the feed-forward nature of plaque inflammation.

Our investigation of endothelial-platelet adhesion after MI is based on the mounting evidence that these interactions play a multifactorial role in plaque inflammatory status (9,23). Local release of platelet-derived pro-inflammatory cytokines and CD40L leads to monocyte activation, upregulation of endothelial adhesion molecules, formation of neutrophil extracellular traps (NETs); and the generation of reactive oxygen species (ROS) (9,23–25). Inhibition of platelet activation or adhesion has been shown in animal models to reduce plaque size and inflammation (26,27).

Platelet adhesion in early to moderate-stage atherosclerosis is primarily mediated by interactions between the GPIIb α component of the GPIIb/IX/V complex on platelets and the A1 domain of “activated” VWF (27–29). This interaction appears to be facilitated by association of VWF with the intact endothelial surface, and ineffective cleavage at the A2 domain by ADAMTS13, resulting in ultra-large multimers of self-associated VWF (17,29,30). In this study, molecular imaging of a remote artery revealed a large increase in endothelial VWF-A1 domain and platelet adhesion after MI which

paralleled endothelial inflammatory responses. Platelet signal in post-MI DKO mice was entirely eliminated by exogenous ADAMTS13 implicating abnormal regulation of VWF. Again, intravital microscopy provided corroborative evidence such as the formation of large linear platelet clusters that were dynamic in size and oscillated in flow, characteristic of the large VWF networks. To a lesser degree, adherent platelet-monocyte complexes were also observed. Many of these hetero-aggregates did not appear consistent with direct contact of single platelets to the leukocyte surface, but instead appeared as a dynamic clustering of platelets downstream from leukocytes possibly consistent with VWF net formation on leukocytes (31). The contribution of platelets to post-MI endothelial activation in this study was confirmed by a reduction, but not elimination, of P-selectin and VCAM-1 signal at 21 days in platelet-depleted DKO mice.

Oxidative stress measured by a variety of biomarkers is known to increase after recent MI (32), is known to be greater in the setting of dyslipidemia (33), and represents a pathway by which inflammation and platelet adhesion can self-propagate in a deleterious manner (9). We evaluated the contribution of oxidative stress by treating mice with apocynin which, among many of its effects, inhibits membrane translocation of the p47 $phox$ and gp91 $phox$ subunits of Nox (13), and in our experience has been more effective at reducing adhesion molecule expression than free radical scavenger approaches. Apocynin was found to reduce molecular imaging signal for P-selectin, VCAM-1, VWF-A1 and platelet GPIb α . These data suggest that increased oxidative stress plays an important role in remote endothelial activation after MI. These findings are consistent with known effects of reactive oxygen species to stimulate adhesion molecule expression through the transcription factor nuclear factor- κ B (NF- κ B), and to inhibit proteolytic regulation of VWF (34–36). The suppression of adhesion molecule expression and platelet adhesion with apocynin was associated with partial protection from post-MI accelerated plaque progression in terms of inflammation and necrotic core size.

There are several limitations of the study that should be acknowledged. Although the murine model was selected to reflect human disease based on reproducible plaque development without extreme diet, mice do not necessarily reproduce human condition

based on both plaque location and lack of plaque rupture or erosion as the inciting event. It is also important to note that post-MI molecular imaging and plaque assessment were made only for the aorta based on the inability to resolve smaller branch non-culprit arteries and because of the unique distribution of disease in murine models. We did not make any direct measurements of oxidative stress in the different cohorts, largely because of the strength of evidence from previous studies demonstrating that oxidative biomarkers increase after MI and are reduced by apocynin (32,37). There are insufficient data to state that the primary mechanism by which apocynin reduced plaque progression after MI was directly attributable to adhesion molecule expression and platelet adhesion. Instead, we believe that lowering ROS would have pleiotropic effects that would include the endothelial abnormalities that were the focus of this study. Importantly, we do not yet have data revealing the primary inciting factor for remote plaque activation, nor do we have data on how infarct size or duration of ischemia influence the degree of remote plaque activation.

In summary, myocardial infarction leads to remote endothelial activation and abnormal regulation of endothelial-associated and possibly leukocyte-associated VWF (Central Illustration). These processes are associated with enhanced monocyte recruitment, platelet-endothelial adhesion, and acceleration of plaque progression. Interrupting the endogenous vascular production of ROS with the Nox inhibitor apocynin suppresses adverse remote endothelial changes. Our findings help understand mechanisms for heightened risk for recurrent events after MI, and reveal potentially modifiable processes. They could also contribute to the mechanistic understanding of the recently-described beneficial effects of pro-inflammatory cytokine inhibition in patients with MI (38).

This study demonstrates application of several techniques described in this thesis as they are used in a complementary fashion to characterize remote molecular and cellular endothelial events, measure atherosclerotic progression, and evaluate a potential anti-oxidant therapy following a remote ischemic event. Specifically, CEU molecular imaging, intravital microscopy, and histology were used to detect molecular and cellular events in different territories, based on the abilities and limitations of each technique. CEU molecular imaging provided a measure of molecular signal at the

endothelial surface of a large artery. Intravital microscopy produced visual and quantitative data of cellular interactions in the peripheral microcirculation. Imaging of extravascular infiltration of macrophages, plaque growth, and plaque destabilization required aortic histology and immunostaining, which also produced corroboratory data on surface VCAM-1 expression. While this study concerned events at the endothelial surface of remote arteries, it was essential to also image cardiac function via echocardiography in order to provide confirmation of induced myocardial infarction. Leveraged together, these techniques led to a better understanding of the global vascular effects of myocardial ischemia as well as validation that targeting oxidative processes can limit adverse changes.

Summary of Techniques

This study provided an ideal example of how the many techniques discussed in earlier chapters can be leveraged together in order to relate cardiac processes to vascular and endothelial processes. 2D echocardiography and measurement of ST-elevation on electrocardiogram were used to measure the presence and extent of myocardial infarction after ligation of the LAD. Beyond simply confirming that ligation resulted in myocardial ischemia, the presence of wall motion abnormalities and reduced longitudinal strain were used to demonstrate that this model of ischemia sufficiently approximated a human MI. Additionally, the sham procedures demonstrated that all vascular changes measured were the result of the MI rather than the surgical procedure used to induce it.

The central principle of this study is that an ischemic event in one territory of myocardium leads to a series of changes throughout the vasculature. After successfully demonstrating the MI model using echocardiography and EKG changes, several techniques were used to measure changes to the vascular endothelium and plaques in the subendothelial space. CEU molecular imaging revealed the time-course of changes in endothelial ECAM and VWF surface expression and recruitment of platelets, and histological analysis was used to both confirm CEU findings and show accelerated atherosclerotic plaque growth and destabilization through increased inflammation and loss of collagen. Intravital microscopy findings suggested that the vascular changes

observed in the aortic root were truly global and affected vascular beds in territories as remote as the cremaster muscle, and also allowed us to directly visualize recruitment of leukocytes by adherent platelets and characteristic VWF-platelet string formation and embolization.

References

1. Stone GW, Maehara A, Lansky AJ, et al. A prospective natural-history study of coronary atherosclerosis. *N Engl J Med*. 2011;364:226–35.
2. Witt BJ, Brown RD, Jr, Jacobsen SJ, Weston SA, Yawn BP, Roger VL. A community-based study of stroke incidence after myocardial infarction. *Annals of internal medicine*. 2005;143:785–92.
3. Milonas C, Jernberg T, Lindback J, et al. Effect of Angiotensin-converting enzyme inhibition on one-year mortality and frequency of repeat acute myocardial infarction in patients with acute myocardial infarction. *Am J Cardiol*. 2010;105:1229–34.
4. Dutta P, Courties G, Wei Y, et al. Myocardial infarction accelerates atherosclerosis. *Nature*. 2012;487:325–9.
5. Lee WW, Marinelli B, van der Laan AM, et al. PET/MRI of inflammation in myocardial infarction. *J Am Coll Cardiol*. 2012;59:153–63.
6. Kaufmann BA, Carr CL, Belcik JT, et al. Molecular imaging of the initial inflammatory response in atherosclerosis: implications for early detection of disease. *Arterioscler Thromb Vasc Biol*. 2010;30:54–9.
7. Shim CY, Liu YN, Atkinson T, et al. Molecular Imaging of Platelet-Endothelial Interactions and Endothelial von Willebrand Factor in Early and Mid-Stage Atherosclerosis. *Circ Cardiovasc Imaging*. 2015;8:e002765.
8. Chadderdon SM, Belcik JT, Bader L, et al. Proinflammatory endothelial activation detected by molecular imaging in obese nonhuman primates coincides with onset of insulin resistance and progressively increases with duration of insulin resistance. *Circulation*. 2014;129:471–8.
9. Wu MD, Atkinson TM, Lindner JR. Platelets and von Willebrand factor in atherogenesis. *Blood*. 2017;129:1415–1419.
10. Dong JF. Cleavage of ultra-large von Willebrand factor by ADAMTS-13 under flow conditions. *Journal of thrombosis and haemostasis: JTH*. 2005;3:1710–6.
11. Ruggeri ZM. Von Willebrand factor, platelets and endothelial cell interactions. *Journal of thrombosis and haemostasis: JTH*. 2003;1:1335–42.
12. Powell-Braxton L, Veniant M, Latvala RD, et al. A mouse model of human familial hypercholesterolemia: markedly elevated low density lipoprotein cholesterol levels and severe atherosclerosis on a low-fat chow diet. *Nat Med*. 1998;4:934–8.
13. Yu J, Weiwer M, Linhardt RJ, Dordick JS. The role of the methoxyphenol apocynin, a vascular NADPH oxidase inhibitor, as a chemopreventative agent in the potential treatment of cardiovascular diseases. *Curr Vasc Pharmacol*. 2008;6:204–17.
14. Impellizzeri D, Esposito E, Mazzon E, et al. Effect of apocynin, a NADPH oxidase inhibitor, on acute lung inflammation. *Biochem Pharmacol*. 81:636–48.
15. Kaufmann BA, Sanders JM, Davis C, et al. Molecular imaging of inflammation in atherosclerosis with targeted ultrasound detection of vascular cell adhesion molecule-1. *Circulation*. 2007;116:276–84.
16. Lindner JR, Coggins MP, Kaul S, Klibanov AL, Brandenburger GH, Ley K. Microbubble persistence in the microcirculation during ischemia/reperfusion and inflammation is caused by integrin- and complement-mediated adherence to activated leukocytes. *Circulation*. 2000;101:668–75.
17. Dong JF, Moake JL, Nolasco L, et al. ADAMTS-13 rapidly cleaves newly secreted ultralarge von Willebrand factor multimers on the endothelial surface under flowing conditions. *Blood*. 2002;100:4033–9.

18. Madjid M, Awan I, Willerson JT, Casscells SW. Leukocyte count and coronary heart disease: implications for risk assessment. *J Am Coll Cardiol*. 2004;44:1945–56.
19. Fang L, Moore XL, Dart AM, Wang LM. Systemic inflammatory response following acute myocardial infarction. *J Geriatr Cardiol*. 2015;12:305–12.
20. Gonzalez-Quesada C, Frangogiannis NG. Monocyte chemoattractant protein-1/CCL2 as a biomarker in acute coronary syndromes. *Curr Atheroscler Rep*. 2009;11:131–8.
21. Kim EJ, Kim S, Kang DO, Seo HS. Metabolic activity of the spleen and bone marrow in patients with acute myocardial infarction evaluated by 18f-fluorodeoxyglucose positron emission tomographic imaging. *Circ Cardiovasc Imaging*. 2014;7:454–60.
22. Galkina E, Ley K. Vascular adhesion molecules in atherosclerosis. *Arterioscler Thromb Vasc Biol*. 2007;27:2292–301.
23. Nording HM, Seizer P, Langer HF. Platelets in inflammation and atherogenesis. *Frontiers in immunology*. 2015;6:98.
24. Langer HF, Gawaz M. Platelet-vessel wall interactions in atherosclerotic disease. *Thromb Haemost*. 2008;99:480–6.
25. Henn V, Slupsky JR, Grafe M, et al. CD40 ligand on activated platelets triggers an inflammatory reaction of endothelial cells. *Nature*. 1998;391:591–4.
26. Huo Y, Schober A, Forlow SB, et al. Circulating activated platelets exacerbate atherosclerosis in mice deficient in apolipoprotein E. *Nat Med*. 2003;9:61–7.
27. Massberg S, Brand K, Gruner S, et al. A critical role of platelet adhesion in the initiation of atherosclerotic lesion formation. *J Exp Med*. 2002;196:887–96.
28. Theilmeyer G, Michiels C, Spaepen E, et al. Endothelial von Willebrand factor recruits platelets to atherosclerosis-prone sites in response to hypercholesterolemia. *Blood*. 2002;99:4486–93.
29. Liu Y, Davidson BP, Yue Q, et al. Molecular imaging of inflammation and platelet adhesion in advanced atherosclerosis effects of antioxidant therapy with NADPH oxidase inhibition. *Circ Cardiovasc Imaging*. 2013;6:74–82.
30. Chauhan AK, Goerge T, Schneider SW, Wagner DD. Formation of platelet strings and microthrombi in the presence of ADAMTS-13 inhibitor does not require P-selectin or beta3 integrin. *Journal of thrombosis and haemostasis: JTH*. 2007;5:583–9.
31. Pendu R, Terraube V, Christophe OD, et al. P-selectin glycoprotein ligand 1 and beta2-integrins cooperate in the adhesion of leukocytes to von Willebrand factor. *Blood*. 2006;108:3746–52.
32. Neri M, Fineschi V, Di Paolo M, et al. Cardiac oxidative stress and inflammatory cytokines response after myocardial infarction. *Curr Vasc Pharmacol*. 2015;13:26–36.
33. Araujo FB, Barbosa DS, Hsin CY, Maranhao RC, Abdalla DS. Evaluation of oxidative stress in patients with hyperlipidemia. *Atherosclerosis*. 1995;117:61–71.
34. Kunsch C, Medford RM. Oxidative stress as a regulator of gene expression in the vasculature. *Circ Res*. 1999;85:753–66.
35. Chen J, Fu X, Wang Y, et al. Oxidative modification of von Willebrand factor by neutrophil oxidants inhibits its cleavage by ADAMTS13. *Blood*. 2010;115:706–12.
36. Drummond GR, Selemidis S, Griendling KK, Sobey CG. Combating oxidative stress in vascular disease: NADPH oxidases as therapeutic targets. *Nat Rev Drug Discov*. 2011;10:453–71.
37. Li B, Tian J, Sun Y, et al. Activation of NADPH oxidase mediates increased endoplasmic reticulum stress and left ventricular remodeling after myocardial infarction in rabbits. *Biochimica et biophysica acta*. 2015;1852:805–15.
38. Ridker PM, Everett BM, Thuren T, et al. Antiinflammatory Therapy with Canakinumab for Atherosclerotic Disease. *N Engl J Med*. 2017;377:1119–1131.

Cardiovascular Toxicity of Tyrosine Kinase Inhibitors

Summary

The third-generation tyrosine kinase inhibitor (TKI) ponatinib has been associated with high rates of acute ischemic events. The pathophysiology responsible for these events is unknown. We hypothesized that ponatinib produces an endothelial angiopathy involving excessive endothelial-associated von Willebrand factor (VWF) and secondary platelet adhesion. In wild-type mice and ApoE^{-/-} mice on a Western diet, ultrasound molecular imaging of the thoracic aorta for VWF A1-domain and glycoprotein-Iba was performed to quantify endothelial-associated VWF and platelet adhesion.

After treatment of wild-type mice for 7 days, aortic molecular signal for endothelial-associated VWF and platelet adhesion were five- to sixfold higher in ponatinib vs sham therapy ($P < .001$), whereas dasatinib had no effect. In ApoE^{-/-} mice, aortic VWF and platelet signals were two- to fourfold higher for ponatinib-treated compared with sham-treated mice ($P < .05$) and were significantly higher than in treated wild-type mice ($P < .05$). Platelet and VWF signals in ponatinib-treated mice were significantly reduced by *N*-acetylcysteine and completely eliminated by recombinant ADAMTS13. Ponatinib produced segmental left ventricular wall motion abnormalities in 33% of wild-type and 45% of ApoE^{-/-} mice and corresponding patchy perfusion defects, yet coronary arteries were normal on angiography. Instead, a global microvascular angiopathy was detected by immunohistochemistry and by intravital microscopy observation of platelet aggregates and nets associated with endothelial cells and leukocytes. Our findings reveal a new form of vascular toxicity for the TKI ponatinib that

involves VWF-mediated platelet adhesion and a secondary microvascular angiopathy that produces ischemic wall motion abnormalities. These processes can be mitigated by interventions known to reduce VWF multimer size.

Background

Tyrosine kinase inhibitors (TKIs) have revolutionized the treatment of patients with chronic myelogenous leukemia (CML). In CML, the t(9;22) chromosomal translocation results in production of the oncogenic tyrosine kinase BCR-ABL1. TKIs targeted to BCR-ABL1 inhibit the proliferation and survival of malignant cells and result in long-term disease-free survival rates of nearly 80%.^{1,2} Ponatinib is a third-generation BCR-ABL1 TKI with a broad range of activity against other TKs (vascular endothelial growth factor, fibroblast growth factor, and platelet-derived growth factor receptors) and is the only TKI that is approved for treating CML rendered drug resistant by the T315I mutation.³⁻⁵ However, the use of ponatinib in patients has been curtailed, and at one point temporarily halted, by the US Food and Drug Administration, because of high rates of vascular toxicity manifest as acute thrombotic occlusive events within months of initiating therapy, the cause of which is unknown.^{6,7}

In this study, in vivo imaging methods unique in their ability to investigate events at the endothelial-blood pool interface, including in vivo ultrasound molecular imaging and intravital microscopy, were used to assess endothelial alterations that underlie the vascular complications of ponatinib. These approaches have recently been applied to elucidate sudden high-risk endothelial changes that occur globally after focal myocardial ischemia.⁸ We applied these techniques to investigate whether ponatinib produces an arterial and microvascular endothelial angiopathy involving excessive endothelial-associated von Willebrand factor (VWF) and secondary glycoprotein-Ib α (GPIb α)–mediated platelet adhesion. Because myocardial infarction is one of the most frequent vascular complications, we also assessed whether these endothelial changes result in ischemic left ventricular (LV) wall motion abnormalities (WMAs). With regards to potential mitigation strategies, we tested whether the platelet-related angiopathy could be partially prevented by *N*-acetylcysteine (NAC), which can potentially reduce VWF

multimer size through direct effects on self-association and secondary effects on endogenous protease activity.⁹

Materials and Methods

Animals

The study was approved by the Animal Care and Use Committee of Oregon Health & Science University. We studied wild-type C57Bl/6 mice and hyperlipidemic mice with susceptibility to atherosclerosis produced by gene deletion of the apolipoprotein-E (ApoE^{-/-}) fed a “Western-style” diet (WSD) consisting of 42% of calories from fat (Teklad TD.88137, Envigo) for 6 weeks prior to the study. Mice were studied at 15 to 20 weeks of age, which for ApoE^{-/-} mice on a WSD is expected to represent a stage at which there are early atherosclerotic lesions in the aortic root and proximal aorta.^{10,11} For all studies except intravital microscopy, mice were anesthetized with 1.0% to 2.0% inhaled isoflurane, and euthermia was maintained. A jugular cannula was placed for IV injection of contrast agents or drugs when necessary. For intravital microscopy, mice were anesthetized with intraperitoneal injection (10-15 μ L/g) of a solution containing ketamine hydrochloride (10 mg/mL), xylazine (1 mg/mL), and atropine (0.02 mg/mL).

TKI Drug Therapy and Study Design

For TKI therapy in mice, either ponatinib (30 mg/kg) or dasatinib (20 mg/kg) was dissolved in a solution of citrate titrated to achieve a pH of 2.75 and administered as a daily oral gavage. Doses of TKI were selected a priori based on studies demonstrating therapeutic response in murine models of malignancy.¹²⁻¹⁴ NAC was administered by daily gavage at the same time as ponatinib at a dose (600 mg/kg) that was weight adjusted to be in slight excess to that used to treat acetaminophen poisoning. Mice were treated for 7 days prior to being studied with contrast-enhanced ultrasound (CEU) molecular imaging, intravital microscopy, echocardiography, or computed tomography (CT) coronary angiography.

Tail Cuff Blood Pressure Measurement

Daily blood pressure measurements were performed with a mouse tail cuff plethysmograph (IITC Life Science Inc., Woodland Hills) by the same female operator (Y.L.) in a designated quiet room. Mice were habituated for ≥ 10 days prior to initiation of therapy by allowing their spontaneous entry into the restraint tube and subsequent adjustment of the tube length to limit motion. The cuff was placed at the base of the tail. System temperature was set at 34° C. Fifteen sequential blood pressure measurements were made, the first five of which were used for acclimation and the last ten of which were then averaged.

CEU Molecular Imaging Study Assignments

The following conditions were tested to evaluate aortic endothelial response to TKIs using contrast-enhanced ultrasound as an in vivo readout:

1. Molecular imaging performed in wild-type mice at baseline and after 7 days of daily therapy with ponatinib, dasatinib, or vehicle.
2. Molecular imaging performed in ApoE^{-/-} mice on a WSD at baseline and after 7 days of daily therapy with ponatinib, ponatinib + NAC, or vehicle.
3. Molecular imaging performed in ApoE^{-/-} mice on a WSD after 7 days of daily therapy with ponatinib that also received recombinant human ADAMTS13 (a disintegrin and metalloprotease with thrombospondin type I repeats-13) (5 μ g IV) 1 hour prior to imaging. ADAMTS13, which is a regulatory protease that cleaves VWF at the A2 domain, was used to reduce ultralarge VWF multimer size after surface expression by endothelial cells.[15,16](#)

Preparation of CEU Molecular Imaging Targeted Contrast Agents

Lipid-shelled decafluorobutane microbubbles bearing a bifunctional conjugation moiety consisting of a hydrophobic domain and a biotin domain at the end of a polyethylene glycol spacer were prepared by sonication of a gas-saturated aqueous suspension of distearoylphosphatidylcholine (2 mg/mL), polyoxyethylene-40-stearate (1 mg/mL), and distearoylphosphatidylethanolamine-PEG(2000)biotin (0.4 mg/mL). Conjugation of biotinylated ligand to the microbubble surface was performed with biotin-

streptavidin bridging as previously described.^{11,17} Ligands used for targeting were dimeric murine recombinant A1 domain of VWF A1 (mature VWF amino acids 445 to 716) for targeting platelet GPIIb α , and a cell-derived peptide representing the N-terminal 300 amino acids of GPIIb α for targeting the VWF A1 domain, which is exposed by shear on ultralarge multimers.¹⁸ Control microbubbles were prepared with isotype control antibody (R3-34, BD Biosciences). Microbubble concentrations and size distributions were measured by electrozone sensing (Multisizer III; Beckman Coulter, Brea, CA).

CEU Molecular Imaging

CEU molecular imaging of the ascending thoracic aorta and proximal arch were imaged using a right parasternal window with a 15L7 linear-array probe (Sequoia; Siemens, Mountain View, CA). Multipulse phase-inversion and amplitude-modulation imaging was performed to specifically detect the nonlinear signals generated at the fundamental and harmonic frequencies by microbubble cavitation.^{19,20} Imaging was performed at a transmission frequency of 7 MHz and a dynamic range of 55 dB. The mechanical index was set at 1.0. Images were acquired 8 minutes after IV injection of targeted or control microbubbles (1×10^6) performed in random order. Signal from retained microbubbles alone was determined as previously described by acquiring the first ultrasound frame and then digitally subtracting several averaged frames obtained after complete destruction of microbubbles at a mechanical index of 1.4 to eliminate signal from the low concentration of freely circulating microbubbles in the blood pool.¹¹ Signal intensity was measured from a region of interest encompassing the entire ascending aorta to just beyond the origin of the brachiocephalic artery. Region selection was facilitated by fundamental 2-dimensional imaging at 14 MHz acquired after each CEU imaging sequence.

Echocardiography

Echocardiography was performed to assess LV function. High-frequency (40 MHz) transthoracic echocardiography (Vevo 2100, VisualSonics Inc., Toronto, Canada) was performed using a parasternal long-axis and sequential parasternal shortaxis imaging planes to assess regional wall motion. LV dimensions at end-systole and end-

diastole and fractional shortening (percent change in LV diameter normalized to end-diastole) were measured from the parasternal long-axis view using linear measurements of the LV at the level of the mitral leaflet tips during diastole. Radial strain was calculated using speckle-tracking echocardiography from a summation of mid- and apical short-axis images view and was quantified as the average of a standard single 6-segment model at the mid, and 4-segmental model at the apex. Stroke volume was calculated as the product of the left ventricular outflow tract crosssectional area and time-velocity integral on pulsed-wave Doppler. The presence versus absence of any wall motion abnormalities was made by an experienced observer blinded to condition.

CT Coronary Angiography

CT coronary angiography was performed immediately after echocardiography in several sham-treated mice and ApoE^{-/-} mice treated with ponatinib that were selected based on presence of obvious WMAs. Mice were treated with 1000 U sodium heparin by intraperitoneal injection. After 15 minutes, an anterior laparotomy was performed in order to selectively cannulate the descending aorta. Retrograde perfusion of the coronary circulation at a perfusion pressure of 100 mm Hg was performed with phosphate-buffered saline at 37°C containing 0.1 mM sodium nitroprusside and 1 mM papaverine in order to clear the intravascular blood pool and achieve maximal vasodilation of the coronary vasculature. Retrograde perfusion fixation was performed with 1% paraformaldehyde followed immediately by perfusion with a radiopaque silicone-based casting agent (Microfil Flow Tech, Carver, MA) prepared as 8:1:1 parts latex/diluent/curing agent, per the manufacturer's instructions. Once the coronary arteries were visually confirmed to be filled, perfusion pressure was maintained for an additional 5 to 10 minutes. After curing for 1 hour, the heart was removed and immersion fixed in 2% paraformaldehyde overnight. Micro-CT angiography (Inveon, Siemens) was performed using a 14-bit X-ray detector and a full 360° rotation at 1° increments and 6870-ms exposure times. Imaging was performed at a peak voltage of 30 kV (0.5 mA tube current) with maximal intensity projection processing.

Spatial Assessment of Perfusion by Microspheres

In animals not undergoing CT coronary angiography, immediately after echocardiography, animals were intubated and placed on mechanical ventilation using weight-adjusted tidal volumes. A left lateral thoracotomy was performed to expose the left ventricular apex, through which a 23 g needle was placed to infuse 200 μ l of a 1% w/v solution of fluorescently-labeled polystyrene microspheres 3-8 μ m in diameter (Duke Scientific Corp., Palo Alto, California). Microspheres were allowed to circulate for 2 minutes. The heart was removed and cut into seven equal-thickness short-axis sections. Digital images of the basal aspect of all sections were acquired under ultraviolet light and the summed area devoid of fluorescent microspheres summed for all sections was measured and expressed as a ratio to total summed left ventricular area.

Intravital Microscopy

Direct observation of platelet- and leukocyte-endothelial interactions was performed with intravital microscopy in male wild-type mice and ApoE^{-/-} mice on a WSD after 1 week of treatment with ponatinib or vehicle. The cremaster muscle was exteriorized and prepared for intravital microscopy using a buffered isothermic superfusion as previously described.²¹ Microscopy was performed with combined fluorescent epi-illumination and low-intensity transillumination (Axioskop2-FS; Carl Zeiss, Thornwood, NY) and a high-resolution charge-coupled device camera (C2400; Hamamatsu Photonics, Hamamatsu, Japan). In vivo fluorescent labeling of platelets was performed with rhodamine-6G (1 mg/mL, 75-100 μ L IV). The number of adherent leukocytes and platelet adhesive events (>3 s) and the formation of platelet “strings” indicative of ultra-large VWF multimers were quantified as either the number of events or the fluorescent platelet area normalized to vessel area. A minimum of 5 separate venules were assessed per animal.

Flow Cytometry

Flow cytometry was used to assess platelet surface adhesion molecule expression. Whole blood from wild-type mice treated for 7 days with ponatinib or vehicle (n=3 each) was obtained in citrated tubes and centrifuged to obtain platelet-rich plasma.

Primary rat anti-mouse monoclonal antibodies (5 μ g) against either P-selectin (RB40.34, BD Biosciences) or GPIIb α (R300, Emfret Analytics, Eibelstadt, Germany) were added to 200 mL aliquots. Platelets were then washed in phosphate-buffered saline containing 2% bovine serum albumin, and secondary staining was performed with FITC-labeled isotype-specific anti-rat secondary antibody (RG11 or RG7, BD Biosciences). Flow cytometry (FACSCanto II, BD Biosciences) was performed gated to the platelet window on forward and side scatter. Data are expressed as the average of the geometric mean for fluorescence intensity.

Endothelial ROS Production, Viability, and VWF secretion

Murine endothelial cells (SVEC4-10; ATCC, Manassas, VA) were grown to confluence in Dulbecco's modified Eagle medium growth medium supplemented with 10% fetal bovine serum. Cells were exposed to ponatinib added to the growth medium to reach a final concentration of 0.1, 0.5, 1.0, or 2.5 μ M for 2 hours. Positive control experiments were performed by adding 10 mL of a 100 mM solution of phorbol 12-myristate 13-acetate to SVE4-10 cells for 30 minutes. For assessing reactive oxygen species (ROS), 2',7'-dichlorodihydrofluorescein diacetate succinimidyl ester (H₂DCFDA; OxyBURST Green, ThermoFisher Scientific) was added to the culture medium at a final concentration of 1 mM for 10 minutes prior to fluorescence microscopy (Axioscop-2, Carl Zeiss) at an emission wavelength of 490 nm and a constant output intensity. Mean fluorescent intensity for H₂DCFDA was measured from a minimum of 10 random fields of view (ImageJ; National Institutes of Health, Bethesda, MD).²²

For cell viability, costaining was performed with propidium iodide (PI) at a final concentration of 5 mM and 4',6-diamidin-2-phenylindol (DAPI) for 5 minutes then washed. Endothelial cell viability was measured by the proportion of DAPI-stained nuclei that also stained with PI in a minimum of 10 randomly selected fields of view. For assessment of VWF secretion, a microfluidic cell culture chamber (VI0.1; ibidi, Martinsried, Germany) was seeded with 2×10^6 human umbilical vein endothelial cells (HUVECs) and infused with complete medium overnight at a shear rate of 200 s⁻¹. Cells were exposed to serum-free medium for 2 hours and then for 24 hours with serum-free medium with either 0.1% fatty acid-free bovine serum albumin (control), ponatinib (0.5

mM), or tumor necrosis factor α (TNF- α ; 10 ng/mL) (positive control). Cells were then fixed and immunostained without permeabilization with rabbit anti-human VWF (A0082; DAKO, Santa Clara, CA) and mouse anti-human CD31 (WM59; Thermo Fisher Scientific, Grand Island, NY) polyclonal antibodies, and Alexa Fluor–labeled secondary antibodies. Area staining for VWF was assessed in 5 random fields of view per chamber.

Histology

For immunohistochemistry of the LV myocardium, myocardial blood volume was removed by retrograde aortic perfusion at physiologic pressure of isothermic phosphate-buffered saline containing 2.5% albumin. Perfusion-fixed short-axis thick sections that, for ponatinib-treated mice, included both the areas with and without WMA were cut. Immersion-fixed sections from the kidneys of ponatinib- and vehicle-treated mice were also assessed. Immunohistochemistry was performed using rat anti-mouse monoclonal antibody against platelet CD41 (ab33661; Abcam, Cambridge, MA), and secondary staining with donkey ant-rat Cy3-labeled polyclonal antibody (Jackson ImmunoResearch, West Grove, PA). Endothelial staining was performed with Alexa Fluor 488–conjugated isolectin GS-IB4 (Invitrogen, Grand Island, NY). Nuclear counterstaining was performed with Hoechst 33342 (Invitrogen). Fluorescent microscopy was performed on a confocal system (TCS SP5; Leica Microsystems, Buffalo Grove, IL).

Statistical Analysis

Data analysis was performed with Prism v7.0a (Graph Pad, La Jolla, California). Continuous variables that were normally distributed are displayed as mean \pm SD unless stated otherwise; whereas those that were not normally distributed are displayed as box-whisker plots with a bar representing median, box representing 25-75% confidence intervals, and whiskers representing range. Student t test (paired or unpaired) were performed for comparisons of normally distributed data. For non-normally distributed data, either a Mann-Whitney U test or Wilcoxon signed-rank test was used as appropriate according to experimental conditions (paired data within a group versus

group-wise comparisons). For multiple comparisons, a one-way ANOVA was performed for normally distributed data with post-hoc testing with Holm-Sidak's multiple comparisons correction. A Kruskal-Wallis test followed by Dunn's multiple comparison test was performed for non-normally distributed data. Differences in proportions (wall motion data) were compared using Fisher's exact test. Differences were considered significant at $p < 0.05$.

Results

Survival and Blood Pressure in Ponatinib-Treated Mice

Because clinical studies have indicated that patients with traditional atherosclerotic risk factors are at greater risk for ponatinib vascular toxicity,⁷ we studied both wild-type C57Bl/6 mice and mice with gene-targeted deletion of ApoE^{-/-} fed for 6 weeks with WSD. During the 1-week period of therapy, treatment-related mortality occurred only in ponatinib-treated mice, with a significantly higher mortality compared with sham-treated animals for the ApoE^{-/-} mice ([Figure 1](#)). Daily awake tail cuff blood pressure measurements in animals acclimatized to the procedure revealed a gradual increase in both systolic and diastolic blood pressure in ponatinib-treated wild-type and ApoE^{-/-} mice, whereas sham-treated mice remained normotensive ([Figure 1](#)). This hypertensive response is similar to blood pressure responses seen in two-thirds of patients receiving ponatinib²³ and likely reflects potency of ponatinib kinase against vascular endothelial growth factor receptor-2. Blood counts after days of therapy showed mild leukocytosis in ponatinib-treated mice. Schistocytes were not detected using Wright-Giemsa stain.

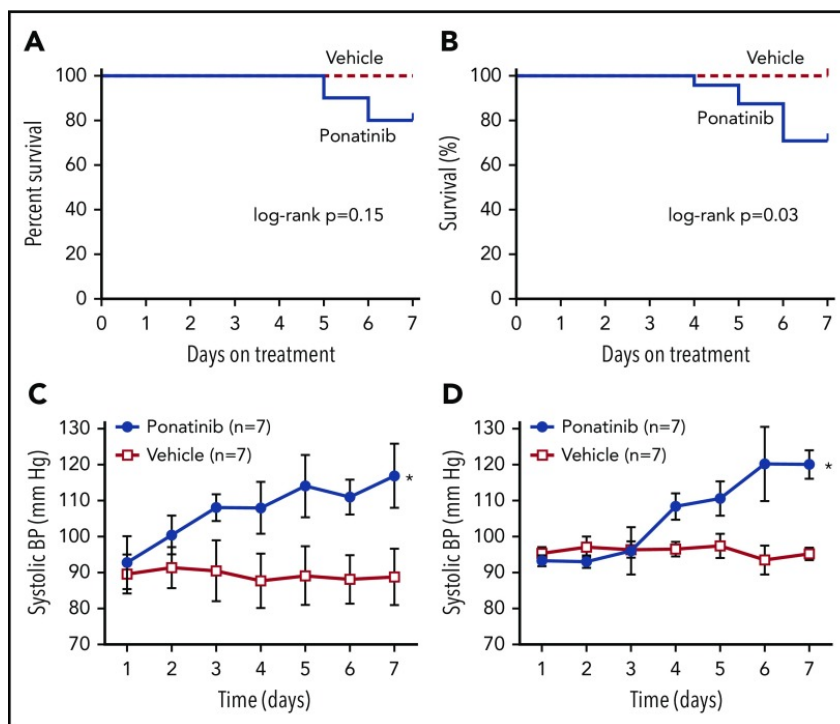


Figure 1: Kaplan-Meier curves illustrate survival after initiation of ponatinib (30 mg/kg per day) or vehicle (sham treatment) in wild-type C57Bl/6 mice (A) and ApoE^{-/-} mice on a WSD (B). Tail-cuff systolic blood pressure was measured in awake wild-type (C) and ApoE^{-/-} mice on a WSD (D) in animals that were acclimatized to the procedure prior to initiation of therapy. **P* < .05 vs vehicle. BP, blood pressure.

Vascular Prothrombotic Changes by Molecular Imaging

Molecular imaging was performed with tracers targeted to endothelial-associated large multimers of VWF that have undergone shear-mediated exposure of their platelet binding domain and to platelet GPIIb/IIIa, which reflects vascular platelet adhesion. In wild-type mice, aortic signal for VWF-A1 and platelet GPIIb/IIIa in ponatinib-treated mice was five- to sixfold greater compared with sham-treated mice (Figure 2A-B). This high degree of signal for VWF and platelet adhesion was not seen after therapy with dasatinib (20 mg/kg per day), a second-generation TKI characterized by a narrower spectrum activity than ponatinib with regards to non-BCR-ABL1 receptors that has been shown to have a much lower rate of vascular events in patients.^{5,6} Flow cytometry performed with platelets from vehicle-treated vs ponatinib-treated mice showed no difference in surface expression for GPIIb/IIIa (median fluorescence intensity, 9156 ± 1439 vs 9505 ± 1684, *P* = .90) or P-selectin (median fluorescence intensity, 6992 ± 860 vs 7536 ± 1291, *P* = .70).

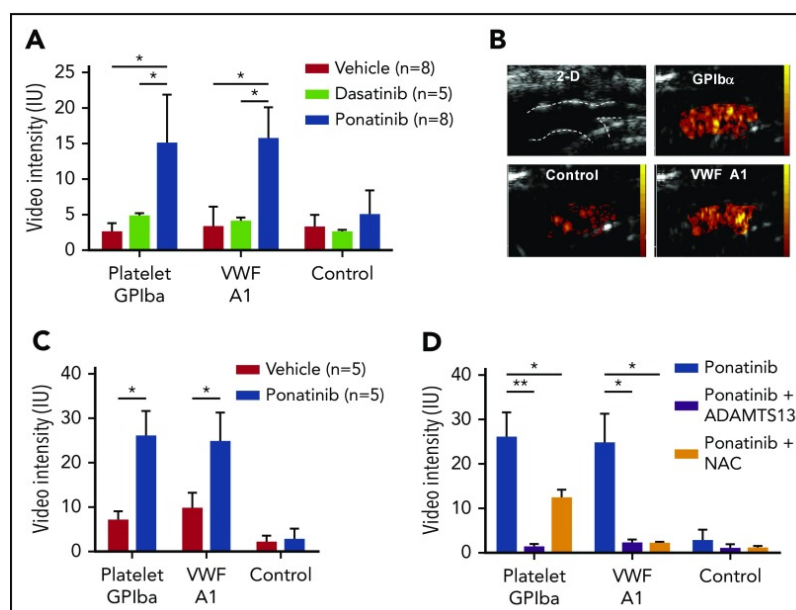


Figure 2: (A) Mean (\pm standard error of the mean [SEM]) signal enhancement measured from the proximal thoracic aorta on CEU molecular imaging using tracers targeted to platelet GPIb α , VWF A1-binding domain, or control agent, in wild-type mice treated for 1 week with ponatinib (30 mg/kg per day), dasatinib (20 mg/kg per day), or vehicle. $*P < .01$. (B) Illustrative images from a ponatinib-treated wild-type mouse showing 2-dimensional (2-D) ultrasound (14 MHz) of the proximal thoracic aorta and origin of the brachiocephalic artery (outlined), and background-subtracted color-coded (scales at right) CEU molecular imaging with control or targeted contrast agents. (C) Mean (\pm SEM) signal enhancement on CEU molecular imaging of the proximal thoracic aorta in ApoE^{-/-} mice on a WSD treated for 1 week with ponatinib (30 mg/kg per day) or vehicle. $*P < .05$. (D) CEU molecular imaging in ponatinib-treated ApoE^{-/-} mice on a WSD showing effects of either daily coadministration of NAC (600 mg/kg per day) or IV rADAMTS13 (5 μ g) given 1 hour prior to imaging. $*P < .05$; $**P < .01$. IU, international unit.

In ApoE^{-/-} mice on a WSD, ponatinib treatment was again associated with a much higher aortic molecular imaging signal for VWF-A1 and platelet GPIb α compared with sham-treated animals (Figure 2B). Compared with wild-type mice, ApoE^{-/-} mice had a higher aortic molecular imaging signal after ponatinib for both platelet GPIb α (median [interquartile range]: 25.1 [21.0-32.3] vs 13.3 [10.6-21.2], $P = .02$) and for VWF-A1 (25.1 [18.1-31.2] vs 15.3 [11.8-18.9], $P = .02$). In ponatinib-treated ApoE^{-/-} mice, IV administration of recombinant ADAMTS13 1 hour prior to molecular imaging resulted in nearly complete elimination of aortic VWF and GPIb α signal enhancement (Figure 2D), indicating that platelet adhesion was entirely attributable to endothelium-associated VWF. Treatment of ApoE^{-/-} mice with NAC, coadministered daily with ponatinib, also eliminated the VWF signal but reduced the platelet signal only by half.

Myocardial Function and Coronary Patency

Because cardiac events are among the most common of the reported ponatinib vascular toxicities seen in humans,⁷ transthoracic 2-dimensional echocardiography was performed to assess for ischemic WMAs. LV function was normal in all animals at baseline and remained normal after sham treatment in wild-type and ApoE^{-/-} mice. In ponatinib-treated mice, new segmental WMAs were frequently observed (Figure 3A-B). Segmental WMAs resulted in a decrease in average stroke volumes and, for ApoE^{-/-} mice, a worsening in systolic global radial strain (Figure 3C-D). Coadministration of NAC in ponatinib-treated ApoE^{-/-} mice prevented the reduction in stroke volume and global radial strain and reduced the proportion of animals with abnormal wall motion at 1 week, although the latter did not meet statistical significance (Fisher's exact $P = .20$).

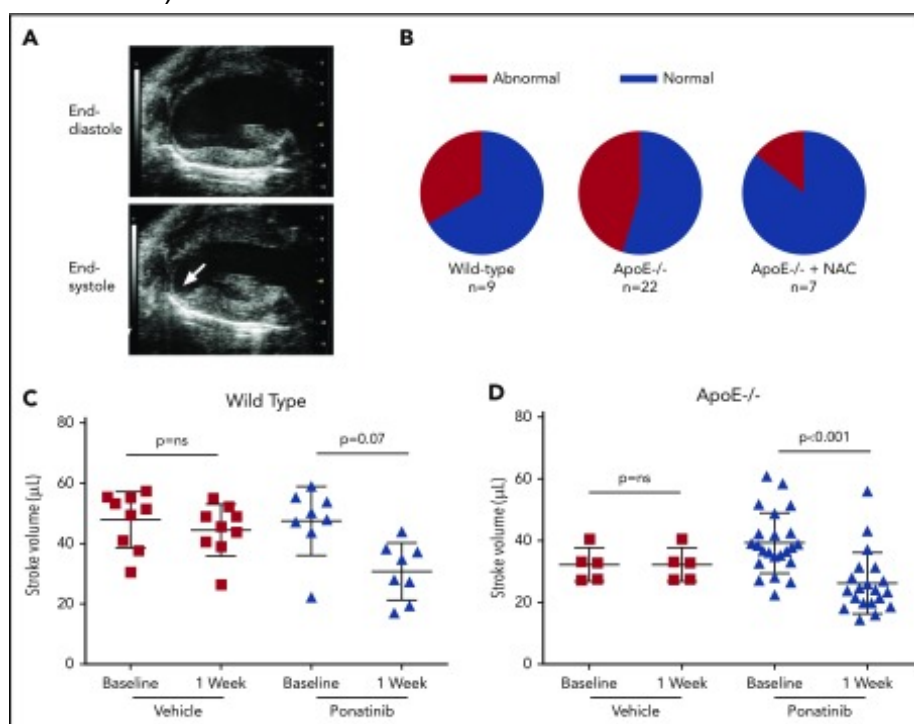


Figure 3: (A) Echocardiography in the parasternal long-axis plane at end-diastole and end-systole illustrating an inferoapical WMA (arrow, see online videos for examples of WMAs). (B) Proportion of animals with segmental LV wall motion abnormalities after 1 week of ponatinib therapy. (C-D) Echocardiographic measurement of stroke volume (bars represent mean \pm standard deviation) at baseline and after treatment (vehicle or ponatinib) in wild-type (C) and ApoE^{-/-} mice on a WSD (D). ns, not significant.

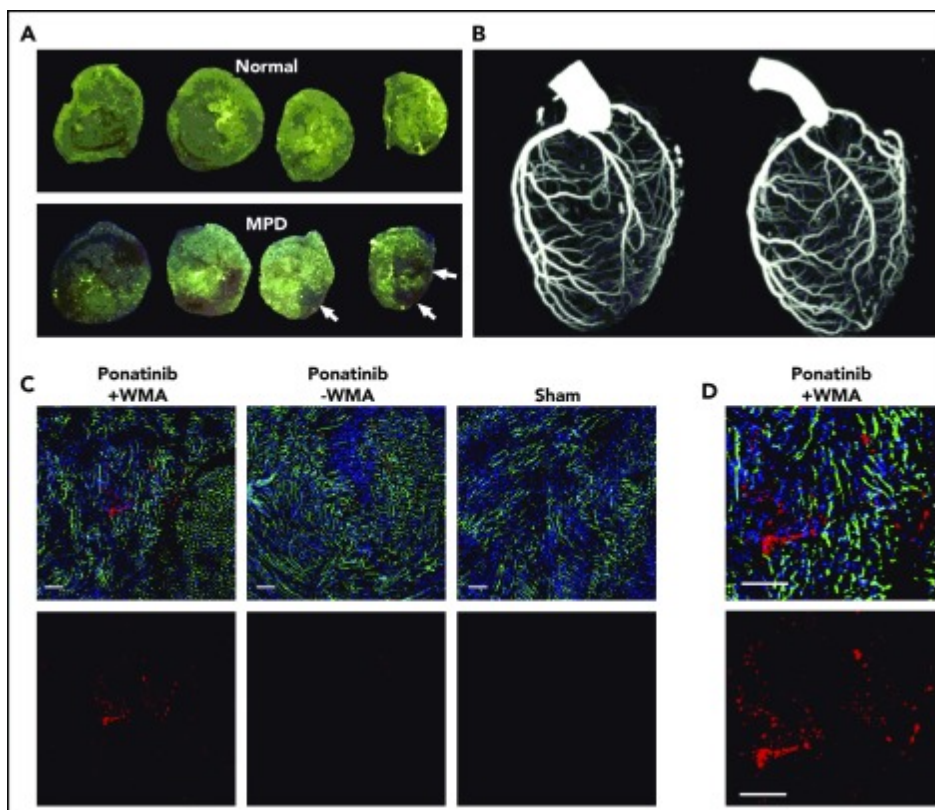


Figure 4: (A) Ex vivo epifluorescent illumination of microspheres in sequential ventricular short-axis sections illustrating normal perfusion, and focal regions of myocardial perfusion defect (MPD) (arrows). (B) CT coronary angiography in the left lateral projection illustrating lack of arterial occlusion in 2 ponatinib-treated mice with WMAs. (C) Fluorescent confocal microscopy of the LV myocardium from ponatinib-treated wild-type mice showing regions with and without WMAs and from a sham-treated mouse. Staining was performed with isolectin (green) for microvessels, Hoechst stain for nuclei (blue), and platelet CD41 immunohistochemistry (red). The bottom rows illustrate the red channel alone to better display platelets. Scale bars, 100 μm . (D) Higher-magnification image from the ponatinib-treated animal with WMA.

In mice with WMAs, spatially matched patchy LV myocardial perfusion defects were observed on postmortem analysis of the distribution of fluorescent microspheres given just prior to euthanasia ([Figure 4A](#)). Quantitatively, the area void of microspheres was greater for ponatinib-treated than sham-treated animals for both wild-type (23.1 ± 11.7 vs 3.1 ± 2.2 , $P < .001$) and ApoE^{-/-} mice (26.5 ± 9.3 vs 5.7 ± 2.7 , $P < .001$). Despite the presence of perfusion defects on microsphere analysis, CT coronary arteriography failed to detect coronary artery stenosis or occlusion in ponatinib-treated mice ([Figure 4B](#)). To investigate the possibility of a microvascular thrombotic angiopathy, immunohistochemistry of the LV was performed and showed multiple large

platelet aggregates in ponatinib-treated mice only in myocardial regions with WMAs (Figure 4C-D). Aggregates were absent in sham-treated mice. Immunohistochemistry of renal tissue, which was performed to assess a nonmyocardial organ, also showed an increase in microvascular platelets in the form of small aggregates.

Microvascular Platelet Adhesion

To further assess for global thrombotic microangiopathy, intravital microscopy of the cremaster muscle was used to directly observe the microcirculation for similar endothelial-related changes. In wild-type mice and in ApoE^{-/-} mice on a WSD, ponatinib resulted in a greater number of platelet-endothelial interactions manifest either as nontransient platelet endothelial adhesion or as platelet aggregates in the form of linear strings and nets associated with the endothelium or leukocytes (Figure 5). Events were seen in both venules and arterioles, and occasional embolization was observed.

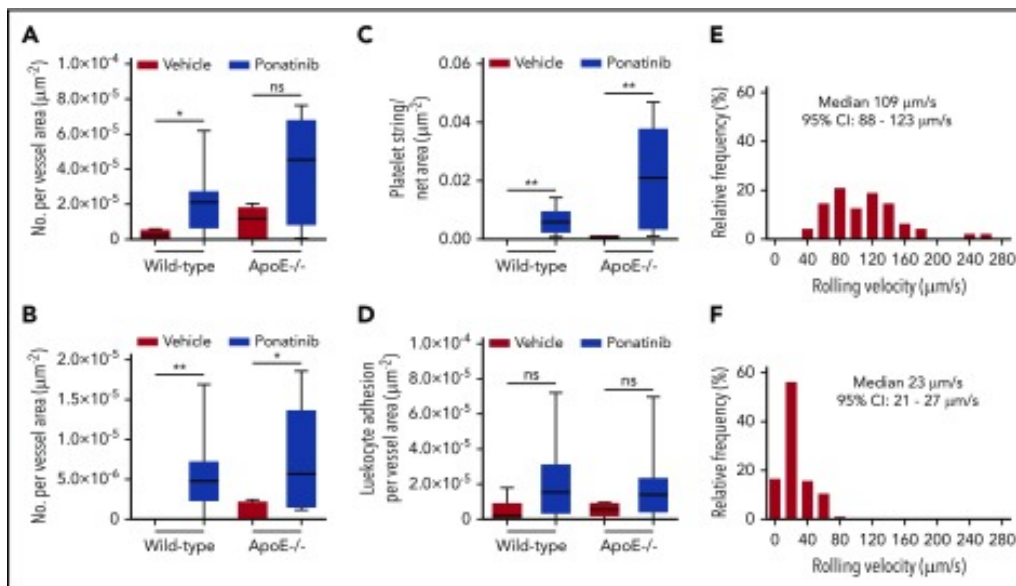


Figure 5: Box-whisker plots for intravital microscopy data from the cremasteric microcirculation of vehicle (sham) or ponatinib-treated wild-type and ApoE^{-/-} mice illustrating the number of platelets adhering to the microvascular endothelium (A), the number of platelet strings or nets (B), the area of adherent platelet strings or nets (C), and the number of leukocytes adhered in postcapillary venules (D). **P* < .05; ***P* < .01. (E-F) Histograms illustrating the distribution of leukocyte rolling velocities in cremasteric venules for ApoE^{-/-} mice on a WSD for animals treated with vehicle (E) or ponatinib (F). Rolling velocity was slower for ponatinib-treated mice (*P* < .01 by Mann-Whitney rank-sum test). ns, not significant.

Because platelet adhesion can promote endothelial cell adhesion molecular expression and can directly participate in leukocyte adhesion and extravasation, [24,25](#) leukocyte recruitment was also analyzed. Ponatinib-treated mice had substantially slower venular leukocyte rolling velocities, but only trends for greater leukocyte adhesion were seen ([Figure 5](#)). Plasma showed modest, nonsignificant increases in VWF antigen levels by enzyme-linked immunosorbent assay for ponatinib-treated wild-type and ApoE^{-/-} mice compared with sham-treated controls.

Endothelial ROS Production and VWF Expression

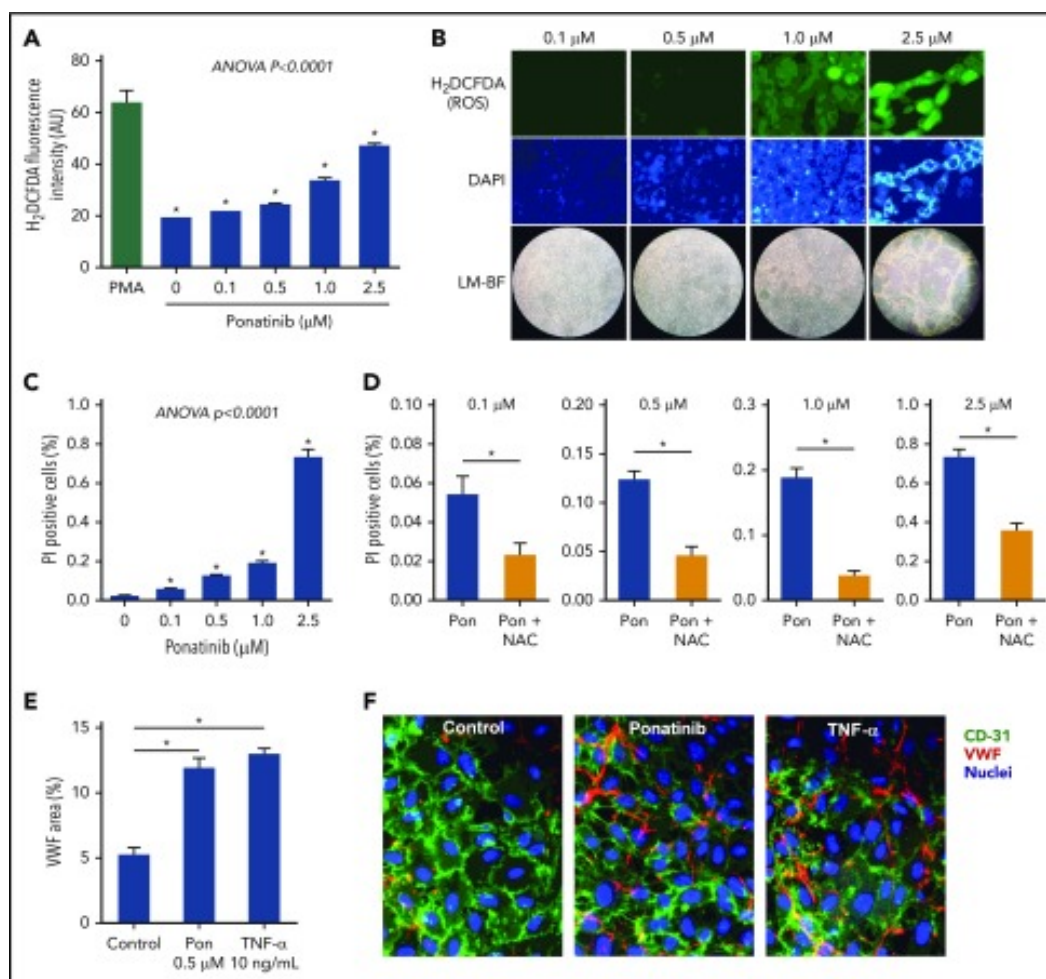


Figure 6: A) ROS generation by SVEC4-10 endothelial cells in culture measured by mean (\pm SEM) H₂DCFDA fluorescence after 24 hours of ponatinib treatment. Positive control data are shown for phorbol 12-myristate 13-acetate (PMA)-treated cells. (B) Examples of SVEC4-10 cells exposed for 24 hours to ponatinib (0.1 to 2.5 μ M) by fluorescent imaging of H₂DCFDA and DAPI (nuclear staining) illustrating dose-dependent increase in ROS, and low-magnification bright-field (LM-BF) microscopy illustrating loss

of cell confluence at high concentrations. (C) Mean (\pm SEM) cell viability after 24 hours of exposure to ponatinib (0.1 to 2.5 μ M) determined by the proportion of cells staining positive for PI. $*P < .05$ vs all other conditions by post hoc testing after correction for multiple comparisons. (D) Cell viability at various concentrations of ponatinib (Pon) with and without NAC. $*P < .05$. (E-F) Mean (\pm SEM) area for externalized VWF on HUVECs in a microfluidic chamber after 24 hours of exposure to ponatinib (0.5 μ M), TNF- α (10 ng/mL), or control serum, and examples of fluorescent microscopy for each condition. $*P < .01$. AU, arbitrary unit.

To better understand the ameliorative effects of NAC in ponatinib-treated mice, production of ROS from ponatinib-treated cultured SVEC4-10 murine endothelial cells was measured. Ponatinib added to the growth media for 24 hours resulted in a concentration-dependent increase in endothelial-derived ROS, as measured by H₂DCFDA fluorescence, and a loss of cell confluence at supraphysiologic ($>0.5 \mu$ M) concentrations ([Figure 6](#)).²⁶ There was also a dose-dependent loss of cell viability, as determined by PI staining. The proportion of nonviable cells was substantially attenuated by addition of NAC. Microfluidic chamber experiments in HUVECs exposed to ponatinib (0.5 μ M) for 24 hours demonstrated that VWF mobilization to the cell surface was much greater than in control conditions and was equivalent to that achieved by TNF- α ([Figure 6](#)).

Discussion

This study provides evidence for a new form of cardiotoxicity associated with TKIs that are used for therapy in CML. Our results indicate that the third-generation TKI ponatinib, which has a broad spectrum of TKI activity and is active against disease that is drug resistant from the T315I mutation, can produce prothrombotic angiopathy manifest by platelet adhesion. This platelet adhesion is mediated by GPIIb α binding of exposed A1 domain on VWF that is endothelial associated or associated with leukocyte–platelet complexes. These processes occur in both large arteries and the peripheral microcirculation and in the latter can produce ischemic changes in ventricular function. These platelet-mediated events are likely to be involved in the processes responsible for the high incidence of vascular toxicity associated with ponatinib in patients with CML.^{6,7,27}

Previous studies investigating potential mechanisms for ischemic events with ponatinib have been largely inconclusive. A knowledge gap existed regarding the potential role of the endothelium. To investigate this possibility, we applied CEU molecular imaging, which employs tracers that are confined to the vascular compartment to assess endothelial events.^{8,18} Molecular imaging of the proximal thoracic aorta, a site that is susceptible to atherosclerosis in WSD-fed ApoE^{-/-} mice,¹¹ was performed with tracers targeted to (1) endothelial-associated large multimers of VWF that have undergone shear-mediated exposure of the A1-binding domain for the GPIIb component of the GPIIb-IX-V complex on platelets or (2) GPIIb, which reflects platelet adhesion to the endothelium and is constitutively expressed by platelets.^{8,18} This approach has recently been used to examine similar global endothelial abnormalities that occur after acute myocardial infarction that are responsible for a sudden increase in events in nonculprit arteries.⁸ Our data indicated that ponatinib increases endothelial VWF with exposure of the A1-binding domain and platelet adhesion several fold within days of initiation. These changes were not seen with the BCR-ABL1–targeted drug dasatinib, which does not have as broad TKI effects as ponatinib and has been associated with much lower rates of thrombotic events.⁶ While our data and those from prior studies studying ponatinib's effects on platelets have demonstrated either neutral or inhibitory effects,^{28,29} the GPIIb-mediated pathways uncovered in this study do not require platelet activation. They would therefore not necessarily respond favorably to traditional antiplatelet therapies used in atherosclerotic disease.

On molecular imaging, IV administration of ADAMTS13, a regulatory zinc protease that cleaves VWF at the Tyr1605-Met1606 site of the A2 domain to regulate multimer size,^{15,30} eliminated the signal for both VWF and platelets. The reversal of aortic platelet adhesion by high-dose rADAMTS13 therapy in ponatinib-treated animals that had normal ADAMTS13 levels supports the notion that ponatinib causes an acquired resistance to ultralarge multimers of VWF (UL-VWF) proteolytic cleavage that can be overcome with excess enzyme. In addition, ponatinib also increased surface expression of VWF on HUVECs cultured in a microfluidic system, indicating that increased surface mobilization and decreased proteolytic cleavage played a role.

Oxidative modification of ADAMTS13 and VWF can impair cleavage of endothelial UL-VWF^{31,32} and has been implicated in platelet–endothelial adhesion in atherosclerosis and acquired forms of thrombotic thrombocytopenic purpura.^{8,33} Accordingly, we tested the effect of coadministration of NAC (600 mg/kg per day by gavage), which maintains antioxidant activity, thereby improving endogenous protease activity.³⁴ We found a significant reduction in both endothelial-associated VWF and platelet adhesion. Because NAC can also directly reduce endothelial-associated UL-VWF through disulfide bond reduction,⁹ certainty of the role of ROS would require the administration of compounds that influence only oxidative stress.

In ponatinib-treated mice, we observed perfusion defects and regional WMAs without coronary artery occlusion or stenosis. This constellation of findings is consistent with a thrombotic microangiopathy, which is known to occur in the kidney with vascular endothelial growth factor receptor TKIs.^{35,36} Thrombotic microangiopathy in diseases such as thrombocytopenic purpura has been associated with high rates of myocardial infarction.^{37,38} A high proportion of these patients do not have obstructive epicardial coronary artery disease but do have postmortem findings of coronary microvascular thrombosis.^{37,39} The notion that segmental LV dysfunction and matching perfusion defects without coronary artery abnormalities in ponatinib-treated mice were due to microvascular angiopathy was supported by histologic evidence of platelet adhesion and by direct observation of endothelial-associated platelet strings and nets on intravital microscopy. The latter technique also revealed that platelet networks were attached on the downstream side of leukocytes. Potential reasons for this finding include that platelets bind to neutrophil-associated VWF or neutrophil extracellular traps,⁴⁰ although parsing these processes would be difficult based on the ability of platelets to trigger neutrophil extracellular traps through TLR-4 signaling.⁴¹ The observation of venular embolization of platelet aggregates on intravital microscopy is intriguing, since venous thromboembolism, which involves VWF-mediated platelet adhesion,⁴² has also been observed in clinical experience. The absence of classic markers of thrombotic microangiopathy such as schistocytes can best be explained by the severity of angiopathy, which was not fulminant, severe, and diffuse but rather indolent and patchy.

There are several limitations of the study that should be mentioned. The short duration of the study was adequate for assessing pathophysiologic mechanisms, but not necessarily all of the clinical sequelae. In humans, hypertension develops rapidly, similar to what we found in mice, but thrombotic complications occur over the course of months. The short duration of our experiments was also not designed to evaluate the worsening of atherosclerosis and thrombotic complications in large arteries seen in clinical experience.^{6,7} The short-duration protocols we used were not, however, designed to test this possibility. In fact, we believe large- and small-vessel pathologies are likely to be intertwined, since VWF-mediated platelet–endothelial interactions in atherosclerosis promote acceleration of plaque growth and inflammation.^{8,43} Because of limited blood sampling, we were not able to accurately measure endogenous ADAMTS13 activity, which would have strengthened the weight of our evidence. These measurements may be best suited to prospective study in clinical trials, since human ADAMTS13 assays are well established. Although we demonstrated that ponatinib influences endothelial cell ROS production and viability, we cannot at this time directly link these findings to the dose dependency of arterial thrombotic events. Finally, we studied a murine model lacking BCR-ABL1 without comparison with BCR-ABL1 transgenic models, implying that the thrombotic effects of ponatinib are not mediated through BCR-ABL1 inhibition.

In aggregate, our findings help elucidate mechanisms for vascular toxicity with the BCR-ABL1 TKI ponatinib that can be tested in humans. The identification of VWF-mediated platelet adhesion and a secondary indolent microvascular angiopathy in mice treated with ponatinib provides a basis for future testing in humans and reveals opportunities for potential mitigating strategies.

Summary of Techniques

Using several previously described techniques, we were able to demonstrate a clear pathway between ponatinib therapy and adverse cardiovascular events: Dysregulation of VWF leads to increased platelet adhesion and thrombotic microangiopathies, which lead to loss of coronary arterial patency, either locally or downstream through embolization, and finally loss of regional myocardial function and

reduced cardiac output. While the previous study examined the effect of cardiac dysfunction the vascular endothelium, this study was concerned with how changes at the endothelial surface cause cardiac dysfunction. As such, many of the techniques were similar between these studies, however this study was focused on relating myocardial function to local vascular function rather than vascular function remote territories. This focus required additional techniques such as angiography and fluorescent microsphere perfusion in order to relate microangiopathies to nearby myocardial dysfunction. By visualizing myocardial function using echocardiography and visualizing perfusion defects and coronary patency with fluorescent microspheres and angiography, we were able to spatially match regions with WMAs to regions with perfusion defects and loss of coronary patency. Since CEU molecular imaging of thrombotic processes was performed in the aorta rather than the myocardium, histological analysis was needed to directly relate local thrombotic processes to perfusion defects and loss of myocardial function.

References

1. Al-Kali A, Kantarjian H, Shan J, et al. . Current event-free survival after sequential tyrosine kinase inhibitor therapy for chronic myeloid leukemia. *Cancer*. 2011;117(2):327-335.
2. Pophali PA, Patnaik MM. The role of new tyrosine kinase inhibitors in chronic myeloid leukemia. *Cancer J*. 2016;22(1):40-50.
3. Cortes JE, Kantarjian H, Shah NP, et al. . Ponatinib in refractory Philadelphia chromosome-positive leukemias. *N Engl J Med*. 2012;367(22):2075-2088.
4. O'Hare T, Shakespeare WC, Zhu X, et al. . AP24534, a pan-BCR-ABL inhibitor for chronic myeloid leukemia, potently inhibits the T315I mutant and overcomes mutation-based resistance. *Cancer Cell*. 2009;16(5):401-412.
5. Uitdehaag JC, de Roos JA, van Doornmalen AM, et al. . Comparison of the cancer gene targeting and biochemical selectivities of all targeted kinase inhibitors approved for clinical use. *PLoS One*. 2014;9(3):e92146.
6. Moslehi JJ, Deininger M. Tyrosine kinase inhibitor-associated cardiovascular toxicity in chronic myeloid leukemia. *J Clin Oncol*. 2015;33(35):4210-4218.
7. Cortes JE, Kim DW, Pinilla-Ibarz J, et al. . Ponatinib efficacy and safety in Philadelphia chromosome-positive leukemia: final 5-year results of the phase 2 PACE trial. *Blood*. 2018;132(4):393-404.
8. Moccetti F, Brown E, Xie A, et al. . Myocardial infarction produces sustained proinflammatory endothelial activation in remote arteries. *J Am Coll Cardiol*. 2018;72(9):1015-1026.
9. Chen J, Reheman A, Gushiken FC, et al. . N-acetylcysteine reduces the size and activity of von Willebrand factor in human plasma and mice. *J Clin Invest*. 2011;121(2):593-603.
10. Meir KS, Leitersdorf E. Atherosclerosis in the apolipoprotein-E-deficient mouse: a decade of progress. *Arterioscler Thromb Vasc Biol*. 2004;24(6):1006-1014.
11. Kaufmann BA, Sanders JM, Davis C, et al. . Molecular imaging of inflammation in atherosclerosis with targeted ultrasound detection of vascular cell adhesion molecule-1. *Circulation*. 2007;116(3):276-284.

12. Ren M, Qin H, Ren R, Cowell JK. Ponatinib suppresses the development of myeloid and lymphoid malignancies associated with FGFR1 abnormalities. *Leukemia*. 2013;27(1):32-40.
13. Okabe S, Tauchi T, Kimura S, et al. . Combining the ABL1 kinase inhibitor ponatinib and the histone deacetylase inhibitor vorinostat: a potential treatment for BCR-ABL-positive leukemia. *PLoS One*. 2014;9(2):e89080.
14. Appelmann I, Rillahan CD, de Stanchina E, et al. . Janus kinase inhibition by ruxolitinib extends dasatinib- and dexamethasone-induced remissions in a mouse model of Ph+ ALL. *Blood*. 2015;125(9):1444-1451.
15. Ruggeri ZM. Von Willebrand factor, platelets and endothelial cell interactions. *J Thromb Haemost*. 2003;1(7):1335-1342.
16. Dong JF. Cleavage of ultra-large von Willebrand factor by ADAMTS-13 under flow conditions. *J Thromb Haemost*. 2005;3(8):1710-1716.
17. Lindner JR, Song J, Christiansen J, Klibanov AL, Xu F, Ley K. Ultrasound assessment of inflammation and renal tissue injury with microbubbles targeted to P-selectin. *Circulation*. 2001;104(17):2107-2112.
18. Shim CY, Liu YN, Atkinson T, et al. . Molecular imaging of platelet-endothelial interactions and endothelial von Willebrand factor in early and mid-stage atherosclerosis. *Circ Cardiovasc Imaging*. 2015;8(7):e002765.
19. Kaufmann BA, Wei K, Lindner JR. Contrast echocardiography. *Curr Probl Cardiol*. 2007;32(2):51-96.
20. Eckersley RJ, Chin CT, Burns PN. Optimising phase and amplitude modulation schemes for imaging microbubble contrast agents at low acoustic power. *Ultrasound Med Biol*. 2005;31(2):213-219.
21. Lindner JR, Coggins MP, Kaul S, Klibanov AL, Brandenburger GH, Ley K. Microbubble persistence in the microcirculation during ischemia/reperfusion and inflammation is caused by integrin- and complement-mediated adherence to activated leukocytes. *Circulation*. 2000;101(6):668-675.
22. Schindelin J, Arganda-Carreras I, Frise E, et al. . Fiji: an open-source platform for biological-image analysis. *Nat Methods*. 2012;9(7):676-682.
23. Jain P, Kantarjian H, Jabbour E, et al. . Ponatinib as first-line treatment for patients with chronic myeloid leukaemia in chronic phase: a phase 2 study. *Lancet Haematol*. 2015;2(9):e376-e383.
24. von Hundelshausen P, Weber KS, Huo Y, et al. . RANTES deposition by platelets triggers monocyte arrest on inflamed and atherosclerotic endothelium. *Circulation*. 2001;103(13):1772-1777.
25. Popa M, Tahir S, Elrod J, et al. . Role of CD40 and ADAMTS13 in von Willebrand factor-mediated endothelial cell-platelet-monocyte interaction. *Proc Natl Acad Sci USA*. 2018;115(24):E5556-E5565.
26. Yasu T, Momo K, Kobayashi S, Kuroda S, Tojo A. Simple determination of plasma ponatinib concentration using hplc. *Biol Pharm Bull*. 2018;41(2):254-25.
27. Müller MC, Cervantes F, Hjorth-Hansen H, et al. . Ponatinib in chronic myeloid leukemia (CML): Consensus on patient treatment and management from a European expert panel. *Crit Rev Oncol Hematol*. 2017;120:52-59.
28. Loren CP, Aslan JE, Rigg RA, et al. . The BCR-ABL inhibitor ponatinib inhibits platelet immunoreceptor tyrosine-based activation motif (ITAM) signaling, platelet activation and aggregate formation under shear. *Thromb Res*. 2015;135(1):155-160.
29. Neelakantan P, Marin D, Laffan M, Goldman J, Apperley J, Milojkovic D. Platelet dysfunction associated with ponatinib, a new pan BCR-ABL inhibitor with efficacy for chronic myeloid leukemia resistant to multiple tyrosine kinase inhibitor therapy. *Haematologica*. 2012;97(9):1444.
30. Chauhan AK, Motto DG, Lamb CB, et al. . Systemic antithrombotic effects of ADAMTS13. *J Exp Med*. 2006;203(3):767-776.
31. Wang Y, Chen J, Ling M, López JA, Chung DW, Fu X. Hypochlorous acid generated by neutrophils inactivates ADAMTS13: an oxidative mechanism for regulating ADAMTS13 proteolytic activity during inflammation. *J Biol Chem*. 2015;290(3):1422-1431.
32. Chen J, Fu X, Wang Y, et al. . Oxidative modification of von Willebrand factor by neutrophil oxidants inhibits its cleavage by ADAMTS13. *Blood*. 2010;115(3):706-712.

33. Sadler JE. Pathophysiology of thrombotic thrombocytopenic purpura. *Blood*. 2017;130(10):1181-1188.
34. Sun SY. N-acetylcysteine, reactive oxygen species and beyond. *Cancer Biol Ther*. 2010;9(2):109-110.
35. Eremina V, Jefferson JA, Kowalewska J, et al. . VEGF inhibition and renal thrombotic microangiopathy. *N Engl J Med*. 2008;358(11):1129-1136.
36. Sartelet H, Toupance O, Lorenzato M, et al. . Sirolimus-induced thrombotic microangiopathy is associated with decreased expression of vascular endothelial growth factor in kidneys. *Am J Transplant*. 2005;5(10):2441-2447.
37. Patschan D, Witzke O, Dührsen U, Erbel R, Philipp T, Herget-Rosenthal S. Acute myocardial infarction in thrombotic microangiopathies--clinical characteristics, risk factors and outcome. *Nephrol Dial Transplant*. 2006;21(6):1549-1554.
38. Gandhi K, Aronow WS, Desai H, et al. . Cardiovascular manifestations in patients with thrombotic thrombocytopenic purpura: a single-center experience. *Clin Cardiol*. 2010;33(4):213-216.
39. Ridolfi RL, Hutchins GM, Bell WR. The heart and cardiac conduction system in thrombotic thrombocytopenic purpura. A clinicopathologic study of 17 autopsied patients. *Ann Intern Med*. 1979;91(3):357-36.
40. Grässle S, Huck V, Pappelbaum KI, et al. . von Willebrand factor directly interacts with DNA from neutrophil extracellular traps. *Arterioscler Thromb Vasc Biol*. 2014;34(7):1382-1389.
41. Clark SR, Ma AC, Tavener SA, et al. . Platelet TLR4 activates neutrophil extracellular traps to ensnare bacteria in septic blood. *Nat Med*. 2007;13(4):463-469.
42. Takahashi M, Yamashita A, Moriguchi-Goto S, et al. . Critical role of von Willebrand factor and platelet interaction in venous thromboembolism. *Histol Histopathol*. 2009;24(11):1391-1398.
43. Jin SY, Tohyama J, Bauer RC, Cao NN, Rader DJ, Zheng XL. Genetic ablation of Adamts13 gene dramatically accelerates the formation of early atherosclerosis in a murine model. *Arterioscler Thromb Vasc Biol*. 2012;32(8):1817-1823.

Acknowledgements and Disclosures

I would like to acknowledge my lab-mates, mentors, instructors, classmates, and family for the many different ways in which they helped to support me as I navigated through this graduate program. I am grateful for my rotation advisors, Dr. Larry Sherman and Dr. Monica Hinds, for mentoring me as I transitioned from an undergraduate student to a graduate researcher. My instructors, namely Dr. Catherine Morgans and Jim McCormick, provided me with the tools to develop a more rich and detailed understanding of human physiology and biomedical research, while teaching me how to learn independently and collaboratively.

To my lab-mates, I extend my unending appreciation for the countless hours spent guiding me through equipment, techniques, and theory. My growth as a scientist is thanks to the wonderful and diverse role models with whom I have the pleasure of working and studying. While I have only had the chance to work with a small portion of the KCVI and BME faculty and researchers, these departments have been such welcoming communities and have provided unique learning opportunities, both formal and informal, for me to learn and grow as a biomedical engineer and a cardiovascular researcher.

Special thanks to my thesis committee, Dr. Monica Hinds (chair), Dr. Cheryl Maslen, and Dr. George Giraud for all of the time, energy, and dedication that goes into mentoring a student, and for always providing me with candid and honest feedback, which helped me overcome challenges and find the most appropriate path for me through my graduate education.

Finally, I am immensely thankful for the mentorship of Dr. Jonathan Lindner, who brought me into his laboratory at a time when I knew little to nothing about cardiovascular imaging. Dr. Lindner's passion for mentoring trainees is truly remarkable,

and I can thank his ability to patient, encouraging, and supportive for the skills and knowledge I have acquired from my graduate research

Case Study Acknowledgements, Authorship, and Disclosures

Chapter 5

Brown, E., Ozawa, K., Moccetti, F., Vinson, A., Hodovan, J., Xie, A., Bader, L., Lopez, J.A., Kievet, P., Shaw, G.D., Chen, J., Lindner J.R. (2020) Arterial Platelet-Endothelial Interactions Occur at the Stage of Early Intimal Thickening in Obese, Insulin-Resistance Primates. (Pre-Submission)

Acknowledgements

Dr. Ozawa is supported by a grant from the JSPS Overseas Research Fellowship and Manpei Suzuki Diabetes Foundation. Dr. Moccetti is supported by a grant from the Swiss National Science Foundation. Dr. Lindner is supported by grants R01-HL078610, R01-HL130046, and P51-OD011092 from the National Institutes of Health (NIH), Bethesda, MD. Dr. Lopez is supported by grant R35-HL145262 from the NIH. The Endocrine Technologies Core (ETC) at the Oregon National Primate Research Center (ONPRC) is supported by NIH Grant P51OD011092.

Conflict-of-interest disclosure

There are no disclosures or relationships with industry to disclose.

Chapter 6

Moccetti, F., Brown, E., Xie, A., Packwood, W., Qi, Y., Ruggeri, Z., Shentu, W., Chen, J., López, J. A., & Lindner, J. R. (2018). Myocardial Infarction Produces Sustained Proinflammatory Endothelial Activation in Remote Arteries. *Journal of the American College of Cardiology*, 72(9), 1015–1026. <https://doi.org/10.1016/j.jacc.2018.06.044>

Acknowledgements

Dr. Lindner is supported by grants R01-HL078610 and R01-HL130046; Dr. López is supported by R01-HL091153 and R01-HL11763; and Dr. Ruggeri is supported by HL42846 and HL78784 from the NIH. Dr. Lindner is also supported by a grant (14-14NSBR11-0025) from the NASA National Space Biomedical Research Institute. Dr. Moccetti is supported by a grant from the Swiss National Science Foundation. Authorship

Conflict-of-interest disclosure

There are no disclosures or relationships with industry to disclose.

Chapter 7

Latifi, Y., Moccetti, F., Wu, M., Xie, A., Packwood, W., Qi, Y., Ozawa, K., Shentu, W., Brown, E., Shirai, T., McCarty, O. J., Ruggeri, Z., Moslehi, J., Chen, J., Druker, B. J., López, J. A., & Lindner, J. R. (2019). Thrombotic microangiopathy as a cause of cardiovascular toxicity from the BCR-ABL1 tyrosine kinase inhibitor ponatinib. *Blood*, 133(14), 1597–1606. <https://doi.org/10.1182/blood-2018-10-881557>

Acknowledgements

This work was supported by National Institutes of Health, National Heart, Lung, and Blood Institute grants R01-HL078610 and R01-HL120046, and National Institutes of Health, Office of the Director grant P51-OD011092 (J.R.L.), National Institutes of Health, National Heart, Lung, and Blood Institute grant K08-HL133493 (M.W.), National Institutes of Health, National Heart, Lung, and Blood Institute grants HL42846

and HL78784 (Z.R.), and National Institutes of Health, National Heart, Lung, and Blood Institute grants R01-HL091153 and R01-HL11763 (J.A.L.), the Swiss National Science Foundation (grant P2BSP3-158853) (F.M.), a Japan Society for the Promotion of Science Overseas Research Fellowship (K.O.), and the Manpei Suzuki Diabetes Foundation and Novartis (F.M.). The study was supported by a material grant from Takeda Pharmaceutical Co., which provided ponatinib.

Authorship

Contribution: J.R.L., J.M., O.J.M., and J.A.L. conceived the hypothesis and designed the study; Y.L., F.M., M.W., A.X., W.P., Y.Q., K.O., W.S., E.B., Z.R., J.C., T.S., J.A.L., and J.R.L. performed research and interpreted data; Y.L., F.M., and J.R.L. made the figures; and Y.L., J.M., B.J.D., J.A.L., and J.R.L. wrote the manuscript.

Conflict-of-interest disclosure

B.J.D. is a member of the scientific advisory board (SAB) for Aileron Therapeutics, ALLCRON, Cepheid, Gilead Sciences, Vivid Biosciences, Celgene, and Baxalta (inactive); is an SAB member and owns stock in Aptose Biosciences, Blueprint Medicines, β Cat, GRAIL, Third Coast Therapeutics, and CTI BioPharma (inactive); is a scientific founder of and owns stock in MolecularMD; is a member of the board of directors and owns stock in Amgen; is a member of the board of directors for Burroughs Wellcome Fund, CureOne; is a member of the Joint Steering Committee at Beat AML LLS; and receives clinical trial funding from Novartis, Bristol-Myers Squibb, and Pfizer, and royalties from patent 6958335 (Novartis exclusive license) and Oregon Health & Science University and Dana-Farber Cancer Institute (one Merck exclusive license). The remaining authors declare no competing financial interests.